HALF-METALLIC CrO_2 THIN FILMS FOR SPINTRONIC APPLICATIONS

by

MANJIT PATHAK

A DISSERTATION

Submitted in partial fulfilment of the requirements
for the degree of Doctor of Philosophy in the
Department of Physics and Astronomy
in the Graduate School of
The University of Alabama

TUSCALOOSA, ALABAMA

2011

ABSTRACT

CrO_2 is a well-established half-metallic oxide with near perfect spin polarization − known to have the highest spin polarization among all known materials theoretically as well as experimentally. This means that the conduction electrons in CrO_2 have only one kind of spin i.e. conduction is due only to the majority spin electrons. Because of its high spin polarization, CrO_2 stands as an ideal and one of the most attractive candidates for spin-electronic applications as well as of fundamental interests. The enormous potential of CrO_2 is still untapped since thin film growth modes, interface/surface properties and various factors affecting them are not very well understood or, relatively unknown. Reported works confirm strained growth of (100) CrO_2 films and strain free growth of (110) CrO_2 films on iso-structural TiO_2 substrates investigated using X−ray diffraction. Superconducting quantum interference device (SQUID) and element specific X-ray magnetic circular dichroism (XMCD) techniques were employed to investigate the effect of this substrate-induced strain on the magnetic properties of the films. Magnetic tunnel junctions (MTJ) were fabricated with CrO_2, Cr_2O_3 [natural oxide of Cr] as the thin insulating barrier and Co as the other ferromagnetic electrode using photolithography. I−V characteristics of this spin-electronic device are reported. Also, results on the low pressure chemical vapor deposition (CVD) growth of CrO_2 and its comparison with standard growth technique under atmospheric pressure are reported.

Dedicated to my family and friends

SYMBOLS AND ABBREVIATIONS

a, b, c	lattice constants, unit cell directions
d	Crystal lattice spacing, film thickness, tunnel barrier thickness in an MTJ
e	Charge of an electron (1.6×10^{-19} C)
E	Energy, electric field
h	Planks constant ($=6.626\times^{-34}$ Js)
$\hbar$	reduced Planks constant, ($h/2\pi$)
H	Applied magnetic field
H_c	Coercivity
H_k	Anisotropy field
I	Current
J	Current density
k	Wave vector
k_B	Boltzmann constant (1.38×10^{-23} JK $^{-1}$)
$\mathbf{l}$	Angular momentum
m	Slope obtained from a linear fit, mass of an electron (9.1×10^{-31} kg)
m_s	Spin moment
m_l	Angular moment
M_s	Saturation magnetization
P	Spin polarization, polarization of X-rays
$\mathbf{q}$	Reciprocal space vector
R_a	Average roughness
R_{AP}	Resistance of an MTJ for antiparallel configuration of magnetization
R_P	Resistance of an MTJ for parallel configuration of magnetization
R_q	RMS roughness
V	Voltage

$\mathbf{s}$	Spin momentum
t	Film thickness
γ	Interface energy
λ	Wavelength
θ	Angle of incidence of X-ray beam
θ_c	Critical angle
φ	Angle of rotation about Y-axis, barrier height
Φ	Work function
$\Delta\varphi$	Barrier asymmetry
ψ	Angle of rotation about X-axis
ω	diffracted beam angle, harmonic oscillator frequency, ac modulation frequency
ρ	Resistivity
σ	Conductivity, surface energy
ac	Alternating current
AFM	Atomic force microscopy
AMR	Anisotropic magnetoresistance
APCVD	Atmospheric pressure chemical vapor deposition
BE	Binding energy
CIP	Current in-plane
CPP	Current perpendicular to plane
CVD	Chemical vapor deposition
dc	Direct current
DOS	Density of states
EDX	Energy dispersive X-ray
FM	Ferromagnetic metal
FWHM	Full width at half maximum

GMR	Giant magnetoresistance
IBE	Ion beam etching
IETS	Inelastic electron tunneling spectroscopy
KE	Kinetic energy
LDA	Local density approximation
LPCVD	Low pressure chemical vapor deposition
MRAM	Magnetic random access memory
MTJ	Magnetic tunnel junction
NM	Normal metal
PR	Photoresist
PVD	Physical vapor deposition
RF	Radio frequency
RMS	Root mean square
RRR	Residual resistivity ratio
RSM	Reciprocal space mapping
SNR	Signal to noise ratio
SQUID	Superconducting quantum interference device
STT-RAM	Spin-torque transfer random access memory
TMR	Tunnel magnetoresistance
TEY	Total electron yield
T_z	Quadrupolar magnetic moment
VSM	Vibrating sample magnetometer
XAS	X-ray absorption spectroscopy
XMCD	X-ray magnetic circular dichroism
XPS	X-ray photo-electron spectroscopy
XRD/XRR	X-ray diffraction/reflection

ACKNOWLEDGEMENT

I am pleased to have this opportunity to thank many faculty members, colleagues and friends who helped me with this research project. First I would like to thank Prof. Patrick R. LeClair, my adviser for his guidance, encouragement and discussion throughout this work. He motivated me to do scientific research in experimental condensed matter physics during my first year as a graduate student. Also, I thank Prof. Arunava Gupta for his consistent guidance and suggestion as my co−adviser in this project. Next I would like to thank all of my committee members, Prof. Gary J. Mankey, Prof. William H. Butler and Prof. Raymond E. White for their invaluable suggestions, motivation and support of both the dissertation and my academic progress. Next I would like to especially thank Dr. Dipanjan Mazumdar and Dr. Hideo Sato, who are post−doctoral fellows at the MINT Center for offering their help in the laboratory and discussion in this project. I would also like to thank Prof. Tim Mewes for helping me with my work during the initial years and Prof. Y. K. Hong for his three months summer support during 2007. Prof. J. W. Harrell′s guidance during my first semester as teaching assistant is also greatly appreciated.

The group of smart colleagues in the MINT Center was of great help undertaking the challenges in this project. I thank Xueyu Zhang for helping me with the sample preparation. Krishna B. Chetry had been really helpful as a senior student in this project. Also, I thank Jinwen Wang for mentoring me on low pressure CVD and Xing Zhong for following me up in this process. I am also very grateful and thankful to my colleagues and friends - Vilas, Vijay, Hunter, Zeenath, Weihao, Vishal, Sreeni, Jon, Justin, Abilash, Harshan for helping me as necessary in my work.

Part of my research work was done at the synchrotron radiation center (SRC), University of Wisconsin, Madison. I would like to thank Mary Severson and Mark Bissen at SRC for helping me with the beam line and troubleshooting during the experiment. Also, I am very grateful to Dr. E. Goering in Max-Plank-Institute für Metallforschung, Stuttgart, Germany for helping me with XMCD data analysis through e−mail communication.

The staff at the MINT Center, UA CAF, UA MFF and at the physics machine shop had been really kind and helpful over the years. I would like to thank John Hawkins, James Weston, Iulica Zana for training me on the facilities at MINT Center, Dr. Alton Highsmith for training with the micro−fabrication facilities at UA MFF and Rich Marten and Johnny Goodwin for helping with UA CAF facilities. Danny Whitcomb and Jason Kuykendall from physics department staff were very helpful with troubleshooting the electronics in various instruments. David Key and Joe Howell in the physics machine shop made lot of thing easier for me during the work. I thank Nancy, Michelle and Karen in the physics department office staff for their professional help. I am also really very thankful to Jason, (late) Tabatha, Jamie, Casey, and Carrie - staff at the MINT office for helping me with computer network solutions, placing numerous orders for my laboratory work and for making several work related travel arrangements.

Finally, a huge thank to all my friends and family back home for making these years in Tuscaloosa eventful and quite enjoyable.

This work was supported by NSF under Grant No. DMR-0706280.

CONTENTS

LIST OF TABLES

LIST OF FIGURES

Chapter 1

OUTLINE

In this dissertation, after the introductory chapter, providing an overview of the research work, the principles of the major experimental techniques used during this work are introduced in chapter 3. Comparison of thin film properties of two orientations of CrO_2, namely (100) and (110), have been described in chapter 4. It was found that although it is nominally the same CrO_2, thin film properties can be significantly different in these two crystal orientations when they are epitaxially grown on TiO_2 substrates of respective orientations. Surface/interface magnetic properties of epitaxial (100) and (110) CrO_2 films have been reported in chapter 5. Another important issue regarding growth of CrO_2 is that not much is known about synthesizing the CrO_2 phase under low pressure, in spite of the fact that low pressure deposition of thin films is desired for spintronic devices. Low pressure synthesis of CrO_2 is discussed in chapter 6. As much work have been previously reported on (100) oriented CrO_2 for spintronic devices [1, 2, 3], a comparison of devices with (110) CrO_2 is discussed in chapter 7.

Chapter 2

INTRODUCTION TO SPINTRONICS

All the work described in this dissertation are related to the relatively new field of spintronics – derived from the words spin and electronics. In a traditional semiconductor device, the charge of electrons is manipulated to achieve device functionality. However, electrons also carry spin together with charge. In spintronics, this additional degree of freedom is manipulated to realize newly functional devices. Among many *proof of concept* and *futuristic* spintronic devices, most notable are the *magnetoresistance* devices that have already been integrated in the read head sensors of magnetic hard-disc drives (electrical resistance change in presence of a magnetic field is called magnetoresistance).

Magnetic materials are integral parts of spintronic devices since in a magnetic material electron spins can be controlled with a magnetic field. In a ferromagnetic material, due to the imbalance in number of up and down spin electrons, currents are *spin–polarized*. High spin–polarization in a magnetic material is desired for excellent performance of a spintronic device. Among all known materials so far, CrO_2 – a metastable chromium oxide, is found to have almost 100% spin polarization which is highest among all known materials. This near perfect spin polarization (described later in this chapter in section 2.2.2) was first theoretically predicted in CrO_2 [4] and experimentally proved later [5, 6, 7]. As such, CrO_2 stands as one of the most ideal candidates for a spintronic device. CrO_2 belongs to the class of materials called half-metals.

2.1 Transport phenomena in spintronics

Fabrication of spintronic devices has been possible because of the significant improvements in thin film deposition techniques. When two thin ferromagnetic layers are separated by a very thin metallic or insulating layer, significant change in electrical resistance of the stack is observed in presence of a magnetic field depending on the relative

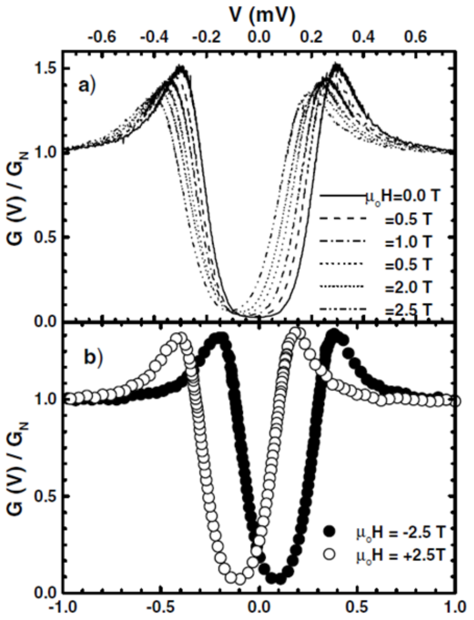

Figure 2.1: (a) Zeeman splitting of conductance curves at different magnetic fields and (b) at ±2.5 T magnetic fields of a CrO_2/Insulator/Al(superconductor) junction obtained at 0.4 K. Only two peaks are observed within ± 1.0 mV bias voltage for different applied magnetic fields indicating the presence of electrons with same spin. Minority spin is absent in CrO_2 as found by Parker et al. [5].

orientations of the magnetic moments in the ferromagnetic films. When the separating layer is metallic, this effect is called giant magnetoresistance (GMR) as this effect is much bigger than the effect due to the magnetic anisotropy of the magnetic material. When the separating layer is an insulator, it is called tunnel magnetoresistance (TMR) effect. Numerically, both GMR and TMR are calculated as:

$$GMR, TMR = \frac{R_{AP} - R_P}{R_P} \times 100\% \tag{2.1}$$

Here, R_{AP} and R_P are the resistances for the parallel and antiparallel configurations of the magnetizations respectively. Although these effects are similar, their mechanisms are quite different. These two effects are qualitatively described as we proceed in this chapter. Since CrO_2 is a ferromagnetic material, these effects, in principle, can be observed in a device with CrO_2 as one of the two ferromagnetic layers. Among other spintronic devices, most notable are spin field effect transistor (spin-FET) or simply spin-transistor and spin torque transfer random access memory (STT-RAM) device, and significant research have been going on all over the world to realize these devices for both fundamental interests and technological importance. These two devices are not described in this dissertation, as this work was focused on realizing especially the TMR devices with CrO_2 as an electrode.

2.1.1 Giant magnetoresistance effect

The giant magnetoresistance (GMR) effect was simultaneously discovered in Fe/Cr multi-layers by Prof. Albert Fert′s group [8] and in Fe/Cr/Fe trilayers by Prof. Peter Grunberg′s group [9] in 1988 (both were awarded Nobel prizes in physics for the year 2007 for this discovery). GMR effect can qualitatively be understood using Mott model [10, 11, 12]. This model states that conduction of spin up and spin down electrons in a ferromagnetic material can be treated separately with different scattering rates. For electron spins aligning with the net magnetic moment of the material, scattering is low and we observe low electrical resistance, while for anti-parallel alignment of the electron spin with net magnetic moment, scattering is high and therefore we observe a higher electrical resistance.

Based on this argument, current in a GMR device can be considered to be composed of two parallel channels - a spin up channel and a spin down channel. As shown in fig. 2.2 (a), for spin up electrons, spin is aligned with the magnetic moment and therefore we have less scattering for spin up electrons in both top and the bottom magnetic layers. However, for the spin down electrons, spin is aligned opposite to the magnetic moment in both top and bottom magnetic layers and we have high scattering. For this combination with magnetic moments being parallel in the top and bottom magnetic layers, the overall electrical resistance in the stack is low. Now the magnetization direction in the top layer is switched applying an external magnetic field keeping the magnetization direction in the bottom layer fixed. This can be achieved with anti-ferromagnetic coupling of the bottom layer or simply having the top and the bottom magnetic layers with different coercivities. In this antiparallel configuration of magnetic moments as shown in fig. 2.2(b), scattering

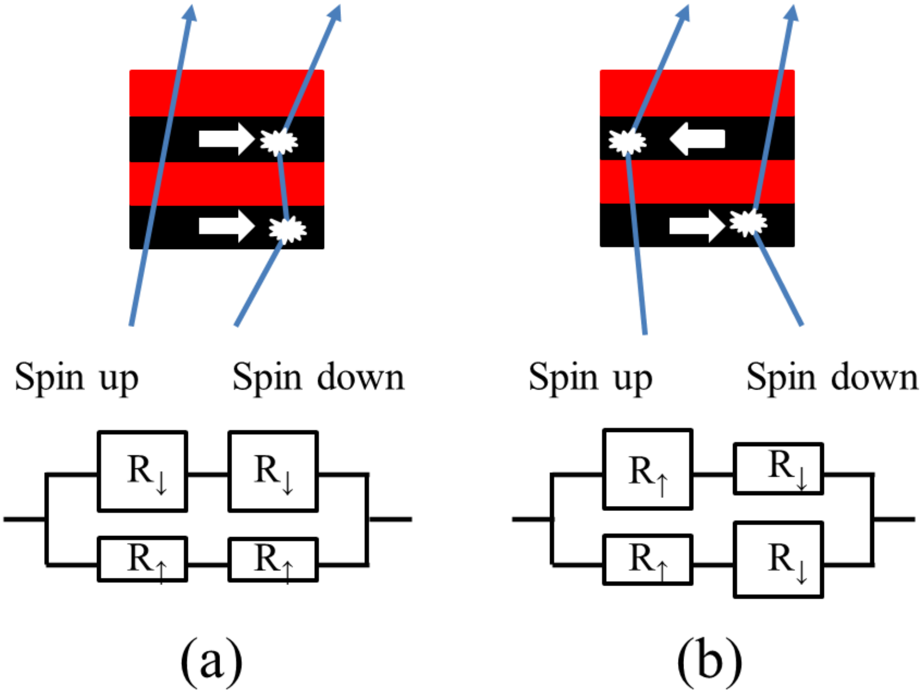

Figure 2.2: Schematic of GMR effect with parallel (a) and antiparallel (b) configurations. Arrows indicate the magnetization direction in the magnetic layers. Spin up and spin down electron trajectories are shown in both configurations assuming that mean free path of electrons is much larger than the film thicknesses. $R_\uparrow$ and $R_\downarrow$ are resistances of up spin and down spin electrons respectively. Small and large boxes qualitatively correspond to the electrical resistance values in the magnetic layers for up and down spin electrons.

is significant when spin and magnetic moments are not aligned and accordingly we have higher scattering of up spins from the top magnetic layer and higher scattering of down spins from the bottom magnetic layer. Overall the electrical resistance of the GMR stack in this antiparallel configuration is higher than that in parallel configuration. This high resistance can be assigned logic 1 and the low resistance as logic 0 to get a memory device compatible with binary logic.

2.1.2 Tunnel magnetoresistance effect

Tunneling is a quantum mechanical phenomenon first experimentally demonstrated by Ivar Giaever when he measured the superconducting energy gap in Pb using a Al/ Al_2O_3/ Pb junction [13]. Tunnel magnetoresistance (TMR) effect was first observed by

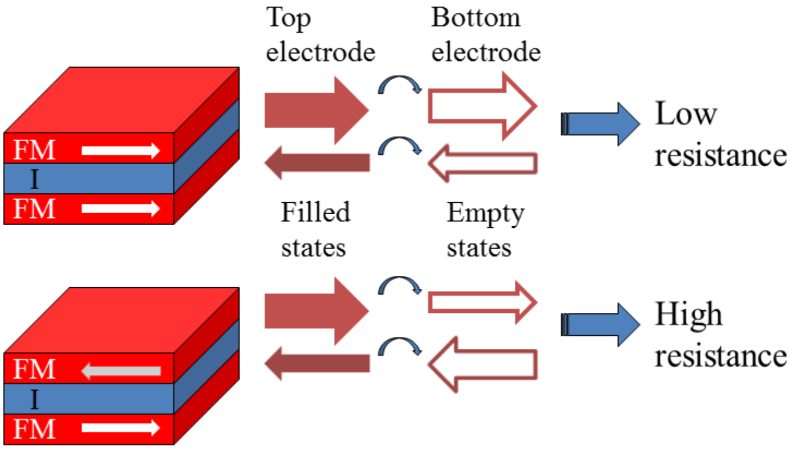

Figure 2.3: Schematic of TMR structure with parallel (top) and antiparallel (bottom) configurations of the ferromagnetic (FM) electrodes with an insulating barrier (I) between them. Arrows indicate the magnetization directions. Assuming electrons are moving from top to bottom electrode, filled states in the top electrode and corresponding available empty states in the bottom electrode are qualitatively shown for the parallel and antiparallel configuration of magnetization directions. Parallel configuration gives rise to low resistance state while the antiparallel configuration gives rise to the high resistance state of the device.

Julliere in 1975 [14]. He found TMR of 14% at 4.2 K in a Fe/Ge-O/Co magnetic tunnel junction (MTJ). When two ferromagnetic layers are separated by a very thin insulating layer, magnetoresistance effect can be observed because of the tunneling of electrons from one ferromagnetic layer to the other. The observed magnetoresistance in TMR effect is usually much higher than that observed in GMR effect. According to Jullieres model [14], tunnelling probabilities of spin up and spin down electrons are proportional to the product of density of states of the ferromagnetic electrodes at their Fermi levels:

$$T_{\uparrow(\downarrow)} = D_{top}(\varepsilon_{Ftop})_{\uparrow(\downarrow)} D_{bottom}(\varepsilon_{Fbottom})_{\uparrow(\downarrow)} \tag{2.2}$$

The mechanism of TMR can be understood in terms of the schematic in fig. 2.3. When the magnetization directions in the top and the bottom electrodes are parallel, majority electrons in one electrode have more states available in the other electrode to tunnel through the barrier. Minority electrons, which are much less in number than majority electrons, have less states available in the other electrode to tunnel into. When the magnetizations are anti-parallel, majority electrons have less states available in the other electrode compared to the parallel magnetization configuration however, minority electrons have significantly more states available. This anti-parallel configuration of magnetization has much higher electrical resistance than the parallel configuration. As with GMR, these high and low resistance states in TMR can be assigned logic 1 and logic 0 for memory devices, and TMR devices have already been successfully incorporated in read head sensor in the hard disc drives and commercially available magnetic random access memories (MRAM).

The above qualitative description, based on Jullierres model predicts the TMR values in a magnetic tunnel junction as:

$$TMR = \frac{2P_1P_2}{1 - P_1P_2} \times 100\% \tag{2.3}$$

Here P_1 and P_2 are spin polarization of the top and bottom magnetic layers respectively or vice versa. Thus, the TMR value is also limited by the spin polarization values of the magnetic electrodes according to Jullieres model and therefore ferromagnetic materials with very high spin polarization, such as CrO_2, are investigated for TMR. Jullierres model predicts infinite TMR for ferromagnetic electrodes with 100% spin polarization of top and bottom magnetic layers, although it is practically very unlikely. Still, this simple model successfully explains TMR observed with Al_2O_3 amorphous barrier at room temperature as first observed simultaneously in 1995 by two different groups - Dr. J. S. Moodera′s group (MIT, Boston) [15] and by Dr. Miyazaki and Dr. Tezuka (Tohoku University, Japan) [16] (maximum TMR observed in Al_2O_3 based device is about 70%). Few years later in 2001, Prof. W. H. Butler [17] (Oak Ridge National Laboratory, Tennessee) and Mathon et al. [18] (City University, London) predicted that much higher TMR should be observed in crystalline heterostructure such as (001) Fe/MgO/Fe. According to this model (popularly known as Butler model) based on first principles (first principles in physics mean that we start with atomic wave functions and without any significant further assumptions), electrons in *spd* hybridized band (namely the Δ_1 band) tunnel very easily from one electrode to the other for the parallel configuration of magnetization directions because of the symmetry of this band in Fe and MgO. As Δ_1 band is not present in the minority states, minority electrons tunnel poorly for anti-parallel magnetizations. There are electrons in other hybridized bands, however, filtering of Δ_1 electrons is most significant effect. Theoretically, this model predicts TMR of more than 1000%, and Parkin et al [19] and Yuasa et al [20] were able to experimentally observe high TMR of few 100% in MTJs with an MgO barrier as predicted by this model. This high TMR basically makes the device act like a switch or valve. Because of that, there have been renewed technological interests in spintronic devices in recent years to further enhance the TMR or GMR value. Recently, more than 600% room temperature TMR has been observed in CoFeB/MgO/CoFeB junctions annealed at high temperature [21].

GMR effect can be observed in two different geometries namely, current in-plane (CIP) with the film and current perpendicular to plane (CPP) of the film. Although the GMR effect is smaller in CIP geometry, it is easier to measure the effect in the CIP geometry. The CPP geometry is also more difficult to fabricate. However, the CPP geometry is preferred over the CIP geometry as the GMR effect is larger in this geometry and also it is technologically more relevant as the device size can be reduced to sub-micron level in CPP geometry with state of the art lithography techniques.

2.1.3 Current driven switching

In GMR and TMR effects mentioned above, the free magnetic layer is switched by an external magnetic field to observe the high and low resistance states in the multilayered structure. The magnetization direction in the free layer in CPP geometry can

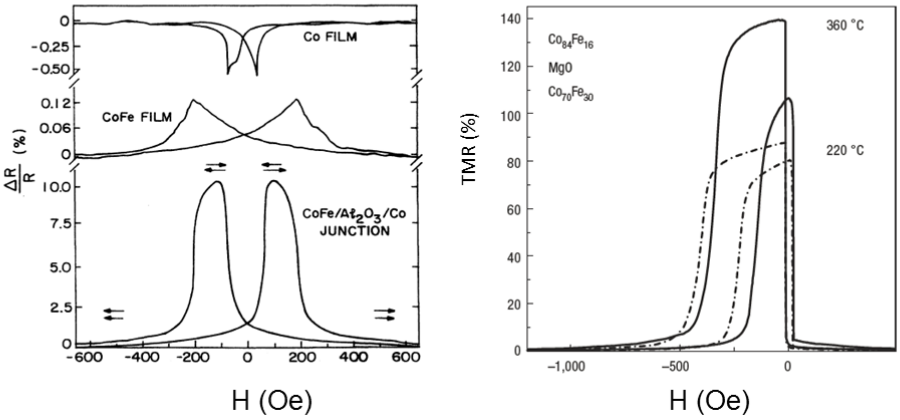

(a) Al_2O_3 barrier (b) MgO barrier

Figure 2.4: Experimentally observed TMR at room temperature in (a) CoFe/ Al_2O_3/Co junction [15] and (b) (100) CoFe/MgO/CoFe junction [19]. Higher TMR observed in crystalline MgO based devices is because of coherent tunnelling of electrons for parallel alignment of top and bottom layer magnetizations which is absent in amorphous Al_2O_3 based devices. Devices are annealed in (b) at temperatures much higher than room temperature to optimize crystalline quality.

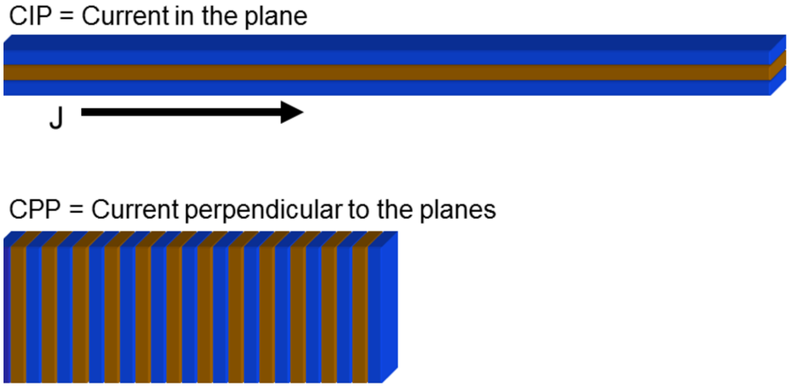

Figure 2.5: Geometries for CIP and CPP GMR.

also be switched by passing sufficiently high current in either direction. Two different mechanisms explain this phenomenon. According to Berger, spin waves are generated because of spin splitting of chemical potential at ferromagnetic resonance frequency [22] while Slonczewski modeled the critical current to switch the magnetization direction [23]. When the magnetic layer thicknesses are very small (∼1 nm), a high spin polarized current density (10^8 A/cm^2) transfers the angular moments from one magnetic layer to the other. This transfer of angular moment exerts torque on the magnetic moments i.e. spins and sufficiently high torque can flip the spins, effectively switching the magnetization direction. Sub-micron lateral dimensions of ∼100 nm diameter gives sufficiently high current densities in the devices to achieve this. Fig. 2.6 illustrates the current induced switching in a a trilayer device [24].

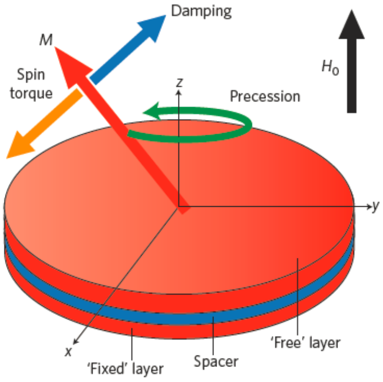

Figure 2.6: Geometry of spin-torque oscillator in a fixed magnetic layer, spacer and free magnetic layer system as illustrated by Slavin and Tiberkevich [24]. The free layer magnetization, M precesses around the applied magnetic field, H_0. The magnetic damping and the spin-torque acts against each other. Sufficient spin polarized current can cause the free layer magnetization to flip overcoming the natural magnetization damping.

2.2 Materials for spintronic devices

In this section, an overview of material selection for GMR and TMR devices is provided from current literature review.

2.2.1 Materials and their properties for GMR and TMR devices

Since the discovery of GMR effect, multilayer structures of ferromagnetic/normal metal (FM/NM) and ferromagnetic/normal metal/ferromagnetic (FM/NM/FM) materials have been extensively studied considering the technological significance of this effect [12]. The high GMR observed by Baibich et al in Fe/Cr multilayers is because of lattice matching of these materials and band matching for one kind of spin [8]. Fe and Cr have bcc structures and they have almost negligible lattice mismatch. Minority spins have excellent band matching between Fe and Cr, while their majority bands are quite dissimilar. This gives rise to strong spin dependent scattering of electrons for anti-parallel configuration of magnetizations. For the same reason, GMR effect in Co/Cr and Fe/Cu multilayer structures is not that strong, as there is significant lattice as well as band mismatch in both up and down channels between Co-Cr and Fe-Cu.

Together with lattice and band matching, GMR as well as TMR ratios can have strong or weak dependence on many other factors related to growth and processing of thin films and also on film thicknesses of different layers in the stack. GMR and TMR ratios can also significantly depend on temperature - often increasing 2-3 times with decreasing temperature from room temperature to liquid helium temperature. The non-magnetic layer thickness and interface roughness also have strong effects on GMR/TMR ratios. Electron-phonon interactions increase with increasing temperature, and although this interaction is spin independent, the overall resistance of the stack increases with increasing electron-phonon interaction as the electron mean free path is shortened with increasing temperature. Because of increase in overall resistance of the stack, the GMR effect is suppressed and a reduced GMR is observed with increasing temperature. Spin fluctuations may also become significant with increasing temperature. Electron-magnon scattering is associated with spin-flip processes inter-mixing the majority and minority channels. With increasing temperature, these intermixing increases because of increasing spin fluctuations and inevitably suppressing the effective spin polarization and thus the magnetoresistance effect. In the case of materials with low Curie temperatures, this decrease in GMR or TMR ratio can be quite significant as we increase the temperature from liquid helium to room temperature.

For the nonmagnetic layer thickness dependence, very thin nonmagnetic layers may allow coupling between the ferromagnetic layers because of the presence of pin holes or roughness in the nonmagnetic layer, reducing the magnetoresistance effect. A nonmagnetic layer which is too thick will reduce the magnetoresistance as the electron scattering probability increases with increasing thickness. Thicknesses in between these two extremes, the magnetoresistance is found to oscillate [26, 27, 28]. Interlayer exchange coupling makes GMR ratio to oscillate while in MgO based MTJ, TMR ratio oscillate because of the oscillation of R_{AP} andR_P with increasing MgO thickness (still not fully understood) [17]. High interface roughness decreases the GMR ratio as inter-diffusion may change the magnetic state of the ferromagnetic layer at the interface region. From technological point of view, the resistance and area product (so called the RA product) is a very important parameter for a GMR or TMR device as more energy is lost by Joule heating in a device with high RA product. In recent years, high TMR ratios have been observed at room temperature in CoFeB/MgO/CoFeB based structures [29, 30]. CoFeB is a soft and amorphous magnetic material. Crystalization of CoFeB at both MgO interfaces leads to symmetry filtering in this structure like in Fe/MgO/Fe structure giving very high TMR ratio at room temperature with enhanced magnetic switching properties. High TMR ratio at room temperature has also been observed in MTJs with heusler alloys as well [31]. Like CrO_2, Heusler alloys also belong to the class of materials called half-metals. Half-metals are briefly introduced in the following section.

2.2.2 Half-metals

Half-metals are ferromagnetic material with a band gap around the Fermi level for one spin (density of states in CrO_2 is shown in fig. 2.7). Because of this gap, there is no conduction of electrons from their valance band to conduction band for the minority electrons, and as a result the conduction electrons in a half-metal are completely spin polarized. Although this is the ideal case for half-metals at absolute zero temperature, real half-metals do show much higher spin polarization than 3d ferromagnetic elements Fe, Co and Ni (close to 40%). Most half-metals are highly sensitive to variation in composition and this makes thin film growth of half-metals not easy example, CrO_2 has a very narrow temperature window for deposition and well above room temperature (section 3.2).

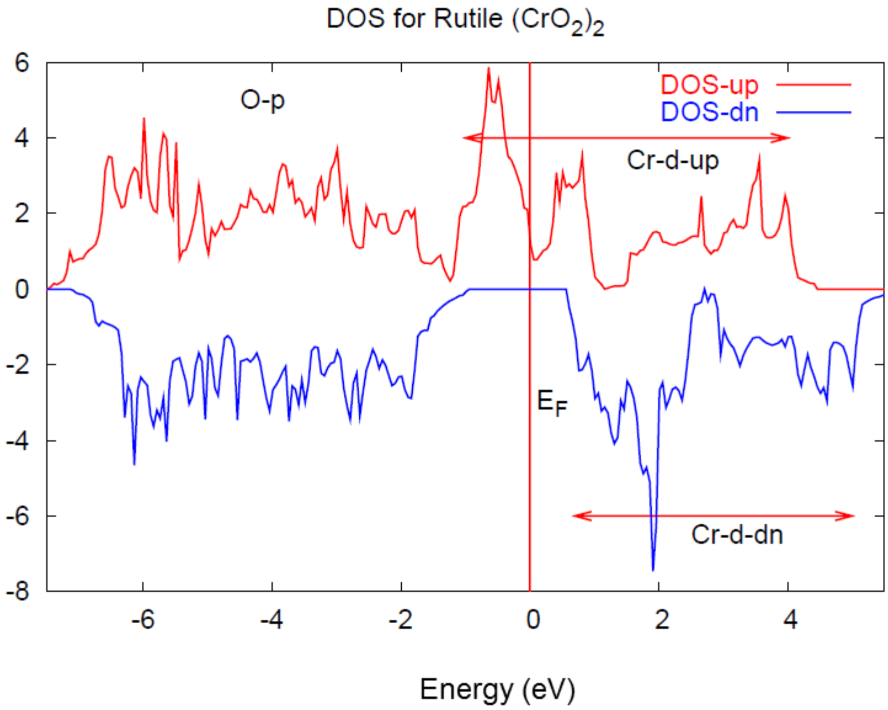

Figure 2.7: Density of states of $CrO_2$for up and down spin electrons (calculated by C. S. Liu and Dr. W. H. Butler). Minority electrons have a band gap of about 1.0 eV around Fermi level.

Depending on the nature of the band gap, half-metals are divided into three categories: (1) covalent band gap (2) charge transfer band gap (3) d-d band gap. An example of covalent band gap material is NiMnSb while CrO_2 is an example of charge transfer band gap material. The band-gap in d-d band-gap material occurs because of crystal field splitting of the bands. Co_2MnSi, Fe_3O_4 are examples of d-d band-gap materials.

In a 3d magnetic material such as in Co, the 4s band crosses the Fermi level and both spin up and spin down electrons are carried by this 4s band. If 3d and 4s bands are reordered by hybridization, we can observe the band gap that is necessary for a half-metal. For hybridization, we need more than one element and therefore all half-metals are either alloys or compounds. Because of hybridization, the 4s band is pushed above Fermi level while the 3d band is pushed below Fermi level and in that way we get an energy gap. Based on composition, half-metals are divided into two classes as Heusler alloys and oxides. Heusler alloys are again of two types: half Heusler alloys (XYZ) with $C1_b$ structure and full Heusler alloys, (X_2YZ) with $L2_1$ structure. Here X and Y represent transition metals and Z is either a semiconductor or a nonmagnetic metal. NiMnSb is a half heusler and Co_2MnSi is an example of full heusler alloy. Theoretically, large numbers of heusler alloys are possible. More than being of fundamental interests, Heusler alloys have gained considerable importance for spintronic devices because of their half-metalicity and because of their Curie temperature much higher than room temperature. Among oxide half-metals, CrO_2 and Fe_2O_2 are examples of binary oxide half-metals and $La_{0.7}Sr_{0.3}MnO_3$, Sr_2FeMoO_6 are examples of quaternary half-metals. These complex oxide half-metals have been of great interests because of their fundamental material properties. Fe_3O_4 exhibits metal-insulator transition below 120 K while recently, high TMR ratio has been observed in LSMO based devices [32].

Among all oxide materials, CrO_2 has been most extensively studied in recent years because of it has the highest measured spin polarization among all known materials [5, 6]. Among many oxides chromium forms such as Cr_2O_3, Cr_2O_5, Cr_3O_8 etc, Cr_2O_3 is thermodynamically the most stable. CrO_2 is a meta-stable oxide of chromium that stabilizes within narrow temperature range of 370 °C to 400 °C under high oxygen pressure(fig. 2.8), crystallizing in a tetragonal rutile structure. Curie temperature of CrO_2 is around 395 K and it has a moment of 2.0 μ_B per formula unit at absolute zero temperature. When heated above 450 °C, CrO_2 starts irreversibly transforming into Cr_2O_3 [33] . CrO_2 also exhibits some fascinating properties among which most notable are its selective growth and lateral overgrowth on a patterned surface [34], columnar growth on Al_2O_3 substrate

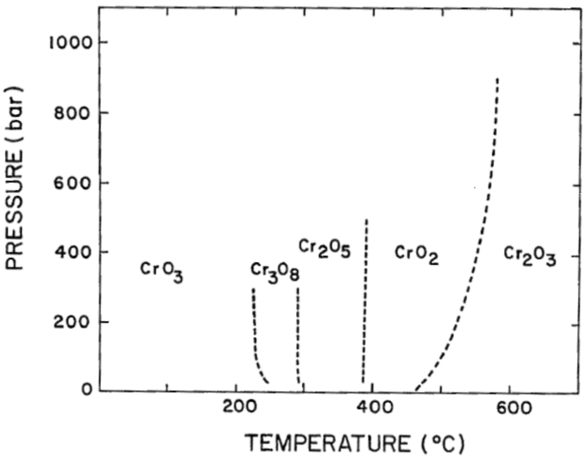

Figure 2.8: Temperature-pressure phase diagram of chromium oxide systems taken from ref. [33]. CrO_2 is stable around 400 K at atmospheric and higher pressure. Dashed lines represent the approximate phase boundaries between different oxide phases.

[35] and substrate-induced strain controlled magnetic anisotropy in (100) CrO_2 films that also depends on temperature and film thickness [36]. All these properties make CrO_2 a very interesting material for fundamental studies as well as for spintronic applications. So far, most of the work on CrO_2 have been on (100) oriented films that were found to be strained. Other low indexed directions such as (110) have not been explored much for their film properties. Also, the surface/interface properties of CrO_2 and various factors affecting them are relatively unknown. Exploring the fundamental thin film properties of CrO_2 and realizing spintronic devices with CrO_2 as a ferromagnetic electrode has been a topic of highly focused work at the MINT Center, University of Alabama and major findings of this work have been reported and discussed in this dissertation.

Chapter 3

EXPERIMENTAL METHODS

3.1 Introduction

In this chapter, working principles of the major instruments that were used during this research work are briefly described and some characteristic results obtained and analyzed using these instruments in this project are shown. All instruments can broadly be divided into three groups: instruments used for (a) thin film preparation (b) thin film characterization (particularly structural, surface and magnetic characterization of thin films) and (c) transport measurement on thin films and fabricated devices.

CrO_2 films were deposited using chemical vapor deposition (CVD) and TMR devices were fabricated using photo-lithography. The device fabrication process also involves ion beam etching, and sputtering or e-beam evaporation of SiO_2 for insulation and Co and Au for top magnetic electrode and contact respectively. X-ray diffraction (XRD) technique was used for detailed structural study of (100) and (110) oriented CrO_2 films. Atomic force microscope (AFM) was used to study surface morphology of TiO_2 substrates and CrO_2 films deposited on those substrates. Vibrating sample magnetometer (VSM) and superconducting quantum interference device (SQUID) were used to study the magnetic properties of CrO_2 thin films. Scanning electron microscope was used for film imaging at high magnifications, for composition study with energy dispersive X-ray (EDX) analysis and for preparation of nano-dots with e-beam lithography that will be integrated in future with our device fabrication process. X-ray photoelectron spectroscopy (XPS) was used to study film surface composition. All these techniques with their working principles are mentioned in this chapter. XMCD, an advanced magnetic characterization technique is explained in chapter 5 and low pressure deposition of CrO_2 films is described in chapter 6 in this dissertation.

3.2 Chemical vapor deposition

In this method of thin film preparation, a volatile compound reacts with one or more gases to produce a non-volatile compound that is deposited on a substrate. Unlike the physical vapor deposition (PVD) technique, there is no transfer of material from target and no directional dependence of deposition. Film growth in CVD is conformal. Also, very good high vacuum is not necessary in CVD as well as application of high electric potential. The chemical reaction in CVD can be activated thermally, by plasma or by photons of particular wavelength. A wide variety of materials can be deposited using the CVD technique and it is very efficient and popular for deposition of semiconductors in industry. In case of CrO_2 films, the reaction is thermally activated according to the method by Ishibashi et al [37]. As shown in figure 3.1, a CrO_3 precursor is kept at 260 °C in one chamber and TiO_2 substrate is kept in the other chamber at 400 °C. Oxygen flowing at 100 sccm (standard cubic centimeter per minute) at atmospheric pressure carries the precursor and it thermally decomposes on the TiO_2 substrate to give CrO_2 films. The precursor temperature, substrate temperature, and oxygen flow rate are the most important parameters for deposition of CrO_2 films.

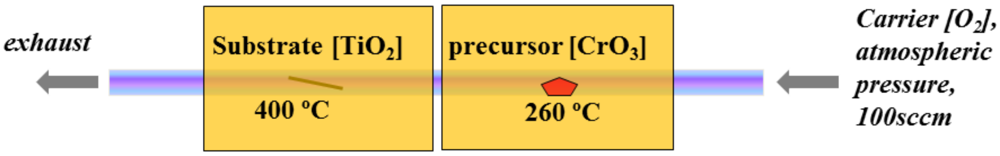

Figure 3.1: Schematic diagram of CrO_2 deposition system.

3.3 Sputtering

When a gas is kept under low pressure and high voltage is applied, the gas molecules ionize as positive ions and electrons. The positive ions move towards the cathode and the electrons move towards the anode. This ionized state of the gas with moving charges is called plasma - the forth state of matter. This plasma can be used for thin film deposition (invariably, argon is used for obtaining plasma). The material to be deposited is the cathode, and cations with high kinetic energy transfer their momentum and energy to the surface molecules on the target. These molecules leave the target and get deposited on the suitably placed substrate. Metals, semiconductors as well as insulators can be deposited using sputtering to obtain thin films with very good stoichiometry. Ultra high vacuum ($\leq 10^{-7}$ Torr) before deposition is required for sputtering to obtain very good structural and compositional quality of deposited thin films free of impurities. Magnets with alternate north and south poles are used under the target to increase deposition efficiency by confining the secondary electrons generated when cations hit the target (this is called magnetron sputtering). Radio frequency (RF) voltage is used for deposition of insulating materials in sputtering as insulators are conducting to these frequencies. Plasma generated by applying RF voltage on the insulating target removes the molecules from the target. An impedance matching network consisting of a combination of variable capacitors and inductors are necessary for maximum power delivery in RF sputtering. The frequency 13.56 MHz is used in RF sputtering power supplies [38].

Deposition rate in sputtering increases linearly with increasing power between the target and the substrate and it decreases with increasing pressure of argon due to the decrease in mean free path of ions (mean free path is the average distance ions travel between successive collision). Sputter yield maximum for 45 ° angle between the target and incident ion direction however, it is usually not necessary to maintain this angle because of different designing of systems with different requirements. Co and Au were sputtered using a home build sputtering machine (named Shirley) with deposition rate for both of about 0.05 nm/s at base pressure of $\sim 5\times 10^{-7}$ Torr and Ar pressure of 5 mTorr for our TMR devices.

3.4 Ion-beam etching

Ion beam etching is a physical process to selectively remove material from a thin film. As shown in the schematic diagram below, electrons coming out of the neutralizer

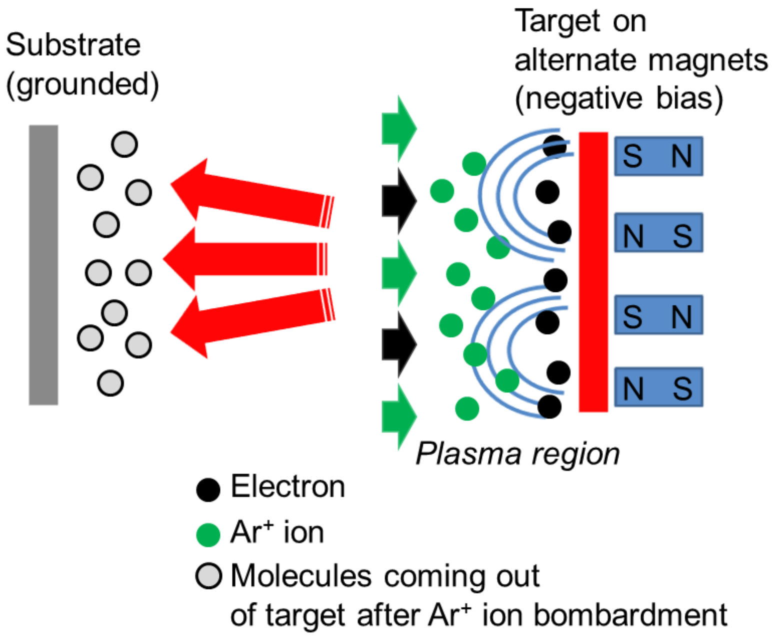

Figure 3.2: Schematic diagram of magnetron sputtering.

are attracted by the RF magnetic field. On their way, electrons charge the inert Ar gas molecules and plasma is created in that way. A suppressor with negative voltage (not shown) is used to extract the ions and an applied high voltage between the film and source of ions accelerates the ions towards the film. Recombination of Ar^+ ions and the electrons from the neutralizer helps in reducing the charge build up on the film. Momentum transfer between the neutralized Ar ions and the molecules in the film knocks them off from the film. Like in sputtering, ion milling rate also depends on the beam energy (i.e. applied voltage), density of the etched material and the angle of incidence. Light atoms are removed easily while heavier atoms require higher energy to be removed. Highest etching rate is obtained at an angle of incidence of 45 °. Since ion milling is a high energy bombardment process, it can structurally damage a film surface. To minimize re-deposition of the etched material, after the initial milling at 45 ° the structure is ion milled at low angle of incidence for short time to remove the particles that gets re-deposited on the side.

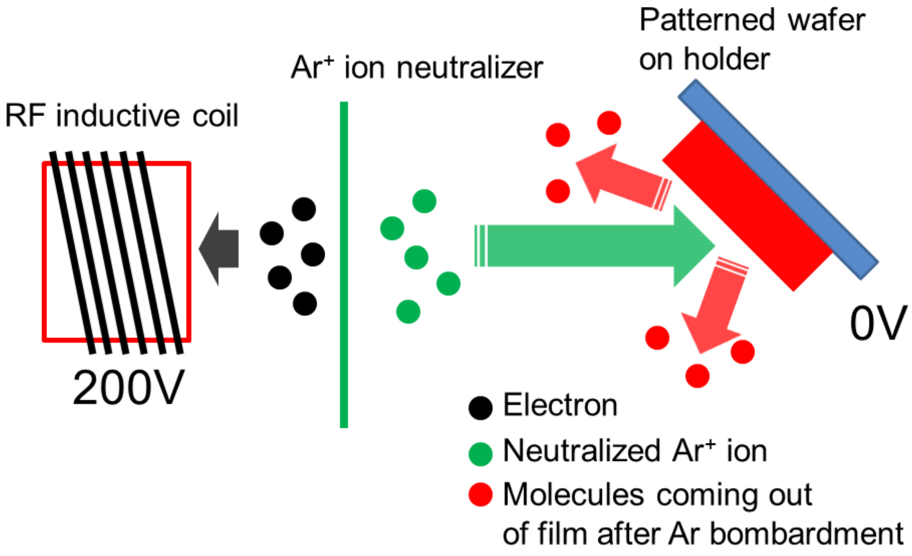

Figure 3.3: Schematic diagram of ion beam etching.

3.5 Electron beam evaporation

In this method, a focused electron beam is used in vacuum to heat and evaporate the material to be deposited. A tungsten wire is heated by applying very high voltage (1-10 kV). When the wire is sufficiently heated, it emits electrons (thermionic emission) and these electrons are deflected, accelerated and focused on the material to be deposited contained in a crucible. The energy of these focused electrons is transferred to the material over a small area and its vapor pressure increases sufficiently for deposition. This vapor inside the chamber produces coating of the material on substrate. Varieties of metals, insulators and alloys can be evaporated using e-beam evaporation. For our TMR devices, SiO_2 was deposited for insulation using e-beam evaporation at 0.1 nm/s deposition rate with base pressure 2×10^{-6} Torr.

3.6 X-ray diffraction and reflection

X-rays are photons with energy 100 eV-100 keV in the electromagnetic radiation spectra. Wavelengths of X-rays are comparable to atomic length scales, and therefore X-rays are used to study structural properties of matter. Penetration depths of X-rays

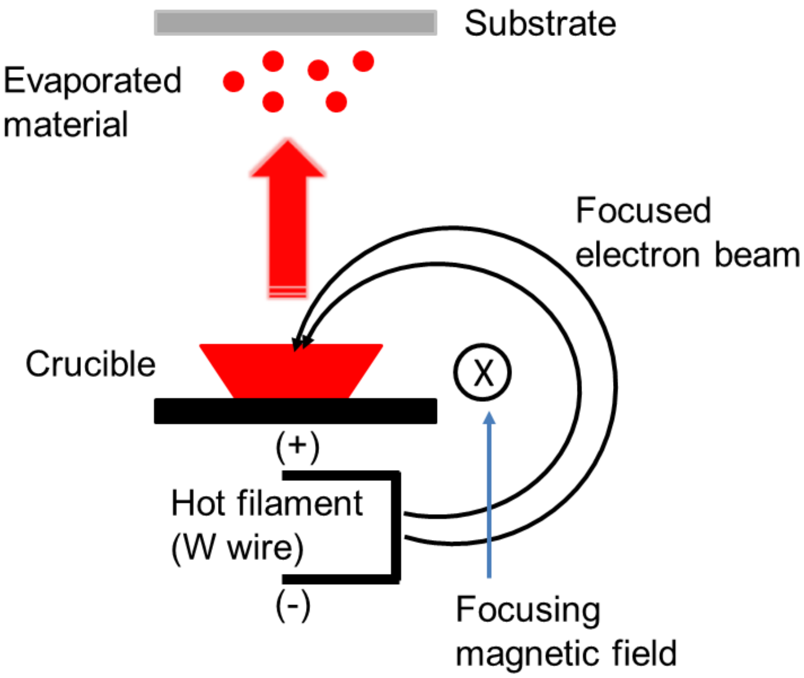

Figure 3.4: Schematic diagram of e-beam evaporation.

are very high and therefore the structural properties not only in thin films but also of bulk materials can be probed with X-rays.

X-rays are generated by transition of inner shell electrons in atoms (characteristic X-rays) and also due to transition in nuclear energy levels (continuous X-rays). When a high energy electron beam coming out of a source (tungsten in our Philips X′Pert machine) is accelerated by applying very high voltage (∼45 kV) and focused on a solid target (the source of X-ray, a Cu block in our case), X-rays are generated from the target. Accelerated electrons eject K inner shell electrons and in that way available empty states are created in the K shell. Electrons from the next higher energy level L jump to K level by releasing the energy as X-rays. This X-ray radiation is called Kα and is the most intense among the X-rays generated from the atom. This Kα line is split into two lines as Kα_1 and Kα_2 because of hyperfine splitting (spin degenerate K levels). Similarly like in atomic energy levels, these high energy electrons also cause transition in the nuclei. Electrons are decelerated by the collision with the nuclei and the X-rays coming out of the nuclei form the background in the X-ray spectra generated from the source.

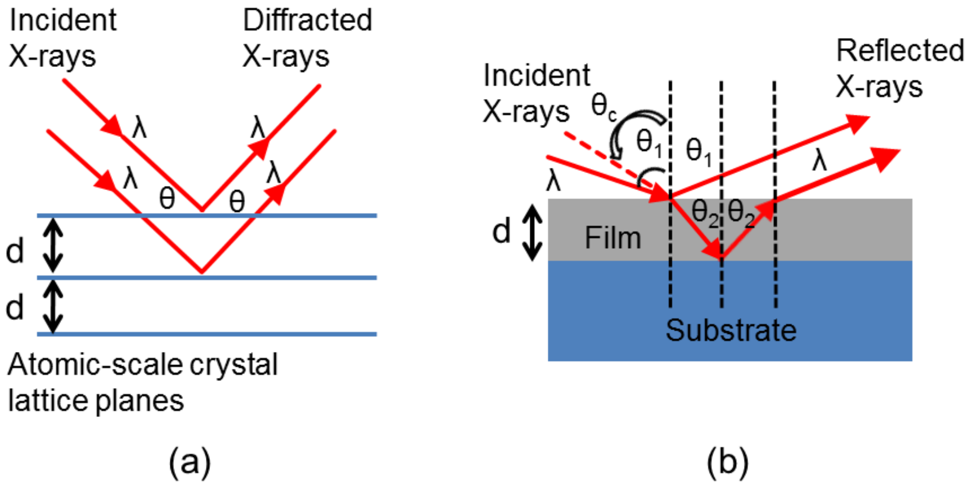

Figure 3.5: Schematic diagram of (a) X-ray diffraction from crystal lattice planes and (b) X-ray reflection from air-film and film-substrate interfaces of a single layer film on a substrate.

Now, the X-rays coming out of the source are incident on the material under investigation and interact with its atoms. X-rays can undergo inelastic scattering (loss of energy and change in wavelength e.g. Compton scattering) as well as elastic scattering (energy and wavelength do not change) with these atoms. When we have periodic arrangement of atoms in the material and atomic distances comparable to the X-ray wavelength, constructive interference of the elastically scattered X-rays from each atomic layer produces sharp intensities collected by the detector (diffraction pattern). These sharp diffraction intensities or the peak positions are related to the atomic distances by Braggs law of diffraction:

$$2dsin\theta = n\lambda \tag{3.1}$$

Where d is the atomic spacings and λ is the X-ray wavelength (=0.1541 nm for our Cu Kα source installed in Philips X′Pert machine). Depending on the geometry of the diffractometer, atomic spacing in different directions of a crystal can be calculated using Braggs law. This technique is known as X-ray diffraction (XRD) was used to investigate substrate-induced strain in (100) and (110) CrO_2 films and to determine the lattice constants as reported in chapter 3.

When X-rays are incident at small angles on a surface, we can observe X-ray reflection (incident angle is equal to reflected angle) and X-rays also penetrate material when angle of incidence is bigger than some critical angle (θ_c). The intensity of reflected X-rays depends on angle of incidence, thickness, surface roughness and density of material. In case of a single layer thin film deposited on a substrate, we can observe oscillations in the reflected X-ray intensities because of the interference of X-rays reflected from air/film interface and film/substrate interface.The path difference between the reflected waves for a film of thickness of t is given by,

$$\Delta = 2t\sqrt{sin^2\theta_n - sin^2\theta_0} \tag{3.2}$$

Here, n is an integer, λ is X-ray wavelength, θ_n is peak position in radian in nth oscillation and θ_0 is the 0th order peak position. For small angles of incidence, this expression can be written as,

$$m^2\left(\frac{\lambda}{2t}\right)^2 = \theta_n^2 - \theta_0^2 \tag{3.3}$$

Using this technique, known as X-ray reflection (XRR), thickness of single layer thin films can be determined within uncertainty of few few nanometers of error using this method. The thickness of multi-layered structure as well as film roughness can also be estimated from XRR data. Figure 3.6(a) shows the XRR of a single layer Co film sputtered on an oxidized Si substrate. Deposition rate of all thin films during the research work were estimated from the thickness measurement using XRR.

3.7 X-ray photoelectron spectroscopy

X-ray photoelectron spectroscopy (XPS) is a surface analysis technique as soft X-rays (energy ≤1 keV) are used in this technique that can penetrate 1-10 nm on a sample

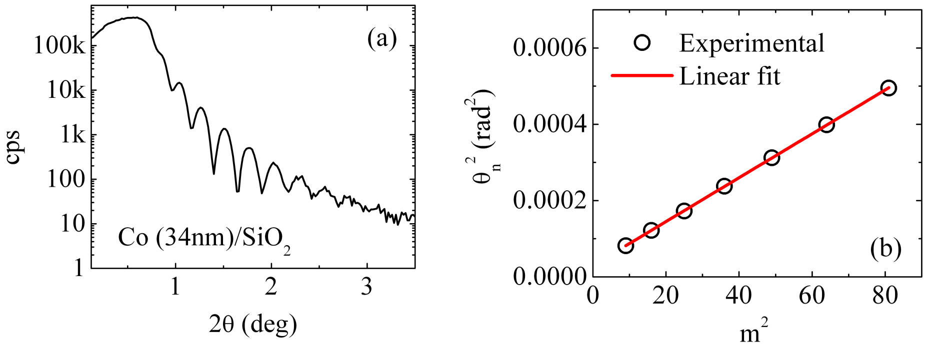

Figure 3.6: (a). XRR pattern of a Co film deposited on SiO_2 substrate. Reflection intensity is plotted against angle of reflection. (b) Plot of θ_n^2 vs. m^2 and linear fit using expression 3.3 are shown. Thickness of the film determined by straight line fit was same as obtained using WINGIXA software (34 nm).

surface. XPS is mainly used to determine element composition, chemical or electronic state of elements and to detect impurities or contamination on the surface region of a sample. XPS can detect all elements except hydrogen and helium. XPS technique works on the principle of photoelectric effect. When a monochromatic beam of X-rays strikes the sample surface, it can generate photoelectrons if the photons have higher energy than the binding energy of the electrons. The kinetic energy of a photoelectron is governed by the following relation,

$$KE = \hbar\omega - [BE + \Phi] \tag{3.4}$$

Here, $\hbar\omega$ is energy of the photon, BE is the binding energy of electron and Φ is the work function of the spectrometer (of the order of few eV). Binding energy is due to the attraction between electrons and the nucleus provided to the electrons by the incident photons to make them free from the atom. Work function is a parameter of the spectrometer and therefore depends on the instrument and is determined by calibration. By conservation of energy, the rest of the available energy is the kinetic energy of the ejected photoelectrons. So, electrons with higher (lower) binding energies have lower (higher) kinetic energy. Electrons coming out of different elements and from different

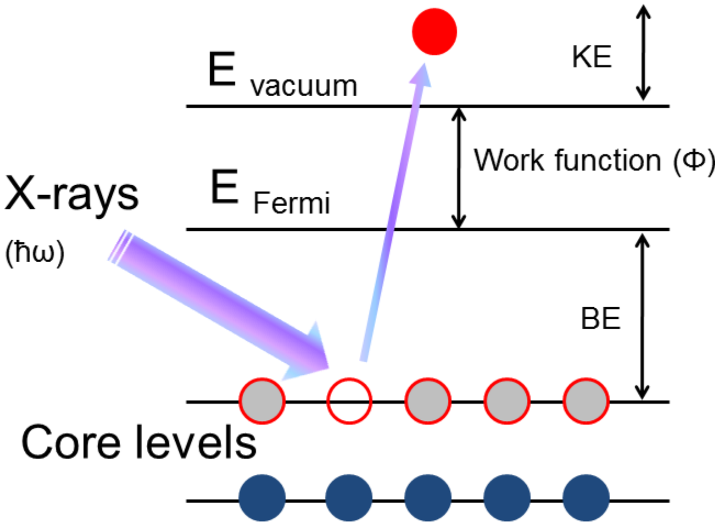

Figure 3.7: Schematic diagram of atomic transition in XPS.

energy levels have different kinetic energies (or velocities) and are captured and detected for their binding energies by a spectrometer.

3.8 Atomic force microscopy

Atomic force microscopy (AFM) is a scanning probe technique used to image surface structures. When the tip is far away from the surface, there is no deflection of the tip. As the tip is brought down towards the surface, it experiences a van der Waals attractive force for a certain distance between the surface molecules and the tip and as a result the tip is deflected. When we further decrease the distance between the tip and the surface, the tip experiences Coulomb repulsion from the surface molecules and as a result it is deflected in the other direction. The force between the tip and the surface is within 0.1 nN-1 nN, and the deflection can be as small as 0.01 nm. In order to detect these small deflections, a laser beam is focused and reflected from the back side of a cantilever holding the tip towards a position sensitive photodetector. The position of the reflected beam changes according to the deflection of the cantilever and the photodetector converts these changes into electrical signal. AFM works in two different modes - contact mode

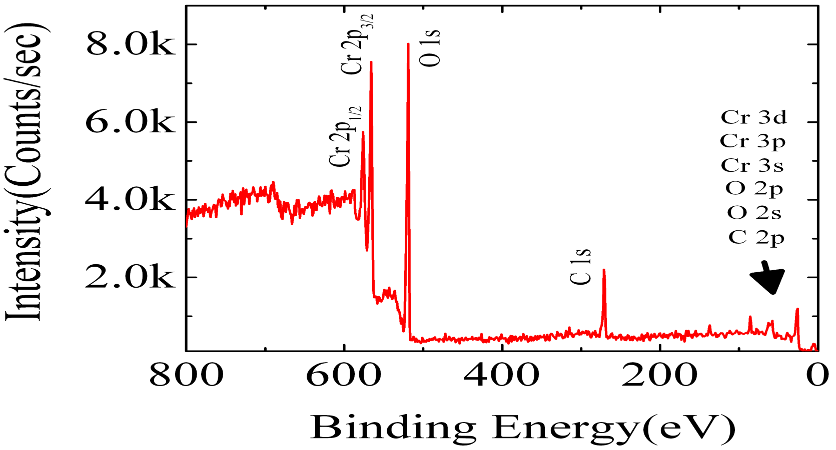

Figure 3.8: Chromium and oxygen along with carbon as a surface contamination were identified on the surface region of a CrO_2 film prepared with low pressure CVD technique on a (100) TiO_2 substrate using XPS technique. Intensities of ejected photoelectrons are plotted against their binding energies. Peak positions below 200 eV are not individually identified as they are close to one another with low intensities. Surface elements on the film were detected without any treatment of the film after deposition. Carbon is usually seen as a surface contamination since the film was exposed to air for long enough time before putting inside the chamber. The monochromatic X-ray here is the Al Kα (1486.6 eV) line and the base pressure during scan was less than 10^{-9} Torr.

and tapping mode. In contact mode, the tip is in mechanical contact with the surface. Force is measured in this method by keeping the deflection constant and adjusting the vertical position of the tip. In tapping mode, the cantilever vibrates near its resonance frequency. Deflection is measured at the photodetector due to the change in oscillation amplitude as well as change in resonance frequency as the tip moves towards and away from the surface. Tapping mode is less damaging than contact mode and all AFM images taken during this work are in tapping mode. Figure 3.9 shows the atomically flat (110) TiO_2 surface imaged with tapping mode AFM on a 1×1 μm^2 area. Steps were obtained by cleaning the substrates with 12% HF solution in deionized water for 30s and then annealing at 1000 °C for three hours in oxygen flow of 1.5 L/min. Steps are observed because of surface relaxation of the slightly miscut substrates upon high temperature annealing.

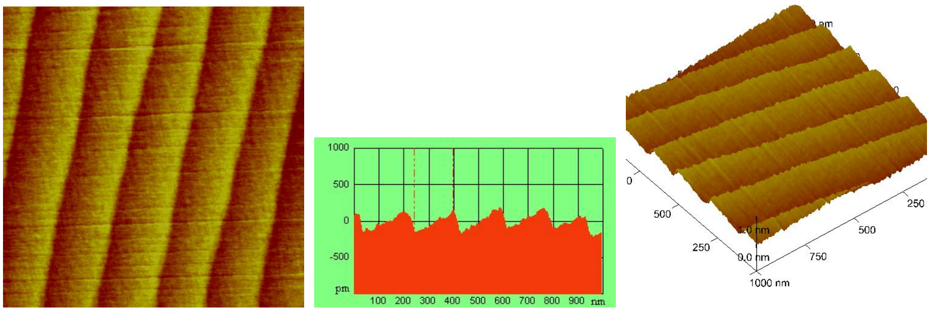

(a) (b) (c)

Figure 3.9: (a). 2D view of the atomically flat (110) TiO_2 substrate. (b) Section view of the same surface. Steps of width 150 nm and height 0.3 nm are observed. (c) 3D view of the steps shown within a height scale of 1 nm.

3.9 Vibrating sample magnetometer

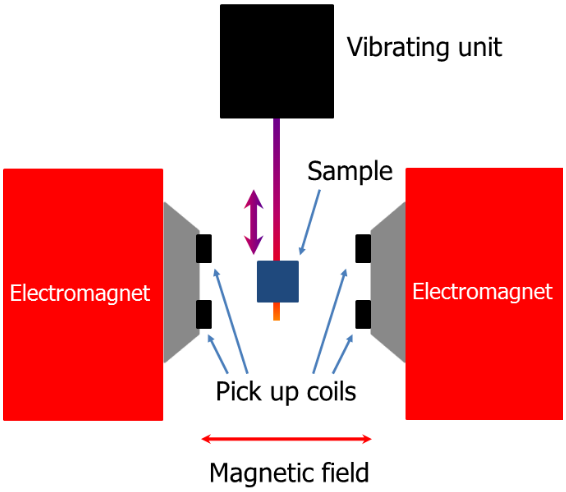

Figure 3.10: Schematic diagram of a VSM.

Vibrating sample magnetometer (VSM) works on the principle of Faradays law of induction (a change in magnetic flux produces electric current in a closed circuit) and is used to study the magnetic properties of thin films and bulk materials. The sample is placed between the poles of a magnet and a constant magnetic field is applied to magnetize the sample as shown in figure 3.10, the schematic for VSM. The magnetic moments in the sample align in the direction of the external field to create a magnetic dipole moment in the sample and this dipole moment creates a small magnetic field around the sample. When the sample vibrates (at 85 Hz in our DMS 1660 VSM), by Faraday's law the time varying magnetic flux due to this dipole moment can be picked up by the "pick-up" coils placed close to the sample as stated by Faradays law. The current in the pick-up coils will be proportional to the magnetic moment and therefore bigger the volume of magnetic material in the sample, bigger the induced current. Magnetic moment of the sample at different magnetic field can be obtained in this way. VSM was used to determine magnetic hysteresis loops (magnetic moment obtained by varying the external magnetic field) and to study the magnetic anisotropy in thin films during this research work.

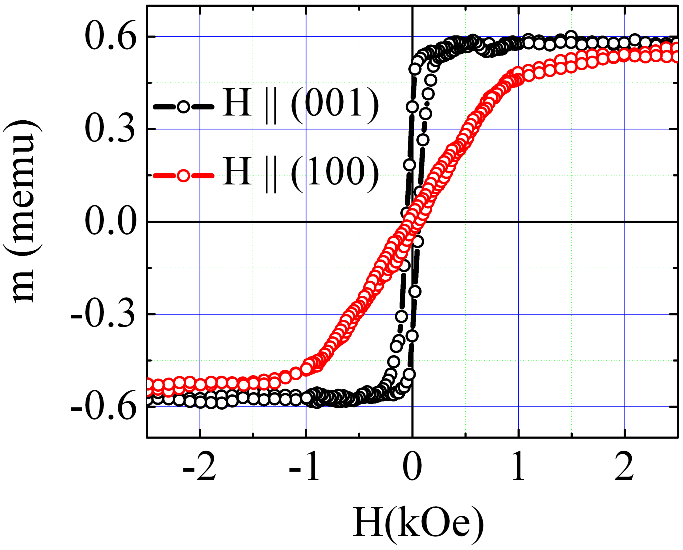

Figure 3.11: Room temperature M(H) loops of a CrO_2 film deposited by low pressure CVD and measured in VSM when the applied field is in-plane and along the (001) and (100) directions in the TiO_2 substrate. (001) and (100) are the easy and hard axis directions in the film respectively. Coercivity was about 65 Oe and in-plane anisotropy field is about 1 kOe for this particular film of thickness about 55 nm. [cgs to S.I. conversion factors: 1 Oe=79.57 A/m, 1 emu=10^{-3} A/m^2]

3.10 Superconducting quantum interference device

Like VSM, superconducting quantum interference device (SQUID) is also a magnetometer that can be used to measure magnetic properties of material however. However, it needs cryogenic refrigeration with liquid helium. Magnetic moments measured in a SQUID are generally more accurate than those measured with VSM because of its very high sensitivity. Also, magnetic moments can be measured from liquid helium temperatures to 350 K using magnetic fields as high as 5 T in our SQUID system (Quantum design MPMS). The working principle of a SQUID is based on the Josephson affect. When we have two superconducting junctions in parallel (a junction is two superconductors separated by insulator or vacuum), the tunnelling current oscillates as a function of magnetic flux. It is expressed according to the following relation [39],

$$I = I_0 \frac{sin\left(\pi\Phi/\Phi_0\right)}{\pi\Phi/\Phi_0} \tag{3.5}$$

where Φ is the total magnetic flux in the junction, Φ_0 is the flux quantum (= hc/2e = $2.07\text{x}10^{15}$ Wb) and I_0 depends on the temperature and structure of the junction but not on magnetic field. The variation of flux is very sensitive and thus the SQUID is very sensitive to changes in magnetic flux and therefore to change in magnetic moment.

3.11 SEM and EDX

In scanning electron microscope (SEM), electron beam is used instead of light for imaging. SEM is also used to perform e-beam lithography (fig. 3.13) and quantify elements in a sample (fig. 3.14). Much higher resolution than in optical microscope is achieved in SEM because of small wavelength of electrons (0.2-0.5 $\AA$) at the energies used. A beam of electrons is generated by applying high voltage (2-30 kV) in ultra-high vacuum between the specimen (anode) and the source of electron (cathode). The source of electron in our JEOL JSM-7000F SEM is a zirconium coated single crystal tungsten wire with tip diameter below 100 nm. The beam of electrons is focused and scanned on the specimen

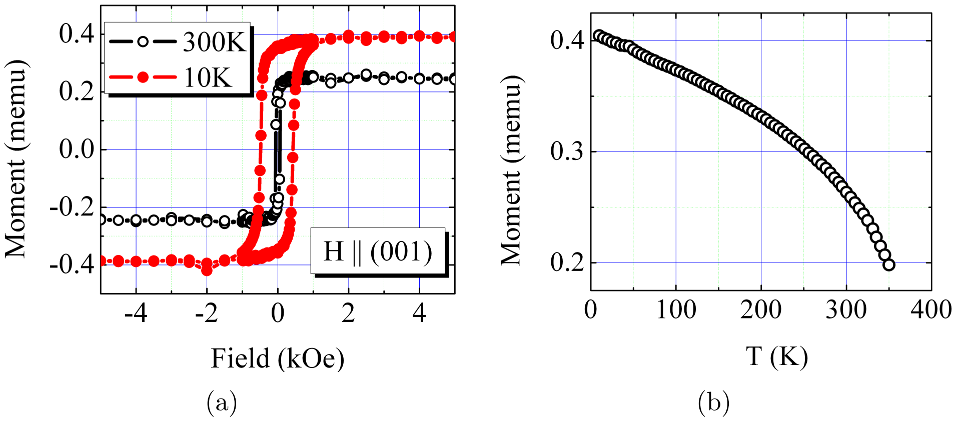

Figure 3.12: (a) M(H) loops of a CrO_2 film prepared with low pressure CVD and measured with SQUID at 10 K and 300 K. Moment as well as film coercivity increased as temperature was decreased from 300 K to 10 K. (b) Magnetic moment vs. temperature of the film from 10 K to 350 K measured in SQUID. Magnetic field of 5 kOe was applied along the c direction to saturate the magnetization during the measurement.

using magnetic lenses. Auger electrons, secondary electrons, backscattered electrons and characteristic X-rays are generated due to the interaction between the incident beam of electrons and the elements in the specimen. Auger process occurs at the surface level of the specimen. Secondary electrons have low energy (0-50 eV) and therefore secondary electron detector is placed closer to the specimen. Backscattered electrons are a result of the elastic scattering between the incident electrons and the nuclei in the specimen. When incident electrons knock off core level electrons, electrons from next higher energy level fill the empty state and characteristic X-rays are generated in this process. These electrons and X-rays are collected to get information about the specimen. The contrast in imaging is obtained from the numbers of secondary and backscattered electrons that are generated. Similar to XPS, the X-rays generated are unique characteristic of the elements present. The signal from collected X-rays is proportional to the concentration of the elements present and therefore used to quantify the elements present (working principle of energy dispersive X-ray analysis (EDX)).

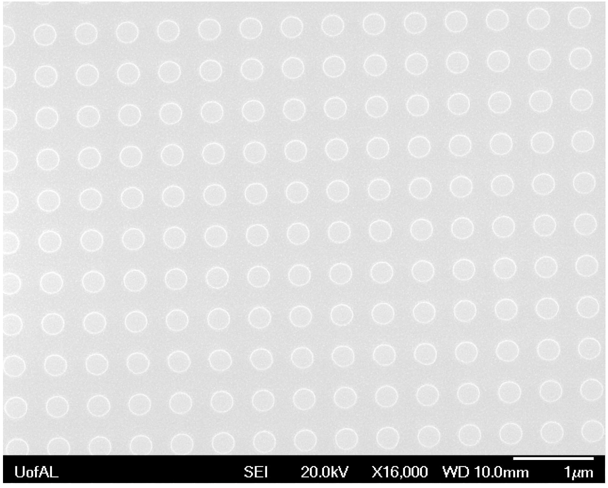

Figure 3.13: SEM image of 250 nm dot-arrays prepared with e-beam lithography

3.12 Photo and e-beam lithography

Photolithography is widely used for printing or patterning electronic devices. Patterns from a photomask (designed using AutoCAD, for example) are transferred by selective exposure of photoresists using UV light. Photoresists are chemicals that change chemical properties when exposed to UV light [40]. In case of a positive photoresist, when it is exposed to UV light the chemical bonds are broken and as a result they become soluble in a developer (we used MF 319 developer). In case of negative photoresist, when it is exposed to UV light they are polymerized and as a result become more difficult to dissolve in a developer. Features of sizes 3×5.5 μm^2 to 128×128 μm^2 were patterned following the photolithography process designed for fabricating $CrO_2/Cr_2O_3/Co$ TMR devices using positive resist 1818 and negative resist AZ 5214.

Resolution in photolithography is ultimately limited by the wavelength of UV light used. Much higher resolution can be achieved in e-beam lithography because of much smaller wavelength of electrons (0.2-0.5 $\AA$). Similar to photoresist, there are e-beam resist that acts as positive or negative when exposed with a focused electron beam. Negative e-beam resist was used to write the patterns showed in figure 3.15.

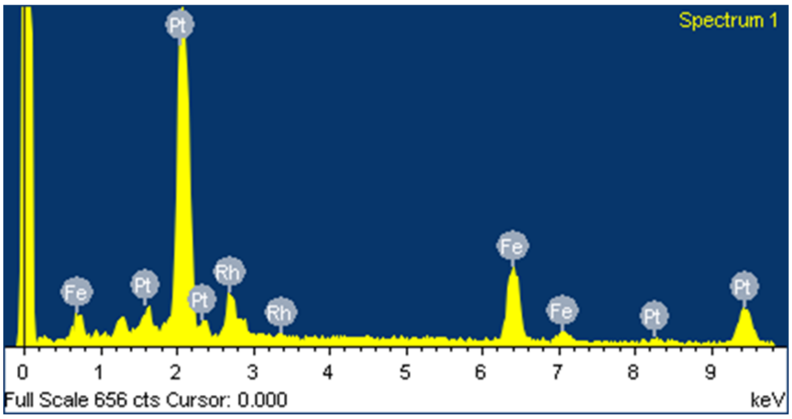

Figure 3.14: An example of EDX analysis performed on a FePtRh film. Scan on an area of 20 ×$20m^2$ showed Fe, Pt and Rh atomic compositions of 43%, 42% and 15% respectively in this film.

Following is a brief description of the positive and negative photoresist used along with the steps followed for fabricating the devices. These steps are not universal to all TMR devices as the CrO_2 film was exposed to air before top electrode deposition.

2.12.1 PR 1818 recipe:

Spin coating @ 4000 rpm, 30s; soft bake @ 115 °C, 60s; exposer : 3.5-12s [1000 W, $2mW/cm^2$, 350 W Hg, hard contact]; develop using MF 319 for 60s and clean resist; hard bake @ 115 °C for 5min.

2.12.2 PR 5214 recipe:

Spin coating @ 4000 rpm, 60s; soft bake @ 100 °C, 10min; expose: 3.5s [1000 W, $2mW/cm^2$, 350 W Hg, hard contact]; reversal bake: 10min @ 100 C in oven; flood expose: 9s; develop using MF 319 for 90s and clean resist. The reversal baking step is critical for photoresist 5214 as the area already exposed to UV light acts like positive resist after baking.

2.12.3 Device fabrication steps:

1. Deposited CrO_2 film using CVD blanket film (50nm) and natural Cr_2O_3 barrier.
2. Define bottom electrode using 1st mask and positive PR 1818.
3. IBE to TiO_2 substrate and remove resist.

4. Align 2nd mask on the line from 1st mask and pattern using PR 1818.
5. IBE (~5nm) to define junction area. Do not remove resist.
6. Deposit SiO_2 all over the film (e-beam evaporation) for thickness of 80nm.
7. Lift off (10min ultrasonic in acetone) and resist from 2nd mask is removed.
8. Define top electrode using 3rd mask and PR 5214 perpendicular to 1st mask pattern.
9. Sputter Co for free magnetic layer and Au for top contact. Then clean the resist.

These steps give the tunnel junctions with crossbar geometry and electrodes are wire bonded for transport measurement.

Figure 3.15: TMR device fabrication steps with CrO_2 as an electrode are schematically shown.

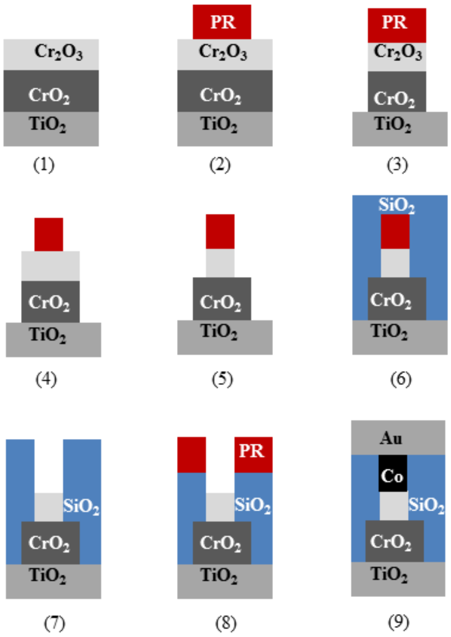

Chapter 4

SUBSTRATE-INDUCED STRAIN AND ITS EFFECT IN CrO_2 THIN FILMS

4.1 Introduction

Substrate-induced strain is a well-known phenomenon, especially in complex oxide thin films. Basically, it is the change in unit cell lattice parameters in thin films at the substrate-film interface region because of their *lattice mismatch*. Therefore, usually it is more pronounced in thinner films. In this chapter, a detailed investigation of substrate-induced strain in epitaxial (100) and (110) CrO_2 films as a function of film thickness and its consequences for films magnetic and transport properties are reported.

CrO_2 and TiO_2 are known to adopt the tetragonal rutile structure in bulk (CrO_2 rutile structure is shown in figure 4.1) with lattice parameters a=b=4.421 Å, c=2.916 Å for CrO_2 and a=b=4.593 Å and c=2.959 Å for TiO_2. This gives rise to lattice mismatch of 3.75 % along (100), (010), (110) and (-110) directions, and 1.45 % along (001) direction between CrO_2 and TiO_2. As a result of this lattice mismatch, substrate-induced strain is expected in CrO_2 films deposited on TiO_2 substrates with the degree of strain varying with growth orientation.

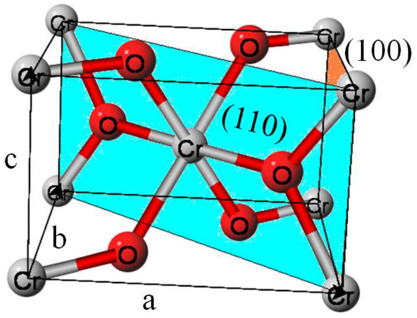

Figure 4.1: Unit cell of CrO_2. Cr^{4+} ions occupy the corner and central position and the O^{2-} ions occupy the octahedral sites around the central Cr^{4+} ion. Lattice directions and (100) and (110) planes in the unit cell are shown.

Substrate-induced strain in CrO_2 films is studied by determining the lattice constants from X-ray diffraction. The geometry for X-ray diffraction in our Philips XPert machine is shown in fig. 4.2.

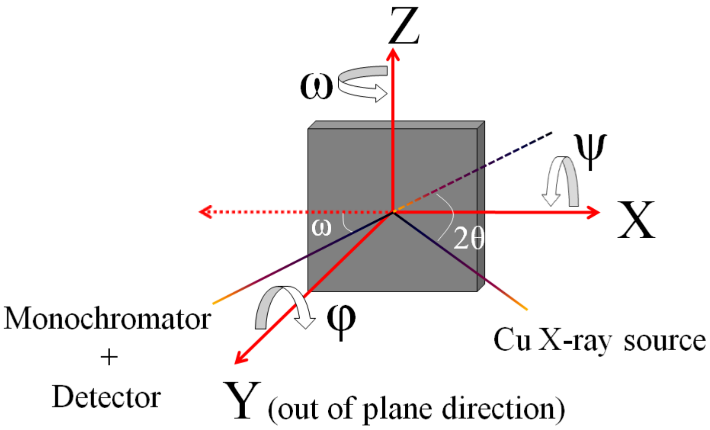

Figure 4.2: Schematic of the sample geometry for XRD, XRR and RSM in the Philips XPert system. Co-ordinate axes and rotation about each of them are shown. Here X, Y and Z are the (010), (100) and (001) directions in case of (100) CrO_2 films, while in case of (110) CrO_2 films, these directions are (-110), (110) and (001). Offsets in φ, ψ and ω angles are cleared (intensity is maximized) before a $(2\theta - \omega)$ scan.

4.2 Film epitaxy

CrO_2 films are known to grow epitaxially on isostructural TiO_2 substrates [41] and Al_2O_3 substrates [35]. Epitaxial growth was confirmed by performing φ-scans (fig. 4.3) and rocking curves (fig. 4.4) using a Philips XPert diffractometer. Very sharp peaks in the φ-scans confirmed films epitaxial growth on TiO_2 substrates meeting Braggs diffraction condition only at particular φ angles.

Small full width at half maximum (FWHM) obtained in rocking curves on (100) and (110) CrO_2 films grown on respective TiO_2 substrates indicate good film epitaxy on TiO_2 substrates. As seen in fig. 4.4, (100) films have smaller FWHM for the same thickness, presumably because they follow layer by layer growth mode while (110) films follow island growth mode [41].

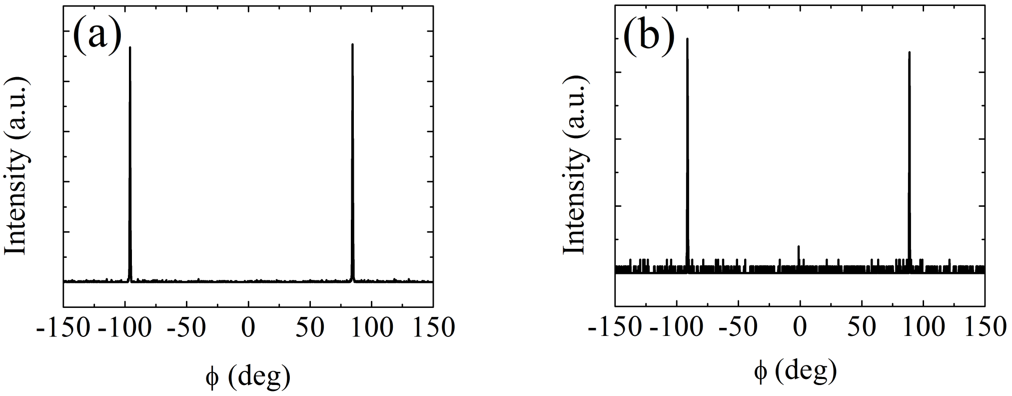

Figure 4.3: (a) φ-scan on (100) CrO_2 when (110) direction was out of plane. (b) φ-scan on (110) CrO_2 when (020) direction was out of plane. The sample thickness of both films was 100 nm. Both (100) and (110) CrO_2 films showed two-fold symmetry about these axes.

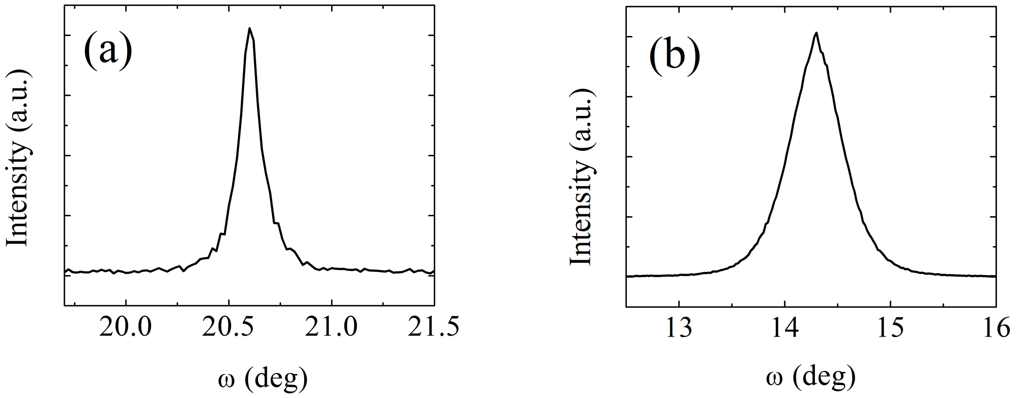

Figure 4.4:]

(a) Rocking curve on a (100) CrO_2 film with FWHM 0.12°. (b) Rocking curve on a (110) CrO_2 film with FWHM 0.57°. Sample thickness of both films was 45 nm.

4.3 Diffraction from different planes

Substrate induced strain in CrO_2 films was determined by $(2\theta - \omega)$ scan in XRD. 2θ positions in (100) CrO_2 films were found to be away from that in bulk CrO_2 along out of plane [38] as well as in other direction. In case of (110) CrO_2 films, 2θ position matched with that of bulk CrO_2 for out of plane [41] as well as for other directions. Few off-axis scans on (100) and (110) CrO_2 films are shown in fig. 4.5(a) and fig. 4.5(b) respectively.

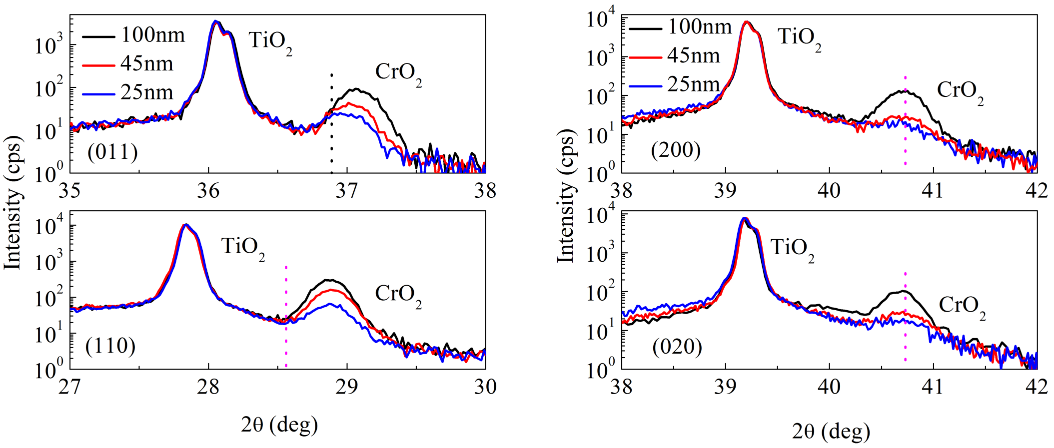

(a) (100) CrO_2

(b) (110) CrO_2

Figure 4.5: *2θ* diffraction peaks from (a) (100) and (b) (110) CrO_2 films for three different film thicknesses. Diffraction from the respective planes is mentioned. The dotted lines indicate 2θ position in bulk CrO_2 for respective plane.

4.4 Cohen′s method for determining lattice constants

To determine the lattice constants, namely a, b and c in the CrO_2 films, we employed Cohen′s method for a tetragonal system, described in [42, 43, 44]. Random errors are reduced in this method due to the least-square approach and the application of appropriate error function reduces possible systematic errors. According to this method, it is required to evaluate the constants A, B, C and D in the following 4.4 below and it is achieved by obtaining diffraction angles (2θ) for different planes:

$$sin^2\theta = Ah^2 + Bk^2 + Cl^2 + D\delta \quad with \quad \delta = 10sin^2 2\theta \left(\frac{1}{sin\theta} + \frac{1}{\theta} \right) \tag{4.1}$$

Here, A=$\lambda^2/4a^2$, B=$\lambda^2/4b^2$ and C=$\lambda^2/4c^2$. (h, k, l) are Miller indices of the relevant plane and the error function is δ. For the Cu X-ray source in the Philips X′Pert machine, λ=1.541Å. Diffraction positions (2θ) of the planes considered for Cohen′s method are shown in table 4.1.

Table 4.1: Diffraction angles from different planes of (100) and (110) CrO_2 films of three different thicknesses are listed. Diffraction angles from one plane in (110) CrO_2 films were found to be same for the three different film thicknesses. The angles have an accuracy of ±0.04°.

	2θ (°)				2θ (°)
(100) CrO_2	25 nm	45 nm	100 nm	(110) CrO_2	25, 45, 100 nm
(020)	41.30	41.21	41.14	(110)	28.52
(040)	89.70	89.45	89.21	(200)	40.70
(101)	36.65	37.02	37.07	(020)	40.70
$(1\bar{1}0)$	28.37	28.88	28.78	(211)	56.16
$(2\bar{1}1)$	56.39	56.38	56.38	(121)	51.16

4.5 Reciprocal space mapping on (100) and (110) CrO_2 films

In reciprocal space, Braggs diffraction condition is written as [45],

$$\Delta\mathbf{k} = \mathbf{q} \tag{4.2}$$

Therefore, from in fig. 4.6 we have,

$$q_x = k[cos(\theta - \omega) - cos(\theta + \omega)], \tag{4.3}$$

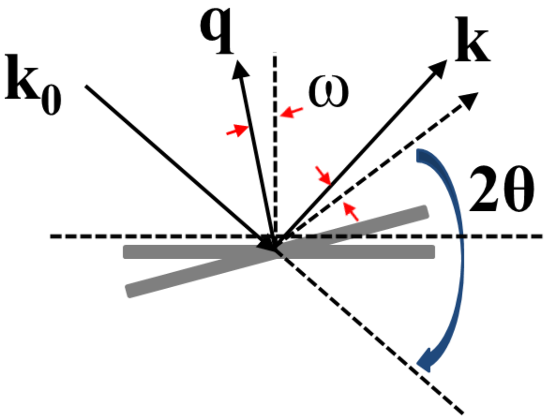

Figure 4.6: Schematic diagram of the RSM measurement from sample point of view. Rocking curve angle, ω is tilted around diffraction angle 2θ (2θ scans for different ω offset values). Here $\mathbf{k}_0$ is the incident wave vector, $\mathbf{k}$ is the scattering wave vector and $\mathbf{q}$ is the reciprocal lattice vector.

$$q_z = k[sin(\theta - \omega) + sin(\theta + \omega)] \tag{4.4}$$

where $k=k_0=2\pi/\lambda$ is the magnitude of the X-ray wave vector [46]. Here q_x is the in-plane component and q_z is the out-of-plane component of the scattering vector q. The plot of diffraction intensities from one or more planes for a range of q_x and q_z values is known as the reciprocal space mapping (RSM) of those particular plane(s). Essentially, RSM is 3D plot. The accessible region for data collection is $-2k \leq q_x \leq 2k$ and $0 \leq q_z \leq 2k$ with the condition that $q_x^2+q_z^2=4k^2$. We performed RSM so that the region in q-space where Braggs diffraction condition is investigated is completely mapped. Different procedures are possible for obtaining RSM. We performed number of 2θ scans for a range of ω values around Braggs diffraction region. RSM is also possible with 2θ scans for a range of ψ values (fig. 4.2). In both cases, combining all the scans an intensity plot in the q-space is obtained for q_x and q_z. We followed the first method for easier access to plotting RSM data.

Information about strain and domain structure in thin films can be obtained from RSM of lattice planes. In fig. 4.8 and fig. 4.7, q_x and q_z represents the horizontal and vertical projections (in nm^{-1}) respectively of RSM plane direction. In fig. 4.7, RSM of the (130) plane in a (110) CrO_2 film on (110) TiO_2 substrate did not show any substrate-induced strain while RSM of (031) and (130) planes in (100) CrO_2 films show that the film is strained when compared with RSM of the same plane of the (100) TiO_2 substrate as, the CrO_2 and TiO_2 2θ intensities are in different regions in a 2θ scan (fig. 4.8). These RSM images also confirm the relaxed growth of (110) films and strained growth of (100) films on respective TiO_2 substrates. The RSMs also indicate single domain evolution of the films as only single significant intensity region in the films could be observed within the scan range.

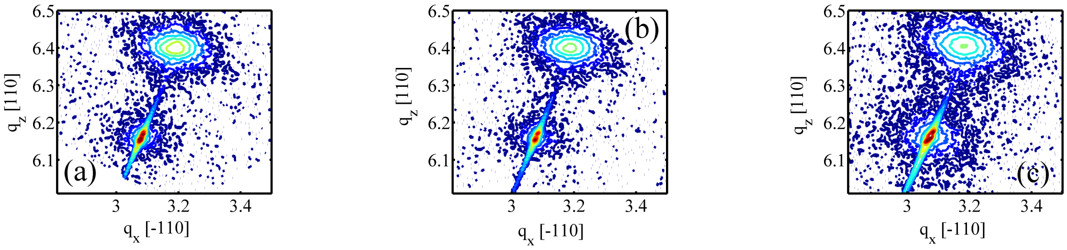

Figure 4.7: RSM of (130) plane in 100 nm (a), 45 nm (b) and 25 nm (c) (110) CrO_2 films. CrO_2 is above the TiO_2 intensity region.

4.6 Strain and lattice constants in (100) and (110) CrO_2 films

Lattice constants in epitaxial (100) and (110) CrO_2 films were determined using Cohen′s method as mentioned in section 4.4. Using the values from table 4.1 in eq. 4.4 , the lattice constants and resulting strain in all lattice directions (namely a,b and c) were calculated. Lattice constants and unit cell volumes as a function of film thickness are plotted in fig. 4.9.

Compressive strain was observed along the out-of-plane, b direction in (100) CrO_2 films and the thinnest sample (25 nm) has the highest compressive strain of -1.15% (b=4.368 Å). We found that the compressive strain decreased with increasing (100) CrO_2

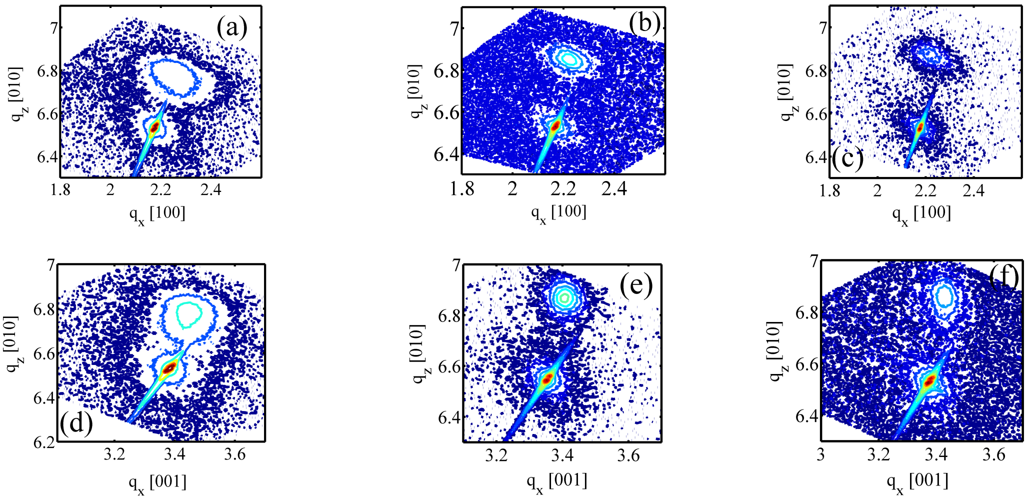

Figure 4.8: RSM of (130) and (031) planes in (100) CrO_2 films of 100 nm (a & d), 45 nm (b & e) and 25 nm (c & f) respectively. CrO_2 is above the TiO_2 intensity region. Contrast is not same each image because of different SNR.

film thickness about -0.9% in 45nm (b=4.382 Å) and -0.6% in 100 nm film (b=4.396 Å). Tensile strain was observed along the c and a directions in the (100) CrO_2 films, with its magnitude decreasing with increasing (100) film thickness. In 25 nm (100) films, strain along the a direction was 1.8% (a=4.500 Å) and it decreased to 1.56% (a=4.492 Å) and 1.42% (a=4.484 Å) in 45 nm and 100 nm films, respectively. Strain in the c direction was found to be smaller than the strain along a and b directions in the (100) CrO_2 films. In the c direction, 25 nm (100) film had strain of 0.6% (c=2.934 Å) while 45 nm and 100 nm (100) films had strain of 0.54% (c=2.932 Å) and 0.15% (c=2.920 Å), respectively. This indicates that overall the (100) CrO_2 unit cell is more distorted along the in-plane direction a. Therefore, as a result of substrate induced strain, the unit cell in a (100) CrO_2 film is compressed in the b direction and consequently expands in the c and a directions leading to an overall tetragonal distortion. Considering a tetragonal unit cell for this strained (100) CrO_2 film, the calculated unit cell volume was found to be slightly larger than the bulk CrO_2 unit cell volume, decreasing towards the bulk value with increasing film thickness. Overall, the thinnest (100) CrO_2 sample (25 nm) is most significantly strained in all three directions and lattice parameters and unit cell volume converges towards bulk values as thickness increases, but still significantly larger even for

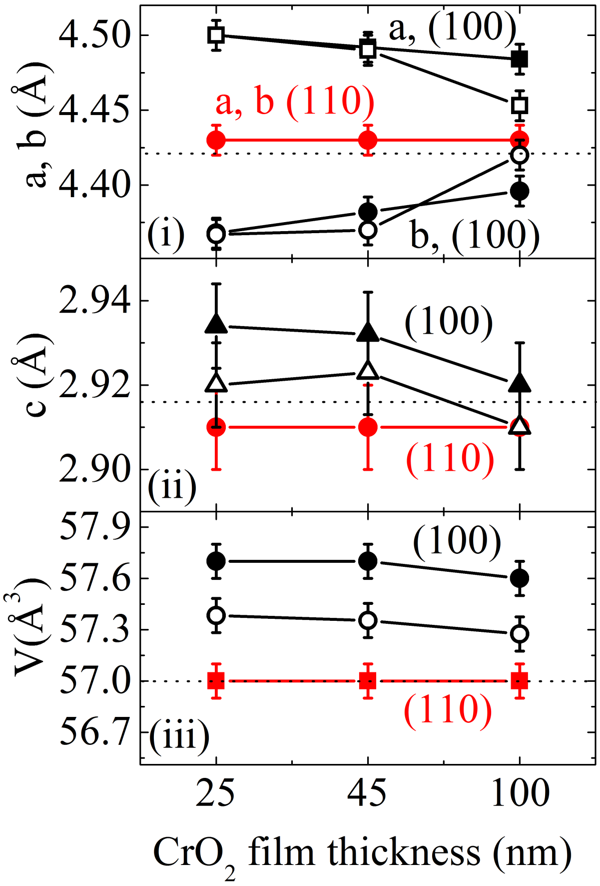

Figure 4.9: (i) Lattice constants a and b of (100) and (110) CrO_2 films for different thicknesses. (ii) Lattice constant c against thickness. (iii) Unit cell volume against thickness. Open symbols indicate the respective values calculated from RSM of (100) CrO_2 films. Errors in determining lattice constants and unit cell volumes are estimated at 2-3% of the reported values. The dotted lines in (i), (ii) and (iii) show the respective values of the parameters in bulk CrO_2.

100 nm films. On the other hand, lattice constants in (110) CrO_2 films for all thicknesses were found to be within ±0.01 Å of bulk CrO_2 lattice parameters in all three directions and as a result, the (110) CrO_2 unit cell maintained essentially its bulk unit cell volume for all thicknesses. Calculated TiO_2 substrate lattice parameters were within ±0.002 Å of bulk TiO_2, demonstrating high quality of the substrates used for film deposition.

Lattice constants in (100) CrO_2 films were also determined from RSM. In fig. 4.8, RSM of (031) and (130) planes in (100) CrO_2 film confirms that the film is strained when compared with RSM of the same plane of the (100) TiO_2 substrate, as the CrO_2 intensity region is displaced from the TiO_2 2θ direction. However, in fig. 4.7, RSM of the (130) plane in a (110) CrO_2 film on (110) TiO_2 substrate did not show any substrate-induced strain. Lattice constants in (100) CrO_2 films were evaluated from the projections of the center of film intensity on the axes. From the projections of (031) plane we have $c=1/q_x$ and $b=3/q_z$, and in case of the (130) plane we have $a=1/q_x$ and $b=3/q_z$. As no projection on c was available in our sample geometry (within the range of angles available) for (110) CrO_2 film, we were not able to determine the lattice constants in (110) CrO_2 films from RSM. Lattice constants in (100) CrO_2 films determined using RSM are plotted in fig. 4.9 along with lattice constants determined using Cohen′s method. As seen in fig. 4.9, lattice constants determined by both RSM and Cohen′s method for (100) CrO_2 films are in good agreement, showing a similar trend with thickness, i.e. approaching bulk lattice parameters with increasing film thickness as the substrate induced strain decreases.

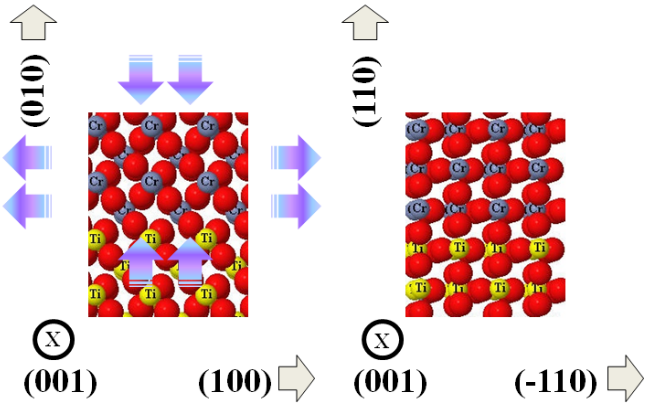

(a) (b)

Figure 4.10: Rutile structure of (100)- and (110)-oriented CrO_2 films are shown in (a) and (b) respectively on TiO_2 substrates of respective orientations. Red spheres indicate the O^{2-} ions on both structures. Out of plane directions on (100) and (110) films are (010) and (110) respectively as shown in the figure. In the (100) structures, compressive strain along out of plane direction and tensile strain along in plane directions are schematically shown while the (110) structure remains strain free.

4.7 Effect of strain on the magnetic moment in CrO_2 thin films

The strained unit cell in (100) CrO_2 can be expected to strongly affect the magnetic properties since the exchange and the magnetic moment are very sensitive to the lattice parameters. On the other hand, since (110) CrO_2 films are found to essentially maintain the bulk lattice parameters; little impact on their magnetic properties is expected.

Fig. 4.11 shows the saturation magnetic moment of the (100) and (110) CrO_2 films measured in SQUID magnetometer. For all thicknesses studied, (110) films showed higher magnetic moment than (100) films at room temperature (∼300 K), attributed to the strain-free growth of the (110) CrO_2 films on TiO_2 substrates. Assuming Cr has a spin magnetic moment of 2.0μB at low temperatures (∼10 K) and neglecting any spin or orbital moment arising from the O^{2-} ions, magnetic moments per Cr atom at 300 K are calculated and reported in table 4.2. We found the Cr moment in (100) CrO_2 films to decrease with decreasing film thickness while (110) films showed no strong trend. We attribute the decreased moment in (100) films to increase in substrate-induced strain in the (100) CrO_2 films with decreasing film thickness.

Table 4.2: CrO_2 moment in the films at 300 K calculated from the SQUID data. Moment values have an uncertainty of $\pm 0.05\mu_B$.

CrO_2 moment (μ_B)	25 nm	45 nm	100 nm
(100)	1.11	1.23	1.43
(110)	1.41	1.51	1.54

4.8 Transport properties of (100) and (110) CrO_2 thin films

With such a strong alteration of magnetic moment with strain, we investigated possible changes in conductance mechanisms of strained (100) and strain free (110) CrO_2 films. In this case, we deposited CrO_2 films of both orientations using selective growth

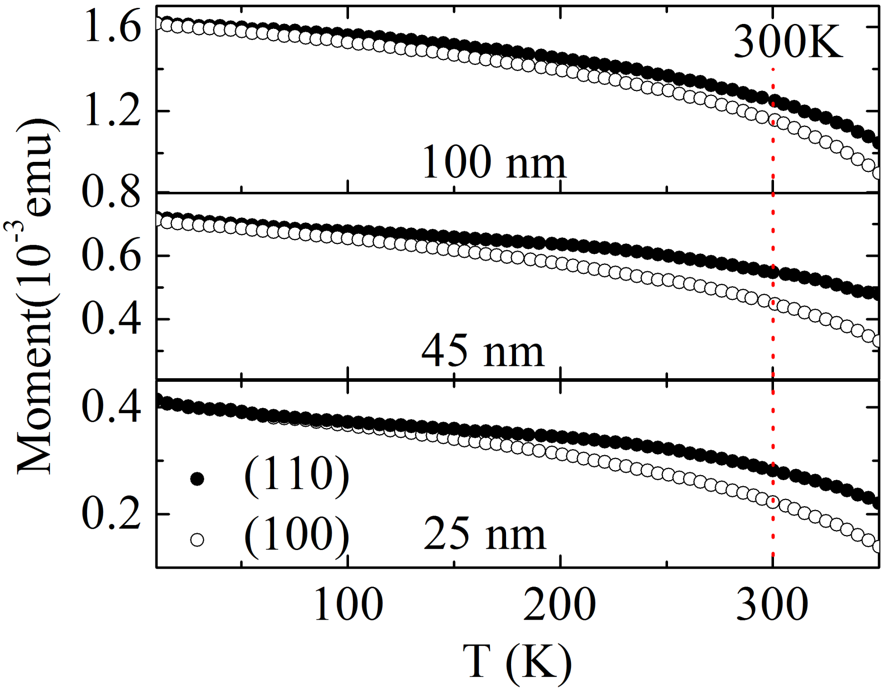

Figure 4.11: Magnetic moments of (100) and (110) CrO_2 films from 10-350 K measured for three different thicknesses in SQUID. Dashed line is through the moments at 300 K. A magnetic field of 5 kOe was applied along the easy axis direction of the samples at all temperatures to saturate the magnetization.

method [34] to define Hall bars of $100\times400\mu m^2$ patterned on TiO_2 substrates of respective orientations (a Hall bar is shown in fig. 4.12 below).

Both these films had thickness of 70 nm. At that thickness, the (100) CrO_2 film is still significantly strained (they were found to be strained even for thicknesses of more than 200 nm) [41]. Resistivity in our films from 5-400 K are plotted in fig. 4.13 (a) measured with 100 μA current along (001) direction for both films. At all temperatures, resistivities of both films were found to be similar suggesting the same conductance mechanism in both films and in good agreement with previous reported results on CrO_2 films [47, 48, 49]. Below ∼35 K, the resistivity approaches a constant value (inset in fig. 4.13(b)), and the residual resistivity (ρ_0) of the films and are about 7 $\mu\Omega$cm and 3 $\mu\Omega$cm in (100) and (110) films respectively. Lower ρ_0 in (110) films may indicate that the film has less defects than the (100) films, e.g. longer coherence length. We also found higher

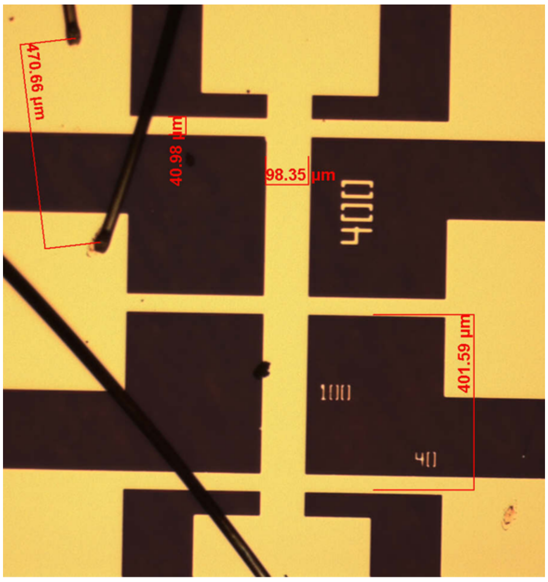

Figure 4.12: Optical image of a selectively grown CrO_2 with Hall bar pattern. Bright yellow regions are CrO_2 as seen under optical microscope.

residual resistivity ratio (RRR), defined as $\rho(300\text{K})/\rho_0$ in case of (110) films (RRR ~98) than (100) films (RRR ~45) as can be observed in fig. 4.13(b), indicating that (110) films do exhibit more metallic conductance, perhaps consistent with phonon frequencies being altered by substrate induced strain in (100) CrO_2 films. As no significant temperature dependence of resistivity in the films were observed below ~35 K (and hence no T^2 dependence), we can say that there is no significant spin-flip scattering in the films below 35 K. This is consistent with, though not unambiguous proof of half-metallic behavior, as found [50]. Resistivity alone does not preclude both films being half-metallic below this temperature. With increasing temperature (~100 K), the minority spin channel is expected to contribute to the conductance giving temperature dependence of resistivity as expected for a non-half-metallic ferromagnetic material. The insets in fig. 4.13(a) show the small but noticeable changes in slopes in the resistivity plots between 390-395 K in both (100) and (110) films. This suggests that the ferromagnetic state is lost in both films between these temperatures [51]. It is known that in a ferromagnetic metal, the contribution to resistivity above T_c due to spin disorder is constant, while contribution due to phonon scattering increases as temperature increases [51], and as a result, the slope changes near T$_c$.

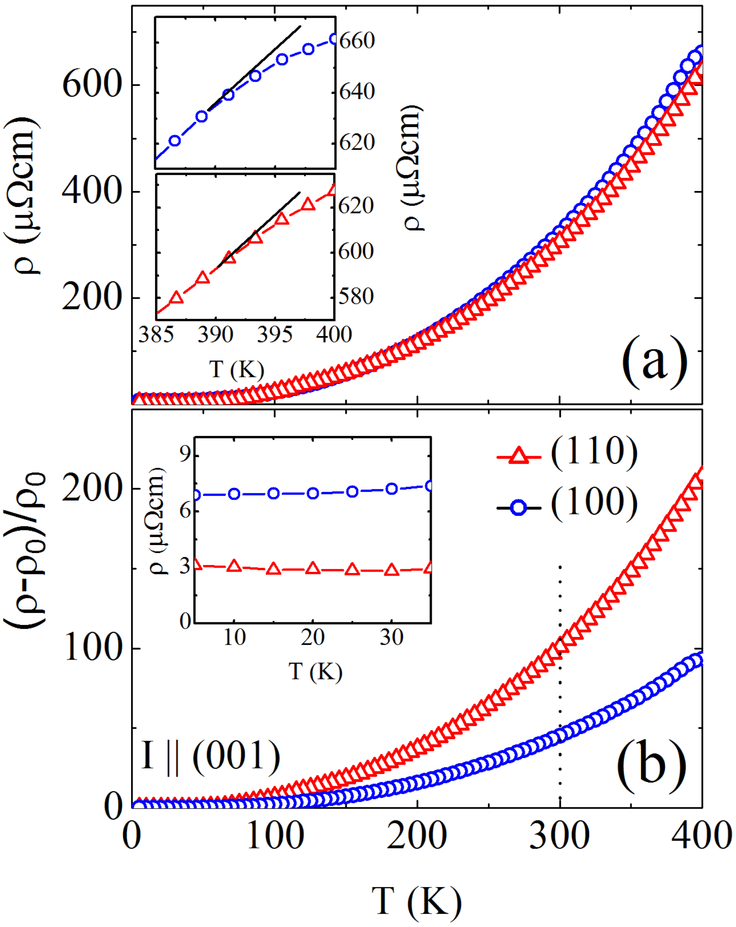

Figure 4.13: (a) Resistivity plot of (100) and (110) CrO$_2$ films of thickness 70 nm from 5-400 K. Inset shows the resistivity in the films from 385-400 K. Black lines are drawn to look the slope change more noticeable. (b) $(\rho - \rho_0)/\rho_0$ vs. temperature clearly shows the higher RRR for (110) film The dotted line indicates the room temperature. The inset shows a constant resistivity from 5-35 K.

4.9 Strain and surface morphology in CrO$_2$ thin films

AFM on epitaxial (100) and (110) CrO$_2$ films grown on isostructural TiO$_2$ substrates showed different surface morphology due to their different growth modes. (100) films follow layer by layer growth while (110) films exhibit island growth. Although the reason for strain in the films has been narrowed down to different growth modes of (100) and

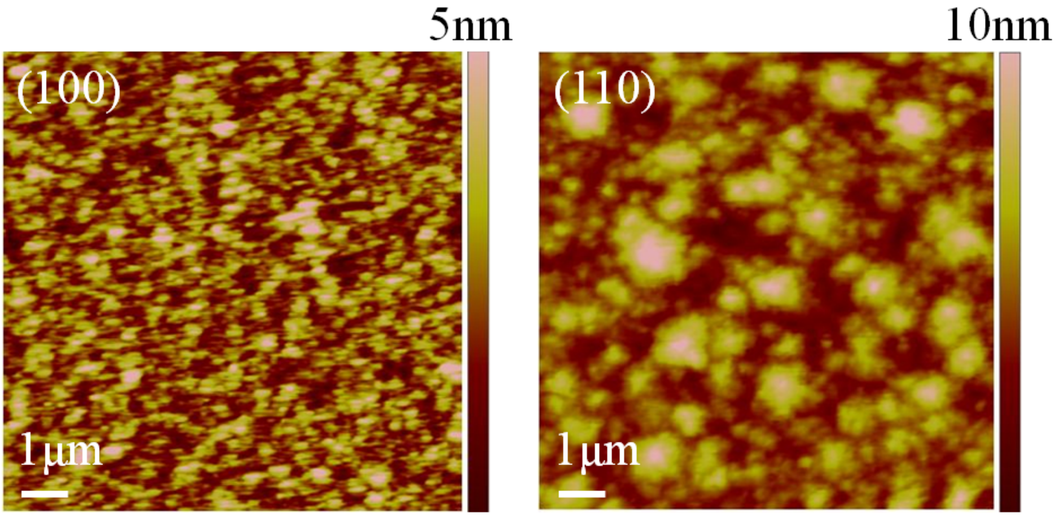

Figure 4.14: AFM on (100)- and (110)- CrO_2 films of thickness 45 nm showing their different surface morphologies.

(110) CrO_2 films, the origin of different growth modes is not very clear yet. It can be speculated that the origin of different growth modes lies in the surface energy difference between the substrate and the film of respective orientations. For a particular orientation, if the substrate surface has higher surface energy, σ_{sub} (or, surface tension) than combined film surface energy, σ_{film} and their interface energy, γ (illustrated in fig. 4.15); the film exhibits layer by layer growth [41]. On the other hand, for substrate surface energy being smaller than combined film surface energy and their interface energy; the film exhibits island growth. As observed in our case, (100) films are strained i.e. not relaxed because of layer by layer growth where as (110) films are strain free i.e. relaxed because of island growth. Thin film growth is also very sensitive to interface conditions that is not very straightforward to investigate or model theoretically. Ways for monitoring growth of CrO_2 films are limited as the films are grown under atmospheric conditions. Surface and interface energies in CrO_2/TiO_2 structures for (100) and (110) orientations are being theoretically investigated by my colleagues Hunter Sims and Krishna B. Chetry.

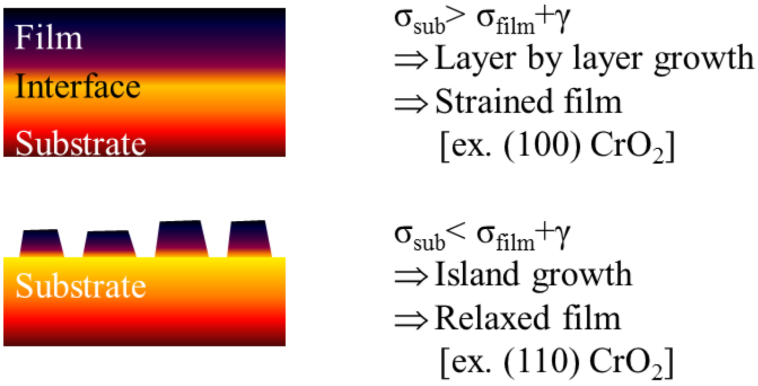

Figure 4.15: A cartoon for layer-by-layer and island growth of thin films.

4.10 Conclusions

In summary, (100) CrO_2 films were found to be strained while (110) CrO_2 films were found to be relaxed. The lattice constants and the degree of substrate-induced strain along the principal lattice directions were determined in (100) CrO_2 films grown on (100) TiO_2 substrate. Out of plane directions are compressively strained while in-plane directions are in tensile strain in (100) CrO_2 films. Strain along the a direction i.e. (100) was found to be more significant than strain along b and c directions, i.e. (010) and (001) directions. (110) CrO_2 films were found to be strain-free in all lattice directions - attributed to relaxed growth of (110) CrO_2 films on (110) TiO_2 substrates. We also observed that substrate-induced strain significantly reduces the magnetic moment in (100) CrO_2 films at room temperature. In spite of the substrate-induced strain in (100) CrO_2 films, similar transport behavior was observed in both (100) and (110) CrO_2 films both at low temperatures as well as near T_c.

Chapter 5

XMCD EXPERIMENTS ON CrO_2 AND CrO_2/RuO_2 BILAYER FILMS

5.1 Introduction

The absorption of circularly polarized light by an optically active material can be slightly different for left and right circular polarization of incident light. Similarly, absorption of X-rays by a magnetic material can be slightly different for right and left circular polarization of incident X-rays - giving rise to the phenomenon called X-ray magnetic circular dichroism (XMCD). Basically, XMCD is a spectroscopic magnetic characterization technique pioneered by Schütz et al [52]. The main advantage of XMCD over other magnetic characterization techniques is the element specific separation of spin and angular magnetic moments and their anisotropies in a material. Because of that, XMCD has been a popular magnetic characterization technique in recent years. Since soft X-rays are used ($\leq$1 k eV), only the surface/interface region (1 - 10 nm) is probed in XMCD. As high intensity and polarized X-ray beams are required for XMCD, it is usually performed at various synchrotron facilities around the world. We employed XMCD technique on (100) and (110) CrO_2 films as well as on (100) CrO_2/RuO_2 bilayer films for a qualitative and quantitative understanding of Cr spins and angular moments in these films. All XMCD spectra reported in this dissertation were obtained at the *port 123, 10-m TGM* (toroidal grating monochromator) and *Hermon* beam lines located at the national facility of Synchrotron Radiation Center (SRC), University of Wisconsin, Madison, USA. In this chapter, the theory of XMCD is briefly described. Then the moment analysis technique, "sum rules", is presented, followed by the XMCD results on epitaxial (100) and (110) CrO_2 films and (100) CrO_2/RuO_2 bilayer films and conclusions from the XMCD experiment.

5.2 Theory of XMCD

XMCD occurs due to the difference in scattering cross-section when polarized light (polarization vector **P**) interacts with spin up and spin down electrons (spin +1/2 and -1/2 respectively) in a material. The phenomenon of XMCD can qualitatively be understood by the one electron picture as described by J. Stöhr. First, a 2p electron is excited to the empty 3d states by incident polarized X-rays [53]. These 3d states, the unoccupied electronic states, are considered as the holes. In case of 3d elements such as Fe, Co and Ni number of holes can directly be obtained from the electronic configuration. However; accurate numbers of holes for compounds or alloys are obtained from detailed electronic structure calculations.

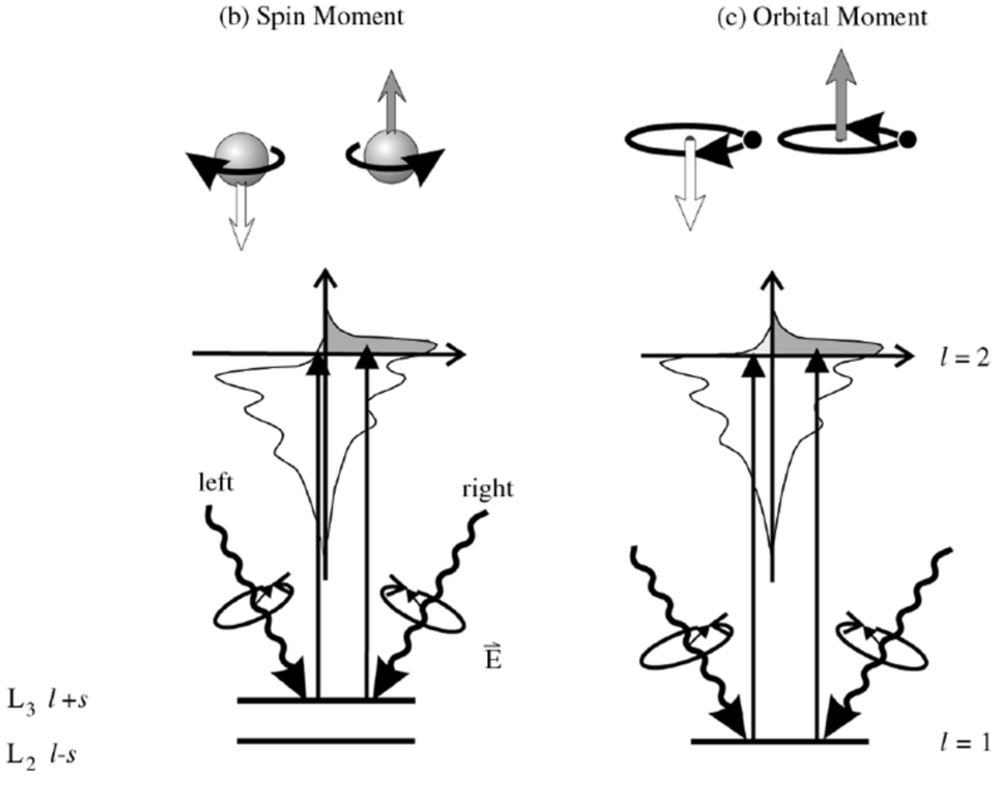

Figure 5.1: Transfer of spin and angular moments in the L-edge absorption of X-rays for two different helicities (This figure is taken from reference [53]).

Because of spin-orbit coupling, the 2p level is split as **l+s** and **l-s** or L_3 and L_2 levels respectively (L_3 and L_2 levels are also denoted by $p_{3/2}$ and $p_{1/2}$ respectively). When incident X-rays are absorbed by the 2p electrons, 2p→3d and other transitions are possible following selection rule: $\Delta l=0, \pm1$ however, the 2p→3d transition dominates [54], and absorption intensities are proportional to the number of available 3d states (i.e. number of 3d holes). As shown in fig. 5.2, when we consider the transition from $L_3 \rightarrow$ 3d, the angular momentum of the left circularly polarized incident photon (i.e. $-\hbar$) is transferred to the excited L_3 electron. Due to spin-orbit coupling, this angular momentum is transferred to both spin and angular moments of this electron. Accordingly, left circularly polarized X-rays transfer this L_3 electron to the available minority states in 3d, a right circularly polarized photon with angular momentum $\hbar$ transfers the electron from L_3 to the majority states in 3d. The spin-orbit coupling is opposite for the L_2 edge compared to the L_3 edge, and therefore the transition is opposite at (and near) the L_2 edge. At the L_2 edge, left circularly polarized X-rays transfer the electron to the available majority states while the right circularly polarized X-rays transfer the electron to the available minority states. In total electron yield (TEY) method for XMCD, all the electrons taking part in these transitions are collected by a high voltage to a collector (400 V in our case) while the photon energy is scanned using a monochromator. If majority and minority states are not balanced, as in ferromagnetic materials, we observe a difference in absorption intensities for left and right circularly polarized X-rays and this difference gives rise to the dichroism effect. Although we have considered the polarization of X-rays to be switching from left to right and vice versa while keeping the magnetization direction fixed, it is equivalent to switch the magnetization direction with fixed photon polarization [55]. Since it is much easier to switch the magnetization direction by applying an external field than to switch the polarization of the X-rays, we kept the polarization fixed in our XMCD experiment and switched the magnetization direction at each energy.

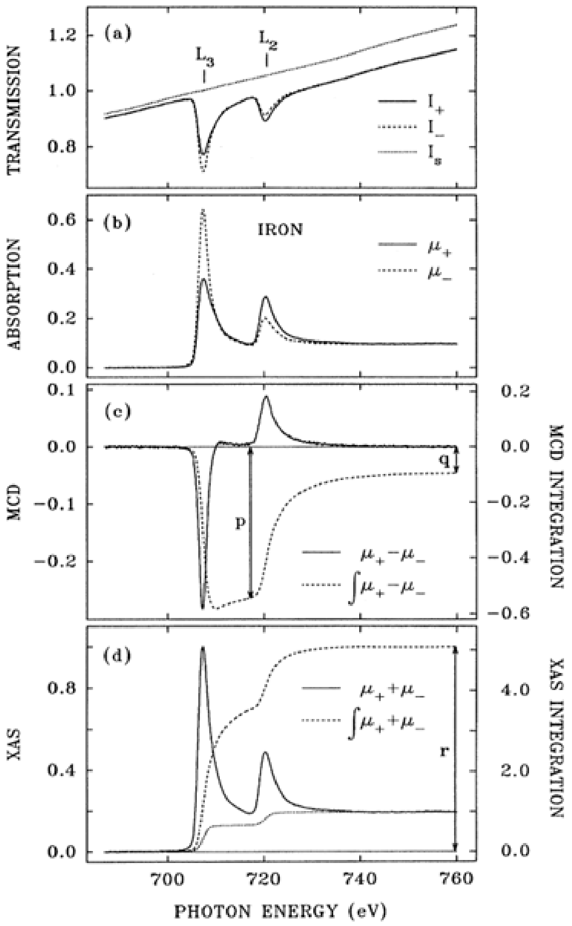

Figure 5.2: This image is taken from reference [58] for illustration of applying sum rules.(a) Transmission current for two different polarizations along with the magnetization independent current (I_s) (b) X-ray absorption (XAS) at the $L_{2,3}$ edges of Fe. μ_+ is the signal with one polarization while μ_- is the signal with the other polarization. (c) The XMCD signal (μ_+-μ_-) along with its integral. (d) Summation of the absorption intensities (μ_++μ_-) and its integral.

5.3 Sum rules and XMCD moment analysis

The sum rules relate the observed absorption intensities to the spin and angular moments in the sample. Basically these rules make it possible to decompose the element specific spin and angular magnetic moment in a system where several magnetic and nonmagnetic elements are present, irrespective of their concentrations. As stated by Thole et al. [56] and Carra et al. [57], estimation of spin (m$_s$), angular (m$_l$) and the quadrupolar magnetic moments (T$_z$) are possible. When expectation values of the operators S$_z$ and L$_z$ are obtained over core level absorptions both at L$_3$ and L$_2$ edges, the difference between the integrated absorption intensities for right and left circular polarization of incident X-rays gives us the spin and the angular moments. As the spin-orbit interaction (∼50 meV) is much smaller than exchange interaction (∼1 eV) for the matter under study, observed angular moments are much smaller than spin moments (for example in Co, m$_s$=1.64 μ_B while m$_l$= 0.14 μ_B) [53]. The quadrupolar term, T$_z$ arises mainly because of the structural asymmetry of the system such as in CrO$_2$ where the tetragonal rutile unit cell has a=b c.

Chen et al. have successfully showed that moment analysis on XMCD spectra of Co and Fe gives spin and angular moments that are correct within few percent of those obtained experimentally from Einstein-de Haas gyromagnetic ratio measurements and those obtained from theory [58]. Application of the sum rules is illustrated in fig. 5.2. After background correction, normalization, and the correction for projection of polarization on the magnetization direction of the sample, the XAS and XMCD data at the L$_2$ and L$_3$ edges are used to find spin and angular moments. The sum rules to determine the spin and angular moments are:

$$\begin{aligned} m_{spin} = -&\frac{6\int\limits_{L_3}(\mu_+ - \mu_-)\,dE - 4\int\limits_{L_3+L_2}(\mu_+ + \mu_-)\,dE}{\int\limits_{L_3+L_2}(\mu_+ + \mu_-)\,dE} \\ &\times(10 - n_{3d})\left(1 + \frac{<7T_z>}{2<S_z>}\right)^{-1} \end{aligned} \tag{5.1}$$

$$m_{orb} = -\frac{4}{3}\frac{\int\limits_{L_3+L_2}(\mu_+ - \mu_-)\,dE}{\int\limits_{L_3+L_2}(\mu_+ + \mu_-)\,dE} \times (10 - n_{3d}) \tag{5.2}$$

In terms of p, q and r representing the integrals shown in fig. 5.2, the sum rules can be written in a simplified form as follows:

$$m_{spin} + 7T_z = -(10 - n_{3d})\frac{6p - 4q}{r} \tag{5.3}$$

$$m_{orb} = -(10 - n_{3d})\frac{4q}{3r} \tag{5.4}$$

Here n_{3d} is the number of holes in 3d states.

Therefore, following the above procedure for analyzing XMCD data, moment analysis procedure for CrO_2 (and other) films can be stated as follows: 1. XAS data with both polarizations are corrected with Shriley background subtraction [59, 60] and then normalized. The Shirley algorithm is an iterative method for background determination commonly used for background subtraction in XPS data [61]. Fig. 5.3 shows the Shirley background of an XAS data on CrO_2. The Shirley background intensity is computed as:

$$S(E) = I_2 + \kappa\frac{A2(E)}{A1(E) + A2(E)} \tag{5.5}$$

Here, κ is defined as (I_2-I_1) and it is basically the step background. As shown in fig. 5.3, S(E) is initially estimated from the XAS data along with the integrated areas A1(E) and A2(E) under the two peaks. The trial background is then iterated and refined using the above relation in 5.3.

2. Now the background corrected XAS data(μ_+ and μ_-) are normalized and separately averaged from several scans.

3. Integrals p, q and r are determined as discussed above from the XMCD ($\mu_+ - \mu_-$) and summation of the absorption intensities ($\mu_+ + \mu_-$).

4. Relations 5.3 and 5.3 are used for moment estimation.

5. To account for the polarization (**P**) and its projection on the magnetization direction,

obtained values are multiplied by $1/(|\mathbf{P}|\cos\theta)$. For our experiment, $|\mathbf{P}|\sim 85\%$ and θ, the angle between polarization and magnetization direction was fixed at 45°.

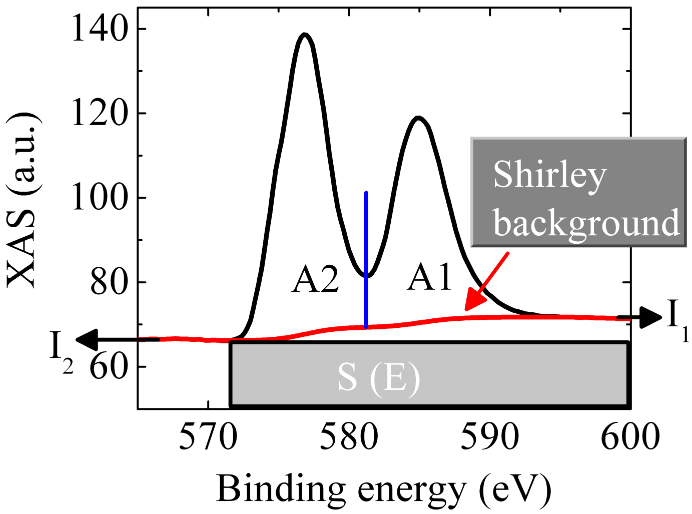

Figure 5.3: Shirley background for an XAS data at the Cr $L_{2,3}$ edges in CrO_2.

5.4 Experimental set up

A brief description of the experimental set up is provided here without the details of the beam line used in SRC. As shown in figure 5.4(b), maximum magnetic field of 1400 Oe were applied to saturate the magnetization along the easy axis direction (c axis direction in case of CrO_2 films) of our films. At each energy, the magnetization direction was switched and absorption spectra were taken at a small remnant field (~70 Oe). The remnant field was kept sufficiently low so that background was not significantly affected by the applied high voltage. A high voltage of 400 V was applied to collect all the electrons coming out of the sample (total electron yield method). A base pressure of less than 3×10^{-9} Torr during collection of spectra provided good signal to noise ratio (SNR).

5.5 Absorption at the $L_{2,3}$ edges of Cr

The XMCD technique was employed to estimate the magnetic moments of Cr at the surface in (100) and (110) CrO_2 films. We prepared films of each orientation with

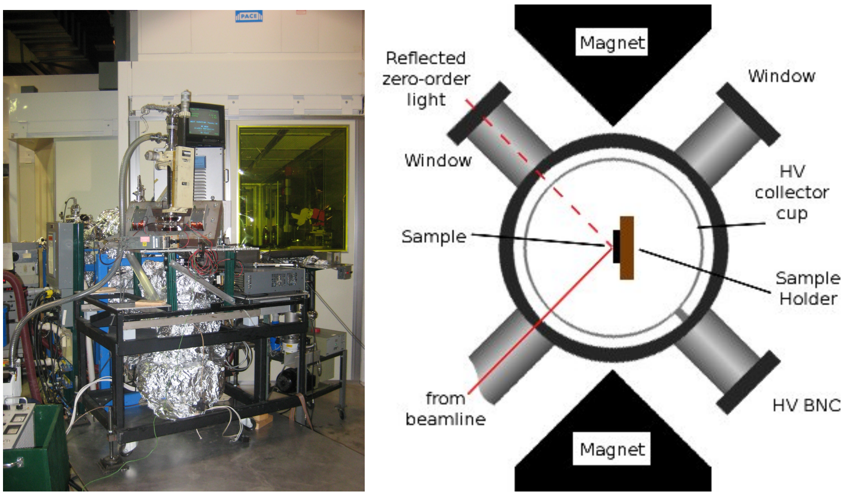

(a) (b)

Figure 5.4: (a) A picture of the XMCD chamber at SRC. (b) Schematic diagram of the XMCD chamber and sample geometry.

thickness 45 nm using CVD, and films of both orientations had same thickness as determined from XRR. (100) CrO_2 films for this thickness range were found to be heavily strained while (110) CrO_2 films are not as showed in the last chapter. Fig. 5.5 shows the normalized XAS spectra of (110) and (100) CrO_2 films on Cr $L_2, 3$ edges at room temperature after saturating the films in opposite directions with fixed photon helicity (indicated by μ_+ and μ_-). We also obtained XAS spectra on the O-K edge, scanning the beam energy from 550-515 eV. However, no unambiguous XMCD was observed from the O-K edge at room temperature. Therefore, in our analysis we have neglected any spin and orbital contribution coming from the O^{2-} ions in CrO_2.

In Figure 5.6(a), the XMCD spectra are plotted which were obtained by subtracting the two XAS spectra obtained at opposite sample magnetizations. The (110) oriented films show a larger XMCD signal than (100) films. The XMCD line shapes are nearly identical, and agree well with previous results obtained on (100) oriented films near room temperature [62]. Quantitative analysis using the sum-rules for 3d elements is somewhat complicated for transition metal oxides in general and for CrO_2 in particular [63]. Two main issues are relevant in the case of CrO_2. The first arises from the weak spin-orbit splitting of the Cr 2p levels and the second from the distorted oxygen octahedra around

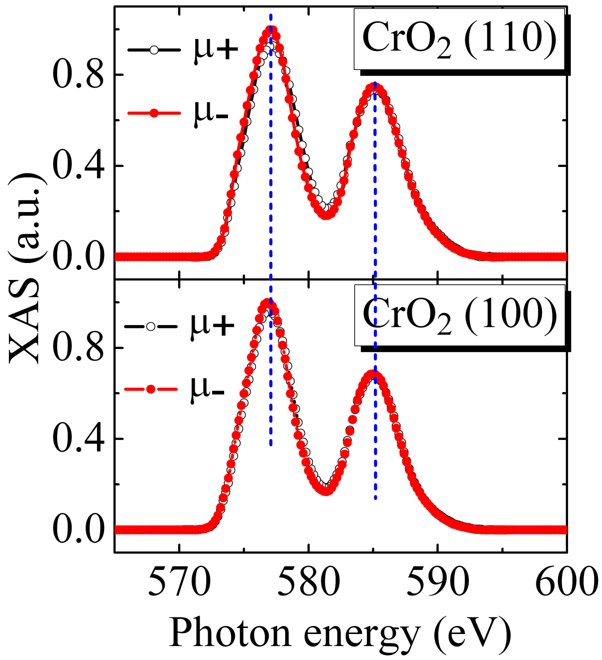

Figure 5.5: Photon energy scan on Cr $L_2, 3$ edges (600-565 eV), showing strong polarization dependent x-ray absorption. We observed Cr L_2 and L_3 peaks at 585 eV and 577 eV respectively within the resolution of the instrument (±0.25 eV) for both (100) and (110) oriented films. X-ray absorption (XAS) data are normalized for comparison between the spectra of (100) and (110) oriented films.

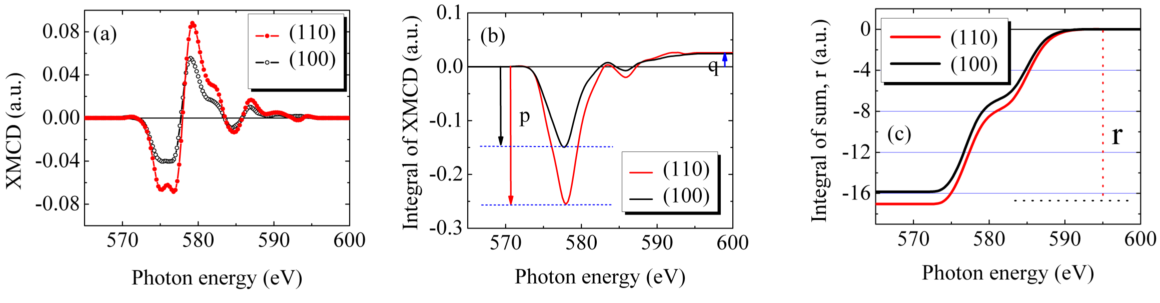

(a) XMCD (b) Integral of $(\mu_+ - \mu_-)$ (c) Integral of $(\mu_+ + \mu_-)$

Figure 5.6: XMCD $(\mu_+ - \mu_-)$ is shown in (a) obtained from the XAS on (100)- and (110)- CrO$_2$ films and (b) shows the integral of XMCD. Integrals p and q for (100) and (110) CrO$_2$ films are shown. (c) Integral r for both films was between 16 and 17 - not significantly different and much larger than p and q.

the central Cr^{4+} ion.

Weak spin-orbit coupling leads to substantial spectral overlap, meaning that the $2p_{3/2} \rightarrow 3d$ (L_3) and $2p_{1/2} \rightarrow 3d$ (L_2) transitions lie very close in energy. This overlap has been estimated to give 5-15% error in the sum rules [64]. Additionally, and more importantly, the x-ray absorption is not from pure $p_{3/2}$ or $p_{1/2}$ states but rather from a quantum-mechanical superposition of both. This is commonly referred to as *jj*-mixing. To take into account this mixture, correction factors have been evaluated for some systems and estimated to be approximately 2.0 for bulk Cr and we use this value in our estimates [64]. Complications from the distorted CrO_2 octahedra result in a substantial contribution to both the dipole moment term and the quadrupole moment term, represented by T_z in the spin sum rule. The e_g ($d_{x^2-y^2}$ and $d_{3z^2-r^2}$) and t_{2g} (d_{xy}, d_{xz} and d_{yz}) manifolds do not possess isotropic charge density in CrO_2 and this gives rise to the quadrupole moment term, T_z [53]. This T_z term for CrO_2 has been reported to be much larger than that for 3d metals like Fe, Co and anisotropic [65]. In our calculations, for a lack of proper understanding and available data, we do not correct for the T_z value and further assume the T_z value to be the same for (100) and (110) orientations as the c/a ratio values are found to be 0.669 for strained (100) structure and 0.659 for the strain free (110) structure suggesting a small tetragonal distortion due to strain in (100) structure. The orbital moment, on the other hand, does not depend on the T_z term explicitly and can be estimated directly using the sum rules.

Knowing these limitations, we analyzed our data using the XMCD sum rules for 3d elements mentioned in relations 5.3 and 5.3. Number of holes in Cr^{4+}, n_{3d} was taken as 8.0 [65]. Figure 5.6(b) shows the integrals p and q and figure 5.6(c) shows the integral r vs. photon energy. The orbital moment was found to be virtually identical for both (100) and (110) orientation, approximately (-0.030±0.005) μ_B. This value agrees reasonably well with LDA+U calculations of Komelj et al. [63] (-0.037 μ_B) but is slightly lower than experimental reports of Georing et al. (-0.062 μ_B) and Huang et al. (-0.051 μ_B) [65, 66]. The spin moments (m_s+7T_z) were found to be (1.2±0.2) μ_B and (1.8±0.3) μ_B

for (100) and (110) orientations respectively. Therefore the spin moment in (110) films was nearly 50% higher than the one in (100) orientation at room temperature. Since these measurements are at room temperature, we expect the moment values to be less than 2.0 μ_B per Cr, the experimental and theoretical bulk moment at low temperature.

5.6 Comparison of surface and bulk magnetic moments

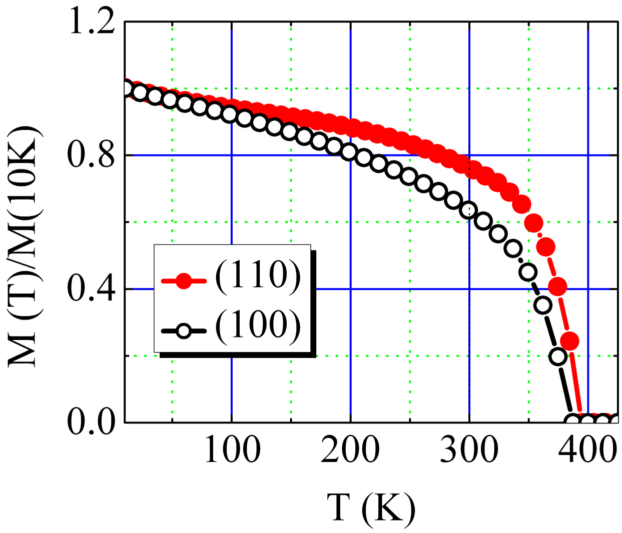

Figure 5.7: Normalized magnetic moments of (100) and (110) CrO_2 films plotted vs. temperature in steps of 10 K. Data from 10 K to 350 K were taken in SQUID and from 300 K to 425 K were taken using a VSM. No offset in moment was found between SQUID and VSM data. Moment values have an estimated uncertainty of 2% at all temperatures, and the temperature was stable within 0.2 K. The T_c for (100) and (110) CrO_2 films are found to be 385 K and 393 K, respectively. Considering the fluctuations near T_c, the uncertainty in T_c can be estimated to be ±5 K.

The bulk magnetic moment measurements against temperature from 10-425 K on the same (100) and (110) CrO_2 films using SQUID and VSM is shown in fig. 5.7. Magnetization for both films at 10 K is found to be $\sim 6.5\times10^5$ A/m which is in agreement with previous reported magnetization values at low temperature [36]. The magnetic moment decays faster in case of (100) CrO_2 films which are about 25% lower than (110)

CrO_2 films at room temperature. Although SQUID and VSM measure the total magnetic moment of the film while XMCD gives surface magnetic moment; given the 10-15% error in moment estimation with XMCD, the difference in moment between (100) and (110) CrO_2 films at room temperature obtained by SQUID is in good agreement with the difference calculated from XMCD analysis. It is believed to be an intrinsic property of the high quality CrO_2 thin films, and a direct manifestation of the different effects of strain in the two orientations. As supporting evidence, fig. 5.7, the Curie temperature, (T_c) for (100) CrO_2 was found to be slightly lower than that of (110) CrO_2. It is known that T_c can be suppressed due to strain [67] in a film.

5.7 Absorption at the Ru $M_{2,3}$ and Cr $L_{2,3}$ edges in CrO_2/RuO_2 bilayers

As reported by G. X. Miao et al., low GMR in (100) $CrO_2/RuO_2/CrO_2$ is attributed to the intermixing at the interfaces [68]. This intermixing might possibly induce magnetic moment in Ru at the interface. Because of its sensitivity and element specificity, we employed XMCD technique to investigate the induced moment in Ru. For this experiment, CrO_2/RuO_2 bilayer films of (100) orientation were prepared with RuO_2 on top. CrO_2 films thickness was 30 nm while RuO_2 film thicknesses were 1.5 nm, 2.0 nm and 2.5 nm. As discussed in chapter 3, (100) CrO_2 film of thickness 30 nm are highly strained.

Absorption intensities are sufficient at $M_{2,3}$ edges (3p→4d) in Ru (440 500 eV) to observe XMCD and estimate magnetic moment [69]. $M_{2,3}$ edges were also accessible in the beam lines used in SRC (photon energies 250-1000 eV) while $L_{2,3}$ edges were not accessible (2800-3000 eV). Therefore, Ru $M_{2,3}$ edges were investigated for XMCD signal on the bilayer samples in the same experimental set up mentioned in section 5.4. Absorption intensities at room temperature are shown in fig. 5.8. However, within the resolution of our instrument and at room temperature, clear difference between μ_+ and μ_- and hence XMCD signal were not observed in any of the bilayer films. The intensities μ_+ and μ_- overlap for all the three RuO_2 thicknesses and any difference between them were within the electrical noise level of the measurement set up. This evidence is against the possibility of any induced moment in Ru in the bilayer samples *at room temperature.*

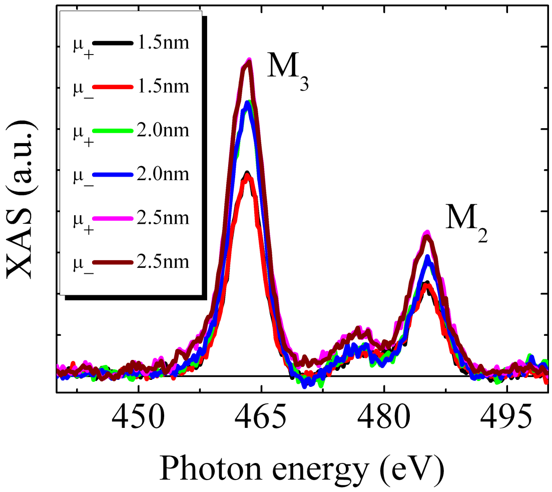

Figure 5.8: XAS at the Ru $M_{2,3}$ edges for three thicknesses of RuO_2. In the spectra, μ_+ and μ_- are for opposite magnetization directions in the films. The humps between M_2 and M_3 are identified as extended X-ray absorption fine structure (EXAFS) of Ru [69].

Cr moments in the bilayer films were estimated from the XMCD at the Cr $L_{2,3}$ edges as shown in fig. 5.9. XMCD was found to be decreasing with increasing RuO_2 thickness from 1.5 nm to 2.5 nm and estimated Cr moments were 1.2 μ_B, 1.0 μ_B and 0.8 μ_B respectively. Considering 15% error in the moment analysis when sum rules are applied on CrO_2 [64], these moment values can be considered similar.

5.8 Conclusions

In conclusion, XMCD measurements were carried out on CrO_2 thin films of (100) and (110) orientations at room temperature and the data were analyzed using XMCD sum rules. Spin moments were found to be almost 50% higher for (110) oriented films compared to (100) oriented films. Temperature-dependent bulk magnetometry measurements revealed a similar trend, with (100) films also exhibiting a slightly lower Curie temperature. We attribute these effects to the intrinsically different growth modes of

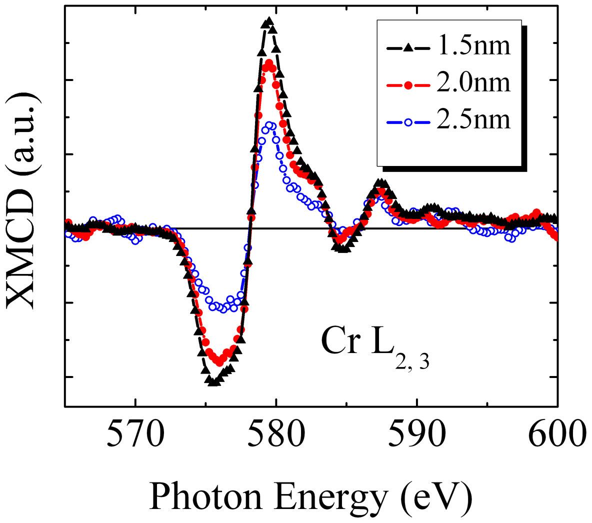

Figure 5.9: XMCD observed at the Cr $L_{2,3}$ edges from the bilayer samples. XMCD found to be decreasing with increasing RuO_2 layer thickness on top.

(100) and (110) films on TiO_2 substrates; (100) films grow strained while (110) films grow strain-free. Orbital moments were found to be the same for both orientations. XMCD experiment on (100) oriented CrO_2/RuO_2 bilayer films at room temperature did not reveal any induced moment in Ru within the resolution of the experiment.

Chapter 6

LOW PRESSURE DEPOSITION OF CrO_2 AND ITS FILM PROPERTIES

6.1 Introduction

CrO_2 is the only known half-metallic oxide showing spin polarization close to 100% at low temperatures [5, 6, 7]. High spin polarization together with a Curie temperature of about 395 K makes CrO_2 one of the most ideal candidates for magnetoelectronic devices. However, so far large magnetoresistance has not been observed in CrO_2 based devices which is in part attributed to non-collinearity of Cr spins at the interfaces [2]. Apart from that, synthesis of CrO_2 films has been challenging since CrO_2 is a metastable oxide of chromium. Cr_2O_3 is known to be the most thermodynamically stable oxide of Cr under ambient conditions. As a result, heat treatment of CrO_2 films can irreversibly reduce the film to Cr_2O_3, significantly constraining the growth of CrO_2 films.

Deposition of CrO_2 thin films is typically carried out by standard atmospheric pressure chemical vapor deposition (APCVD) method using solid CrO_3 as a precursor as shown in section 3.2. APCVD process is not amenable to heterostructure growth such as required for magnetic tunnel junctions although very good quality epitaxial CrO_2 films of (100) and (110) orientations can be prepared on TiO_2 substrates of respective orientations [41] and (0001) Al_2O_3 substrates [35]. To make it compatible with in-situ growth of heterostructures, the CrO_2 phase is desired at low pressure. However, not much is known about the phase purity of CrO_2 films prepared under low pressure conditions. Recently, the deposition temperature of CrO_2 using this precursor has been further reduced [70], but still operating at atmospheric pressure. Other than CrO_3, other precursors such as CrO_2Cl_2, $Cr(CO)_6$ and Cr_8O_{21} [71, 72, 73] have also been used to obtain good quality CrO_2 films. Though very successful in APCVD, CrO_3 is not suitable for low pressure deposition as it is corrosive to vacuum system components. Also it needs significantly high temperatures to attain a reasonable vapor pressure for deposition at low pressure. In all cases, the quality of the CrO_2 films depends strongly on substrate temperature; outside a narrow window, the thermodynamically more stable Cr_2O_3 phase is obtained. Aside from APCVD, photo dissociation of $Cr(CO)_6$ under low pressure has also been explored previously [71, 72]. However, single phase CrO_2 has not been obtained, despite the fact that CrO_2 can be stabilized well below atmospheric pressure [74].

In this chapter, low pressure chemical vapor deposition (LPCVD) of CrO_2 films is described and resulted films′ structural, surface morphology, transport, magneto-transport and surface magnetic properties are compared with APCVD films.

6.2 Deposition process

CrO_2 films under low pressure conditions were grown on (100) TiO_2 at substrate temperatures between 380-400°C. Substrates were heated with cartridge heater embedded in a copper block placed underneath the substrate and temperatures were monitored using a K-type thermocouple. As the deposition of CrO_2 is very sensitive to impurities in the substrates, TiO_2 substrates were cleaned before loading into the deposition chamber with 20% HF solution in deionized water to remove any impurity material, like in APCVD, that may come from chemical mechanical polishing of the substrates. We chose $Cr(CO)_6$ as the precursor for the process that was kept at 3 °C during deposition to maintain a low vapor pressure. Vapor pressure is determined by,

$$\log P = 8.51 - \frac{3285}{T} \tag{6.1}$$

where P is the pressure in Pascal and T is the temperature in Kelvin [71]. Before deposition was started, substrates were heated at the desired temperature for one hour in oxygen pressure of 2.0 Torr maintained with flow of 100 sccm. Oxygen was also used as the carrier gas for the precursor. Oxygen flow through the precursor was maintained at 15 sccm and the chamber pressure during deposition was maintained at 4.5 Torr during deposition. Base pressure of the system before deposition was 2.0×10^{-6} Torr achieved by pumping mechanism of a rotary pump first and then a turbo pump. Schematic diagram of the deposition system is show in fig. 6.1.

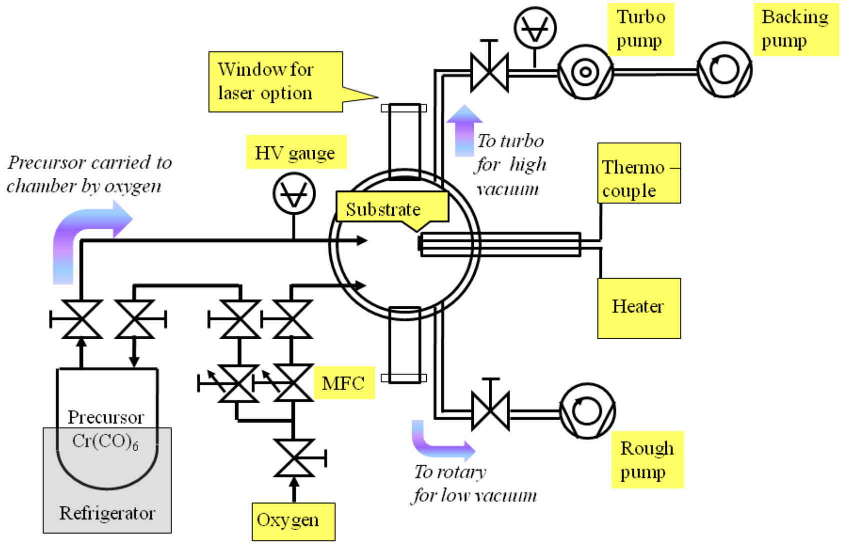

Figure 6.1: Schematic diagram of the LPCVD system showing different components and gas flow directions.

6.3 Structural properties

XRD showed CrO_2 to be the most dominant phase in the LPCVD films when substrate temperatures were between 380-400 °C with significant amount of crystalline Cr_2O_3 present in the films. Fig. 6.2 shows $(2\theta - \omega)$ scans of an LPCVD film grown at 385 °C and an APCVD film. Outside this temperature range, XRD showed Cr_2O_3 to be the only crystalline phase in the LPCVD films.

6.4 Surface morphology

Surface morphology investigated with AFM on the LPCVD films showed RMS surface roughness somewhat higher but comparable to that obtained on (100) CrO_2 films grown under APCVD conditions (1-2 nm of RMS roughness for films with thickness less than 100 nm for APCVD films [41]). Ideally atomically flat surfaces are desired for

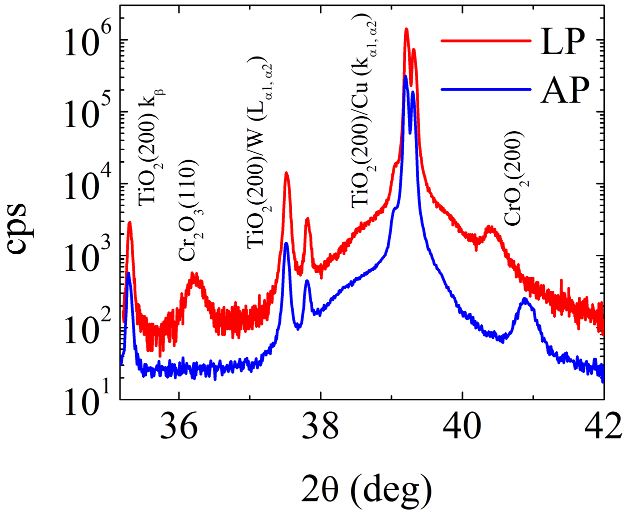

Figure 6.2: XRD pattern of the CrO_2 films prepared under LPCVD and APCVD. APCVD film shows no Cr_2O_3 peak while the peak intensities of CrO_2 and Cr_2O_3 are 5:1 in the LPCVD film. The CrO_2 peak in the AP film is away from its bulk position because of surface induced strain [41]. k_β peak and L peaks due to tungsten in the X-ray source coming from the TiO_2 substrate are identified.

spintronic devices. Roughness higher than 1 nm may make the films more susceptible to pin-holes and film discontinuity for the spacer/barrier in a GMR/TMR device.

6.5 Transport properties

Film resistivity as a function of temperature was measured in a Quantum Design Physical Property Measurement System (PPMS). For resistivity measurements, films were patterned into Hall bars (50×200 μm^2) using photolithography and ion beam etching and measured at constant current (I=100 μA) with four point probe method (similar to that shown in fig. 4.13). Fig. 6.4(a) shows the resistivity of an LPCVD film and an APCVD film from 5-400 K. Both the films had a thickness of about 55 nm. At all temperatures, LPCVD films show higher resistivity than epitaxial CrO_2 films prepared by APCVD. Moreover, LPCVD films′ resistivity was observed to be higher than that of CrO_2 film grown on Al_2O_3 substrates and polycrystalline TiO_2 substrates under

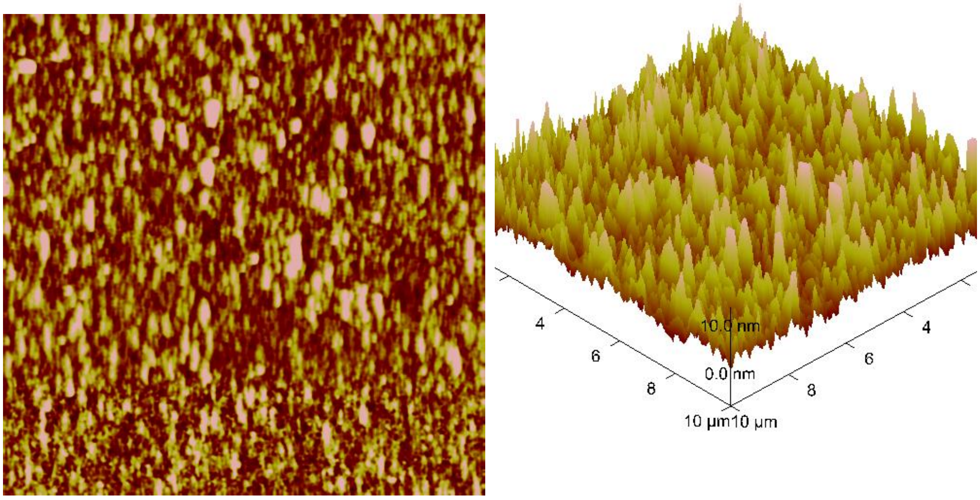

(a) (b)

Figure 6.3: 2D (a) and 3D (b) images of an AFM scan on an LPCVD film deposited for half an hour at 385 °C under the conditions mentioned above. Scan area was 10×10 μm^2. RMS surface roughness on this particular film was ~2.3 nm.

atmospheric pressure [47]. The resistivity approaches a constant value below 35 K for the APCVD film (residual resistivity ~7 $\mu\Omega$cm), which agrees well with previous reports [47, 48, 49, 75]. The residual resistivity ratio (RRR), defined as ρ(300K)/ρ(minimum), was ~1.6 for LPCVD film, much smaller than the RRR of ~45 for epitaxial (100) APCVD CrO_2 films, indicating that APCVD also show a much more sharply decreasing resistivity with decreasing temperature. The residual resistivity, ρ_{min} for LPCVD films was ~1750 $\mu\Omega$cm, far above that of APCVD films. This is expected because of the presence of a significant amount of insulating Cr_2O_3 in the LPCVD films, which is known to be an insulator and weakly anti-ferromagnetic [76]. The resistivity versus temperature for LPCVD films appears to be a convolution of an insulating Cr_2O_3 phase and a metallic CrO_2 phase present in the film, consistent with X-ray diffraction results. The resistivity of LPCVD film increases below 60 K as a result of this convolution.

In half-metallic CrO_2, one-magnon scattering should be absent at low temperatures, and hence the characteristic T^2 contribution to the resistivity should be absent. Fig. 6.4(b) shows the resistivity of the films plotted against T^2 for both APCVD and LPCVD films. In case of APCVD film, no significant T^2 dependence of resistivity was observed

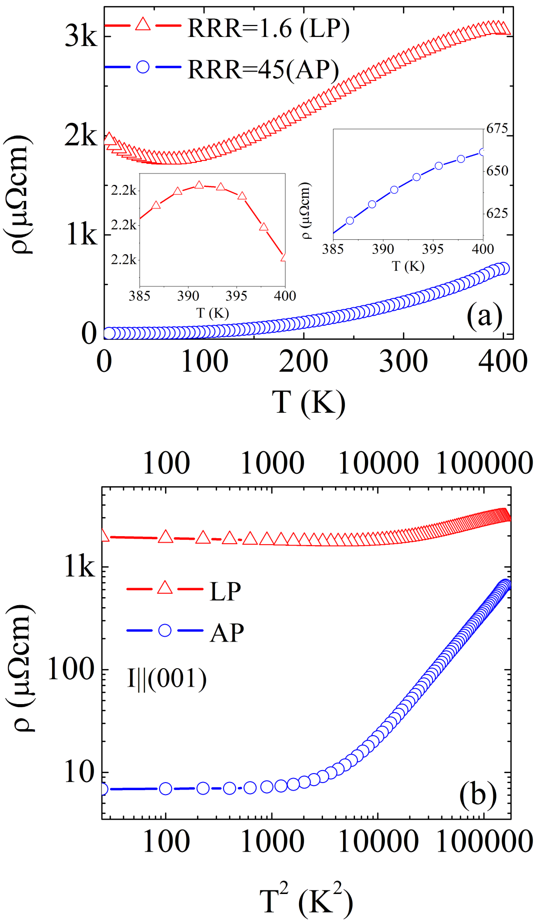

Figure 6.4: (a) Resistivity curves of LPCVD and APCVD CrO_2 films from 5-400 K. Insets show the near T_c behavior of resistivity. (b) Resistivity plotted (log-log) against T^2.

below 35 K, suggesting absence of a one-magnon channel and thus half-metallic CrO_2 [50, 51]. Using the same argument, half-metalicity of LPCVD films is questionable as significant T^2 dependence is observed below 100 K when compared to APCVD films. The T^2 dependence of resistivity in both films at higher temperatures (i.e., above 100 K) suggests coherent one-magnon scattering in conventional ferromagnetic material, as expected [50]. Thus there is spin flip scattering present in both films at these higher temperatures, i.e. both spin up and spin down channels are present at the Fermi level, invalidating any purely half-metallic nature in the films above ∼100 K. As shown in the insets of fig. 6.4(a), the slopes of the resistivity curves also change between 390-395 K, suggesting the loss of ferromagnetic state [51], which is more pronounced in case of the LPCVD film. In case of ferromagnetic metals, the contribution to the resistivity above T_c due to spin disorder can be assumed to be constant, while the phonon contribution increases linearly with increasing temperature. In case of LPCVD films, spin disorder cannot be neglected above T_c because of the presence of anti-ferromagnetic Cr_2O_3 in the films causing a more sharp change in slope near T_c.

6.6 Anisotropic magnetoresistance

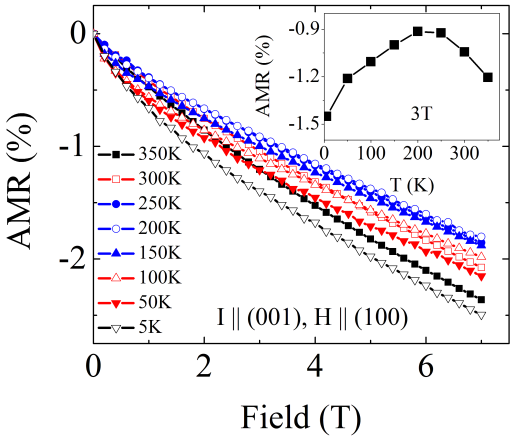

Figure 6.5: In-plane AMR of LPCVD film with current and field perpendicular to each other measured at eight different temperatures. AMR = (ρ(H) - ρ(H=0))/ρ(H=0). Inset shows the AMR at different temperatures at 3 T applied field.

For the in-plane anisotropic magnetoresistance (AMR) measurement, magnetic field was applied along (100) direction and current was applied along (001) direction of the of LPCVD films. The AMR as a function of magnetic field at a few different temperatures from 5-350 K is plotted in Fig. 6.5. The AMR for the LPCVD film is negative, suggesting a decrease in resistance due to increase in magnetic ordering with increasing magnetic field. The highest obtained AMR value is -2.6% at 5 K in an applied field of 7 T. Even at this high magnetic field, the MR is far from saturation at all temperatures, indicating that a very large field is needed to align the disordered spins along the direction of the field. This is expected if there are a large number of disordered spins in the LPCVD films due to the presence of a large fraction of non-CrO_2 phase(s). Similar MR behavior is observed in CrO_2 films on Al_2O_2 substrates [77]. The MR also decreases significantly with increasing temperature due to the increasing of spin flip scattering, [49, 78] which is similar to the MR behavior of putative half-metal $La_{(1-x)}Sr_xMnO_3$ [79]. As reported by Suzuki et al. [49], longitudinal MR in CrO_2 has a minimum around 200 K (inset in Fig. 6.5) similar to our observation.

6.7 Surface magnetic properties

In order to examine the surface magnetic properties of our films, XMCD technique was employed at room temperature (discussed in chapter 4). A significantly larger XMCD was observed at the $L_{2,3}$ edges of Cr in the APCVD films compared to the LPCVD films. One possible reason for the discrepancy is uncompensated Cr spins in the reduced Cr_2O_3 of the LPCVD film, particularly on the surface and at CrO_2/Cr_2O_3 grain boundaries, as bulk Cr_2O_3 is known to be weakly anti-ferromagnetic [76]. The amount of possible Cr_2O_3 in the APCVD film surface is neglected. The magnetic moment of Cr in CrO_2 has been estimated from XMCD data using the sum rules [58] for 3d elements and the sum rule correction factor for CrO_2 [64] for all the films. We neglected the angular moment and contribution from the O K-edge as they are negligible compared to the Cr spin moment [65, 66]. The number of holes in 3d orbital of CrO_2 is assumed to be 8 [65]. The calculated magnetic moment on the APCVD film was (1.2±0.2) μ_B, compared to (0.6±0.1) μ_B on LPCVD films. The error in the determined magnetic moment is estimated to be about 15% because of the overlap of L_2 and L_3 edges of Cr in the X-ray absorption spectra [64]. No significant XMCD was observed from a Cr_2O_3 control sample within the resolution of the instrument, and the Cr moment on this film is estimated to be within ±0.1 μ_B. The estimated magnetic moment on the APCVD and LPCVD films were smaller than the calculated and experimentally observed moment of 2.0 μ_B per Cr atom of CrO_2 at low temperature as our experiment was carried out at room temperature (∼300 K).

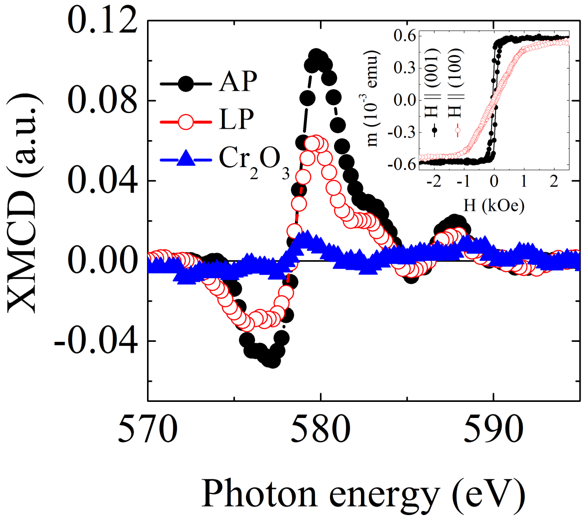

Figure 6.6: XMCD obtained from the X-ray absorption on the $L_{2,3}$ edges of Cr on CrO_2 films from LPCVD, APCVD and a Cr_2O_3 films. Inset shows the in-plane M (H) loops of an LPCVD film measured in VSM (fig. 3.11).

6.8 Conclusions

In conclusion, CrO_2 phase was found to be possible at low pressure in CVD however; it is mixed with significant amount of crystalline Cr_2O_3. Films prepared with LPCVD showed relatively higher resistivity than epitaxial CrO_2 films. AMR behavior of the (100) LPCVD films is comparable to that of epitaxial (100) CrO_2 films prepared with APCVD. XMCD showed a substantially reduced magnetic moment on the surface of LPCVD films compared to APCVD films of CrO_2 because of the presence of antiferromagnetic Cr_2O_3.

Chapter 7

TRANSPORT IN CrO_2/Cr_2O_3/Co JUNCTIONS

7.1 Introduction

Because of the high spin polarization of CrO_2, magnetic tunnel junctions with CrO_2 as an electrode have been investigated by quite a few groups all over the world. However; high TMR has not been observed in a device with CrO_2 as an electrode. As reported by Gupta et al. a negative TMR of ∼8% was observed in a CrO_2/Cr_2O_3/Co junction at 4.2 K [1]. In this junction, Cr_2O_3 is a naturally grown barrier. Leo et al. also found similar negative TMR with CrO_2 as a ferromagnetic electrode and they showed that MR sign is positive when the barrier is replaced with a thin MgO layer [3]. All these reported works are on (100) CrO_2 films grown on iso-structural TiO_2 substrates. As reported in chapter 3, (100) CrO_2 films are subject to substrate-induced strain while (110) CrO_2 films are not as these two orientations of CrO_2 follow different growth modes [41]. In this chapter, device properties of CrO_2/Cr_2O_3/Co are revisited for the (110) orientation. In the fabricated devices, TMR and I-V characteristics are reported. The natural barrier in the junction was probed with inelastic electron tunnelling spectroscopy (IETS).

7.2 TMR

To observe TMR in (110) $TiO_2/CrO_2/Cr_2O_3$ (natural barrier)/Co/Au (cap) structure, micron size devices were fabricated following the steps mentioned in section 3.12. The CrO_2 film was exposed to atmosphere during processing. Fig. 7.1(a) shows 2.5 times increase in junction resistance (8.5 kΩ to 20 kΩ) in a fabricated device with area 3×5.5 μm^2 when temperature was decreased from near room temperature to liquid nitrogen temperature. This indicates that tunnelling is the likely mode of transport in the device. An increase in junction resistance with decreasing temperature can be attributed to few factors. Although both electrodes′ resistance decreases significantly with decreasing temperature, thermal smearing of the bands in the Cr_2O_3 insulator band-gap decreases with decreasing temperature and consequently reduces the tunnelling current. Also, thermal fluctuations reduce with decreasing temperature. Increasing magnetic moment with decreasing temperature also contributes to increase in the resistance of the junction via spin dependent tunnelling. TMR observed in the device (as shown in fig. 7.1(b)) is less than 2% at 78 K and negative (using eq. 2.1). This is similar to the previously reported negative TMR of ~3% observed in the same device around liquid nitrogen temperature with epitaxial (100) CrO_2 [1, 3].

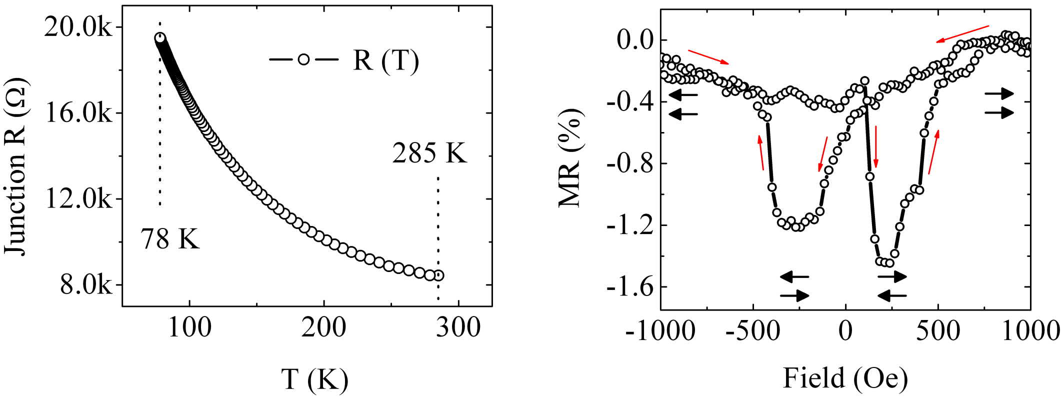

(a) (b)

Figure 7.1: (a) Resistance against temperature and (b) TMR against applied magnetic field in a 3×5.5 μm^2 device. Magnetic field was applied along the easy axis direction i.e. (001) direction of CrO_2. Switching of the top magnetic layer, Co was observed around 120 Oe at 78 K. The CrO_2 layer switched near applied field of 450 Oe. Applied current in the device was 0.1 μA. Top and bottom electrodes showed metallic conductivity with electrode resistance decreasing with decreasing temperature.

Assuming spin polarization of CrO_2 to be 98% and that of Co to be -42%, then according to Julliere model [14], TMR value for this junction is expected to be about -57%. The observed TMR is much lower than this expected value. This indicates that there is significant spin-flip process taking place at the interfaces with the barrier. As Cr_2O_3 is known to be weakly antiferromagnetic [76], significant spin-flip scattering at the barrier interfaces is not unlikely to reduce the TMR effect. Also, (110) CrO_2 follows island growth mode on iso-structural TiO_2 substrates, and (110) CrO_2 films of thickness 50 nm have surface roughness of about 1.0 nm [41]. The island growth mode and relatively higher surface roughness might possibly make the barrier less effective to observe a significant TMR effect e.g. by promoting FM coupling of the electrodes or intermixing. The sign of TMR in a CrO_2 based device is very interface sensitive [3]. However; in this fabricated device, observed negative TMR is attributed to the negative spin polarization of top Co layer while the CrO_2 layer maintains a positive spin polarization due to conduction of only majority electrons [1].

7.3 Barrier height

Like in other tunnel junctions, the barrier in $CrO_2/Cr_2O_3/Co$ junction can be studied by observing the current through the device as a function of applied bias voltage. A schematic energy diagram of this junction is shown in fig. 7.2. Barrier height (φ) is the potential barrier provided by the insulator of thickness d between the ferromagnetic electrodes. Asymmetry in the barrier arises because of the different work functions involved with CrO_2 and Co. When no bias is applied, the Fermi levels of CrO_2 and Co are at the same energy (Fermi level is the highest occupied energy level at absolute temperature). With an applied bias voltage of V, the Fermi levels shift by eV relative to each other (e is the charge of an electron). For the electrons to tunnel through the barrier from one electrode to the other, it is required that there are available empty states in the other electrode.

Based on the I-V characteristics of a tunnelling device, its barrier height can be estimated. Two models are used and compared to estimate the energy barrier in the device Simmons model [80] and Brinkman model [81] as described below.

7.3.1 Simmons model

Simmons assumed a rectangular shaped ideal barrier between two metallic electrodes. According to his model, current density across the junction for intermediate voltages can

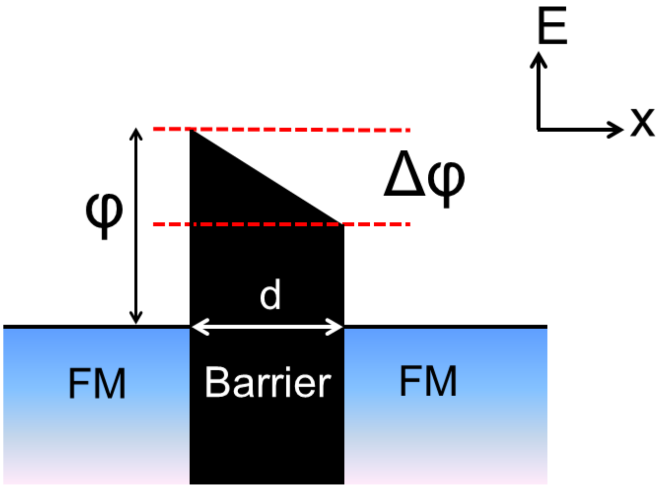

Figure 7.2: Schematic diagram showing the barrier height (φ) and barrier asymmetry ($\Delta\varphi$) in ferromagnetic(FM)|insulator(thickness d)|ferromagnetic(FM) junction at zero bias. Shaded region in the FM electrodes are occupied states and above them are the unoccupied states (no shading). Current through the junction is due to quantum mechanical tunnelling of electrons through the barrier.

be approximated by the following expression:

$$J = \beta(V + \gamma V^3) \tag{7.1}$$

where,

$$\beta = \frac{3}{2d}\left(\frac{e}{\hbar}\right)^2 (2m\varphi)^{1/2} exp\left[-\left(\frac{4\pi d}{\hbar}\right)(2m\varphi)^{1/2}\right] \tag{7.2}$$

and,

$$\gamma = \frac{\pi m}{3\varphi(ed/\hbar)^2} \tag{7.3}$$

Here, φ is the potential barrier height in eV, d is the barrier thickness in nm, m is the mass of electron and $\hbar$ is reduced Planks constant. For low bias, eq. 7.1 can further be approximated to J=βV neglecting the cubic potential term. Simmons model does not give a very good fitting of the current densities against applied bias voltage as can be seen in fig. 7.3. Conversely, it suggests that the barrier in this junction is highly asymmetric which can not be accounted for in Simmons model. From Simmons model, barrier height was found to be 0.42 eV at 78 K with a barrier thickness of 1.3 nm. Also, the effective barrier thickness obtained with Simmons fitting is close to lattice parameter c in crystalline Cr_2O_3 (a=0.496 nm, c=1.36 nm for hexagonal corundum structure [83]) assuming that temperature dependence of lattice parameter is not very significant [84].

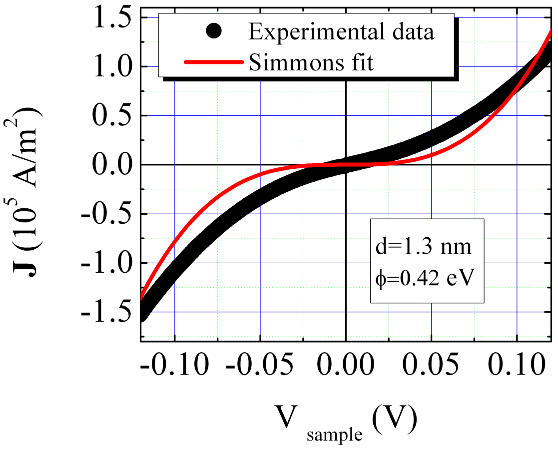

Figure 7.3: Current density plot of a 3×5.5 μm^2 device against applied bias voltage. Bias voltage was swept at least ten times between ±0.12 V to obtain the average current density. Obtained barrier thickness and barrier height are mentioned.

7.3.2 Brinkman model

The Brinkman-Dynes and Rowell (BDR) model assumes a trapezoidal barrier as shown in figure 6.1 which is more realistic for an asymmetric junction like $CrO_2/Cr_2O_3/Co$. Along with the barrier height (φ) and barrier thickness (d), barrier asymmetry ($\Delta\varphi$) can also be estimated with the BDR model. According to this model, conductance of the junction is expressed as a polynomial function of bias voltage upto 2nd order:

$$\frac{dI}{dV} = A + BV + CV^2 \tag{7.4}$$

and integrating this expression we can obtain the current in the device against bias voltage:

$$I = AV + B\frac{V^2}{2} + C\frac{V^3}{3} \tag{7.5}$$

where A, B and C are constants evaluated by fitting experimental data. The constant of integration is zero considering the fact that there is no voltage offset during the measurement [I(V=0)=0]. On getting the constants A, B and C from fitting, barrier thickness (in Å), barrier height (in eV) and barrier asymmetry (in eV) can be calculated from the following expressions according to BDR model:

$$d^2 = -5.368\sqrt{\frac{C}{A}}\ln\left(1.747 \times 10^{-10}\sqrt{\frac{C}{A}}\right) \tag{7.6}$$

$$\varphi = 0.0328\left(\frac{A}{C}\right)d^2 \tag{7.7}$$

$$\Delta\varphi = -23.42\left(\frac{B}{A}\right)\frac{\varphi^{3/2}}{d} \tag{7.8}$$

Fundamental constants arising in the expressions are taken care of by the numerical coefficients in expressions 7.6 - 7.8. Both conductance (dI/dV) and current (I) against applied bias voltage are fitted with Brinkman model. Fig. 7.4(a) shows the experimental conductance data and Brinkman fit with eq. 7.4 and fig. 7.4(b) shows the current through the device and Brinkman fit using eq. 7.5 against bias voltage. Both conductance and current fitting with Brinkman model gives exactly same barrier thickness of 4.0 nm, which is larger than that obtained with Simmons model. Also, this barrier thickness is close to three times the lattice parameter c in Cr_2O_3 (c=1.36 nm) - perhaps more physically reasonable. This indicates that, effectively we have three unit cells of Cr_2O_3 as the barrier between the ferromagnetic layers i.e. CrO_2 and Co. Both fittings gave higher barrier asymmetry than barrier height, which is seemingly unphysical as barrier asymmetry is considered as a small perturbation to the actual barrier height in BDR model. This suggests that multiple barrier height fitting is more suitable for this junction. Considering effective barrier height to be $\varphi + \Delta\varphi/2$, from conductance fit effective barrier is 0.45 eV and from current fit it is 0.37 eV both similar to barrier height obtained from Simmons fit which is 0.42 eV. This barrier height is smaller than the barrier height of 0.76 eV reported by Barry et al. in a similar junction [82]. All these barrier heights are again much smaller than the energy gap of 3.0 eV between the conduction band and the valance band of Cr_2O_3 observed by Cheng et al. in XPS study of naturally grown Cr_2O_3 insulator on CrO_2 metallic surface [85].

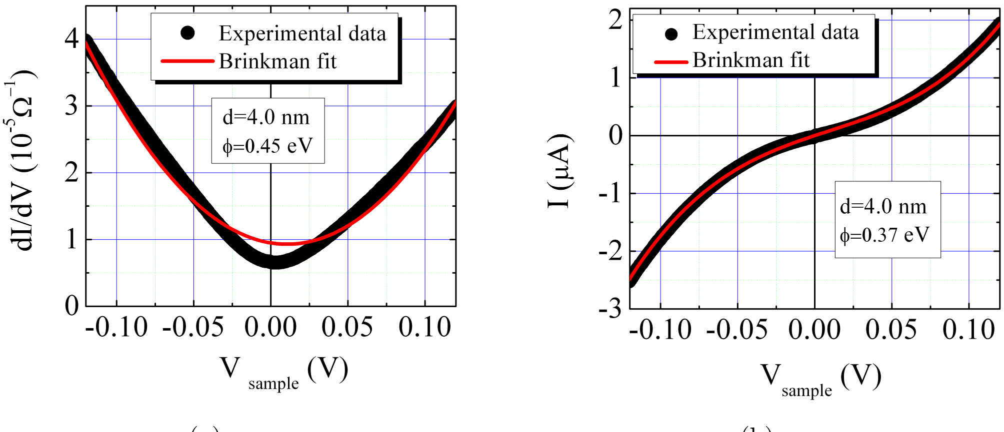

(a) (b)

Figure 7.4: Experimental data and Brinkman fit for (a) conductance vs. bias voltage and (b) current vs. bias voltage. Parameters calculated from fit are mentioned.

7.4 IETS

7.4.1 Inelastic tunneling of electrons

When electrons tunnel through an insulating barrier between two metals without interacting with the barrier material, their total energy is not altered and this is called elastic tunnelling. However, if the applied bias is such that it is enough to excite a particular characteristic vibrational mode between atoms in the barrier, tunnelling electrons will lose energy in the barrier to excite those particular vibrational modes. Accordingly, we see an increase in current due to this additional conduction channel. Due to this increase in current at a certain voltage, derivative of current with respect to voltage is a step function and the 2nd derivative of current is observed as a peak at that voltage. This inelastic tunnelling of electrons is qualitatively shown in fig. 7.5 above. Compared to the total current through the junction, this increase in current due to inelastic tunnelling is very small within 1% of the total current, and therefore it may not be more significant than the electrical noise level at room temperature. Further, the FWHM of the peak in this inelastic electron tunnelling spectroscopy (IETS) has a temperature dependence of 5.4k_BT [86] and therefore to obtain a significant resolution, spectra were taken at 2 K which corresponds to a thermal broadening of 0.93 mV. Because of asymmetry in barrier energy, inelastic tunnelling electrons also see different barrier height depending on the bias polarity and accordingly their peak intensities can depend on the bias voltage polarity of the device [87].

7.4.2 Measurement technique

Although it seem straightforward to observe the IETS peaks by taking the 2nd derivative (d^2I/dV^2) of the I-V spectra, it is typically a very poor method, mainly because of the unfavorable signal to noise ratio at any temperature. IETS spectra are usually obtained by a more sensitive technique of applying a small ac modulation voltage with the applied dc bias. Considering the ac bias to be significantly smaller than the dc bias, Taylor expansion of the current about the dc bias shows that conductance (1st derivative) and

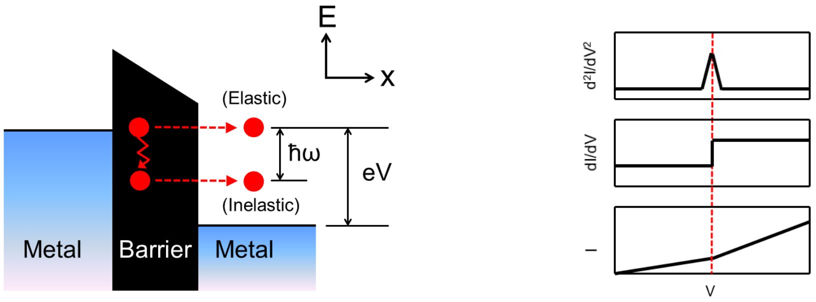

(a)

(b)

Figure 7.5: (a) schematic diagram for inelastic tunnelling of electrons together with elastic tunnelling of electrons through an insulating barrier between two metals (b) corresponding change in current (I), conductance (dI/dV) and derivative of conductance (d^2I/dV^2) due to inelastic tunnelling of electrons.

IETS (2nd derivative) can be obtained using this ac modulation technique:

$$\begin{aligned} I(V_b + V_m cos\omega t) = I(V_b) + \frac{dI}{dV} \mid V_b V_m cos\omega t \\ + \frac{d^2I}{dV^2} \mid_{V_b} V_m cos\omega t + \dots \end{aligned} \tag{7.9}$$

Lock-in amplifiers are used to determine the conductance and IETS signals as first and second harmonics respectively. For a bias voltage of 150 mV, modulation voltage was 1-2 mV with modulation frequency ∼1 kHz to avoid any low frequency noise. Since the bandwidth of lock-in measurement is very small, this technique also vastly improves SNR. For a good energy resolution, a low modulation voltage is desired, while for a good SNR, a high modulation voltage is desired. Calculated minimum energy resolution due to ac modulation is 1.22Vm [86] and therefore for an ac modulation of 2 mV, IETS spectra can be confirmed to be correct within ±2.5 mV. Modulation broadening of the IETS spectra is therefore on the same order as thermal broadening at 2 K which is about 1.0 mV.

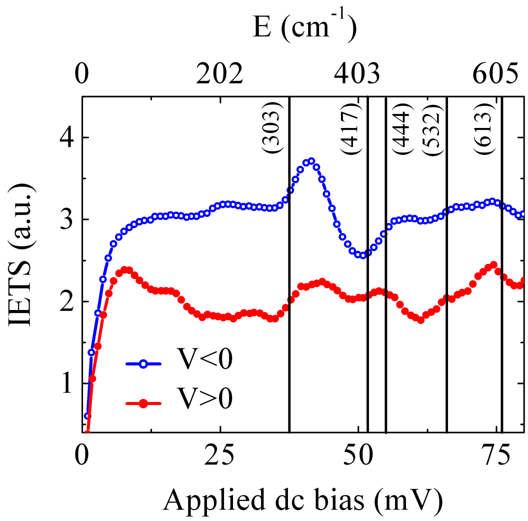

Figure 7.6: IETS spectra obtained on a $CrO_2/Cr_2O_3/Co$ junction (area 3×5.5 μm^2) at 2 K for positive and negative bias between CrO_2 and Co electrodes. Corresponding vibrational energies in cm^{-1} are shown in brackets for applied dc bias. Vertical lines indicate position of a few vibrational modes of Cr_2O_3 obtained from infrared spectroscopy [88].

7.4.3 IETS spectra from (110) $CrO_2/Cr_2O_3/Co$ tunnel junction

Fig. 7.6 shows the IETS spectra obtained on the $CrO_2/Cr_2O_3/Co$ junction at 2 K for positive and negative biases. Observed intensities in the spectra were smaller for positive bias between CrO_2 and Co than negative bias and correspondingly peak intensities are also smaller for positive bias. Energies of the vibrational modes in bulk Cr_2O_3 obtained with infrared spectroscopy are shown in by the vertical lines (1 eV=8.065 cm^{-1}). From left to right, the positions of these lines are 303, 419, 444, 532 and 613 cm^{-1}, respectively [88]. Considering the peak positions to be correct within ±2.5 mV and comparing with the available data, these peak positions can be confirmed to be due to the excitation of the vibrational modes in the thin insulating Cr_2O_3 barrier in the tunnel junction. Further, the presence of inelastic peaks confirms that tunnelling is present in the device, and not purely a metallic short, since only ballistic transport can give rise to IETS. Because of the strong bias and temperature dependence of the IETS spectra, it was not corrected for the elastic tunnelling background. Reported spectra are averaged from 10 scans between

±100 mV.

7.5 Conclusions

In conclusion, fabricated (110) CrO_2/Cr_2O_3/Co tunnel junction was investigated for TMR and its I-V characteristics. The junction showed similar TMR behavior previously reported with (100) CrO_2 as an electrode. Barrier height obtained from the I-V characteristics of the junction is about 0.40 eV. The IETS spectra had significant bias dependence and the IETS peak positions showed vibrational modes of Cr_2O_3 that are close to those in bulk Cr_2O_3.

Chapter 8

SUMMARY

- (100) CrO_2 films grows layer by layer and (110) CrO_2 film follows island growth mode on isostructural TiO_2 substrates. Because of their different growth modes, (100) CrO_2 films are subject to substrate-induced strain while (110) CrO_2 films are strain free in all lattice directions.

- Substrate-induced strain can effect the magnetic moment in CrO_2 thin films. Bulk and surface magnetic moment is reduced at room temperature in strained (100) CrO_2 films compared to strain free (110) CrO_2 films .

- CrO_2 phase is possible in lower than atmospheric pressure. Biphasic CrO_2/Cr_2O_3 films obtained in low pressure were characterized for film properties.

- MTJ′s were fabricated with (110) CrO_2 as an electrode. The (110) $CrO_2/Cr_2O_3/Co$ tunnel junction showed negative TMR of $\sim$2% at 78 K & junction I-V characteristics were obtained. Barrier height in this junction was estimated to be $\sim$0.4 eV. Vibrational modes of Cr_2O_3 were observed in IETS spectra of this junction.

Bibliography

[1] A. Gupta, X. W. Li, Gang Xiao, Appl. Phys. Lett. **78**, 1894 (2001)

[2] G. X. Miao, A. Gupta, H. Sims, W. H. Butler, S. Ghosh, Gang Xiao, J. Appl. Phys. **97**, 10C924 (2005)

[3] Titus Leo, Christian Kaiser, Hyunsoo Yang, Stuart S. P. Parkin, Martin Sperlich, Gernot Gntherordt, David J. Smith, Appl. Phys. Lett. **91**, 252506 (2007)

[4] M. A. Korotin, V. I. Anisimov, D. I. Khomskii, G. A. Sawatzky, Phy. Rev. Lett. **80**, 4305 (1998)

[5] J. Parker, S. Watts, P. Ivanov, P. Xiong, Phys. Rev. Lett. **88**, 196601 (2002)

[6] A. Anguelouch, A. Gupta, G. Xiao, D. W. Abraham, Y. Ji, S. Ingvarsson, C. L. Chein, Phys. Rev. B **64**, R180408 (2001)

[7] K. A. Yates, W. R. Branford, F. Magnus, Y. Miyoshi, B. Morris, L. F. Cohen, P. M. Sousa, O. Konde, A. J. Silvestre, Appl. Phys. Lett. **91**, 172504 (2007)

[8] M. N Baibich, J. M. Broto, A. Fert, F. Nguyen Van Dau, F. Petroff, P. Eitenne, G. Greuzet, A. Friederich, J. Chazelas, Phys. Rev. Lett. **61**, 2472 (1988)

[9] G. Binash, P. Grnberg, F. Saurenbach, W. Zinn, Phys. Rev. B **39**, 4828 (1989)

[10] N. F. Mott, Proc. Royal Soc. **156**, 368 (1936)

[11] N. F. Mott, Adv. Phys. **13**, 325 (1964)

[12] E. Y. Tsymbal, D. G. Pettifor, Solid State Physics, edited by H. Ehrenreich and F. Spaepen, Vol. **56** (Academic Press, 2001) pp. 113-237

[13] Ivar Giaever, Phys. Rev. Lett. **5**, 147 (1960)

[14] M. Julliere, Phys. Lett. **54A**, 225 (1975)

[15] J. S. Moodera, Lisa R. Kinder, Terrilyn M. Wong, R. Meservey, Phys. Rev. Lett. **74**, 3273 (1995)

[16] T. Miyazaki, N. Tezuka, J. Magn. Magn. Mater. **139**, L231 (1995)

[17] W. H. Butler, X-G. Zhang, T. C. Schulthess, J. M. MacLaren, Phys. Rev. B **63**, 054416 (2001)

[18] J. Mathon, A. Umerski, Phys. Rev B **63**, 220403(R) (2001)

[19] Stuart S. P. Parkin, Christian Kaiser, Alex Panchula, Philip M. Rice, Brian Hughes, Mahesh Samant, See-hun Yang, Nature Mater. **3**, 862 (2004)

[20] S. Yuasa, A. Fukushima, H. Kubota, Y. Suzuki, K. Ando, Appl. Phys. Lett. **89**, 042505 (2006)

[21] S. Ikeda, J. Hayakawa, Y. Ashijawa, Y. M. Lee, K. Miura, H. Hasegawa, M. Tsunoda, F. Matsukura, H. Ohno, Appl. Phys. Lett. **93**, 082508 (2008)

[22] L. Berger, Phys. Rev. B **54**, 9353 (1996)

[23] J. Slonczewski, J. Magn. Magn. Mater. **159**, L1 (1996)

[24] A. Slavin, V Tiberkevich, IEEE Trans. Mag. **45** 4, 1875 (2009)

[25] J. A. Katine, F. J. Albert, R. A. Buhrman, E. B. Myers, D. C. Ralph, Phys. Rev. Lett. **84**, 3149 (2000)

[26] S. S. P. Parkin, R. Bharda, and K. P. Roche, Phys. Rev. Lett. **66**, 2152 (1991)

[27] S.Yuasa, T. Nagahama, A. Fukushima, Y. Suzuki, K. Ando, Nature Mater. **3**, 868 (2004)

[28] R. Matsumoto, A. Fukushima, T. Nagahama, Y. Suzuki, K. Ando, S. Yuasa, Appl. Phys. Lett. **90**, 252506 (2007)

[29] D. D. Djayapravira, K. Tsunekawa, M. Nagai, H. Maehara, S. Yamagata, N. Watanabe, S. Yuasa, Y. Suzuki, K. Ando, Appl. Phys. Lett **86**, 092502 (2005)

[30] J. Hayakawa, S. Ikeda, Y. M. Lee, F. Matsukura, O. Ohno, Appl. Phys. Lett. **89**, 232510 (2006)

[31] M. Oogane, Y. Sakuraba, J. Nakata, H. Kubota, Y. Ando, A. Sakuma, T. Miyazaki, J. Phys. D: Appl. Phys. **39**, 834 (2006)

[32] Y. Ishii, H. Yamada, H. Sato, H. Akoh, Y. Ogawa, M. Kawasaki, Y. Tokura, Appl. Phys. Lett. **89**, 042509 (2006)

[33] B. L. Chamberland, Critical review in solid state & materials sciences **7**, 1 (1-31) 1977

[34] A. Gupta, X. W. Li, S. Guha, G. Xiao, Appl. Phys. Lett. **75**, 2996 (1999)

[35] M. Rabe, J. Pommer, K. Samm, B. Ozyilmaz, C. Konig, M. Fraune, U. Rudiger, G. Guntherodt, S. Senz, and D. Hesse, J. Phys.: Cond. Matt. **14**, 7 (2002)

[36] G. Miao, G. Xiao, and A. Gupta, Phys. Rev. B **71**, 094418 (2005)

[37] S. Ishibashi, T. Namikawa, M. Satou, Mat. Res. Bull. **14**, 51 (1979)

[38] Milton Ohring, Material science of thin films deposition and structure, Academic press, San Diego, 2nd edition, 2002, page 215

[39] Neil W. Ashcroft, N. David Mermin, Solid state physics, Thomson Brooks/Cole, 3rd Indian reprint, Delhi, 2007, page 752

[40] Stephen A. Campbell, The science and engineering of microelectronic fabrication, 2nd edition, Oxford University Press, NY 10016, 2001 chapters 7 & 8

[41] K. B. Chetry, M. Pathak, P. LeClair, A. Gupta, J. Appl. Phys., **105**, 083925 (2009)

[42] M. U. Cohen, Rev. Sci. Instrum. 6, 68 (1935)

[43] J. I. Langford, J. Appl. Cryst. 6, 190 (1973)

[44] B. D. Cullity, S. R. Stock, Elements of X-ray diffraction, 3rd edition, Prentice Hall, NJ 07458, 2001, pages 376-381

[45] Charles Kittel, Introduction to solid state physics, 7th edition, John Wiley & Sons, Inc. Singapore, 2000, page 49

[46] Mario Birkholz, Thin film analysis by X-ray scattering (2006), WILEY-VCH Verlag GmbH & Co. KGaA, Weiheim, pages 332-337

[47] A. Gupta, X. W. Li, Gang Xiao, J. Appl. Phys. 87, 6073 (2000)

[48] A. Barry, J. M. D. Coey, L. Ranno, K. Ounadjela, J. Appl. Phys. 83, 7166 (1998)

[49] K. Suzuki, P. M. Tedrow, Phys. Rev. B, 58, 11597 (1998)

[50] C. G. F. Blum, C. A. Jenkins, J. Barth, C. Felser, S. Wurmehl, G. Friemel, C. Hess, G. Behr, B, Buchner, A. Reller, S. Reigg, S. G. Ebbinghaus, T. Ellis, P. J. Jacobs, J. T. Kohlhepp, H. J. M. Swagten, Appl. Phys. Lett. 95, 161903 (2009)

[51] M. J. Otto, R. A. M. van Woerden, P. J. van der Valk, J. Wijngaard, C. F. van Bruggen, C Haas, J. Phys: Condens. Matter, 1, 2351 (1989)

[52] G. Schtz, W. Wagner, W. Wilhelm, P. Kienle, R. Zeller, R. Frahm, G. Materlik, Phys. Rev. Lett. 58, 737 (1987)

[53] J. Stöhr, J. Magn. Magn. Mater. 200, 470 (1999)

[54] H. Ebert, J. Sthr, S. S. P. Parkin, M. Samant, A. Nilsson, Phys. Rev. B 53, 16067 (1996)

[55] J. Stöhr, Y. Wu, in: A. S. Schlachter, F. J. Wuilleumier, (Eds.), New Direction in Research with Third GenerationSoft X-ray Synchrotron Radiation Sources, Kluwer Academic Publishers, Netherlands, 1994, page 221

[56] B. T. Thole, Paolo Carra, F. Sette, G. van der Laan, Phys. Rev. Lett. 68, 1943 (1992)

[57] Paolo Carra, B. T. Thole, Massimo Altarelli, Xingdong Wang, Phys. Rev. Lett. 70, 694 (1993)

[58] C. T. Chen, Y. U. Idzerda, H. J. Lin, N. V. Smith, G. Meigs, E. Chaban, G. H. Ho, E. Pellegrin, F. Sette, Phys. Rev. Lett, 75, 152 (1995)

[59] D. A. Shirley, Phys. Rev. B 5, 4709 (1972)

[60] J. E. Castle, A. M. Salvi, J. Vac. Sci. Technol. A 19(4) 1170 (2001)

[61] Peak fitting in XPS, Casa XPS software manual (2006).

[62] S. Gold, E. Goering, C. Konig, U. Rudiger, G. Guntherodt, G. Schutz, Phys. Rev. B, 71 220404(R) (2005)

[63] M. Komelj, C. Ederer, M. Fähnle, Phys. Rev B, 69, 132409 (2004)

[64] E. Goering, Philosophical Magazine 85, 2895 (2005)

[65] E. Goering, A. Bayer, S. Gold, G. Schutz, M. Rabe, U. Rudiger, G. Guntherodt, Phys. Rev. Lett. 88, 207203 (2002)

[66] D. J. Huang, H. T. Jeng, C. F. Chang, G. Y. Guo, J. Chen, W. P. Wu, S. C. Chung, S. G. Shyu, C. C. Wu, H. J. Lin, C. T. Chen, Phys. Rev. B, 66 174440 (2002)

[67] A. J. Millis, T. Darling, A. Migliori, J. Appl. Phys., 83 1588 (1998)

[68] G. X. Miao, A. Gupta, H. Sims, W. H. Butler, S. Ghosh, Gang Xiao, J. Appl. Phys. 97, 10C924 (2005)

[69] M. A. Tomaz, Tao Lin, G. R. Harp, E. Hallin, T. K. Sham, W. L. OBrien, J. Vac. Sci. Technol. A 16(3), 1359 (1998)

[70] P. M. Sousa, S. A. Dias, A. J. Silvestre, O. Conde, B. Morris, K. A. Yates, W. R. Branford, L. F. Cohen, Chem. Vap. Deposition 12, 712 (2006)

[71] F. Keith Perkins, C. Hwang, M. Onnelion, Yoon-Gi Kim, P. A. Dowben, Thin Solid Films, 198, 317 (1991)

[72] R. Cheng, C. N. Borca, P. A. Dowben, S. Stadler, Y. U. Idzerda, Appl. Phys. Lett. 78, 521 (2001)

[73] P. G. Ivanov, S. M. Watts, D. M. Lind, J. Appl. Phys. 89, 1035 (2001)

[74] N. J. C. Ingle, R. H. Hammond, M. R. Beasley, J. Appl. Phys. 89, 4631 (2001)

[75] P. M. Sousa, S. A. Dias, O. Konde, A. J. Silvestre, W. R. Branford, B. Morris, K. A. Yates, L. F. Cohen, Chem. Vap. Deposition 13, 537 (2007)

[76] T. R. McGuire, E. J. Scott, F. H. Grannis, Phy. Rev. 102, 1000 (1956)

[77] Q. Jhao, J. J. Yuan, G. H. Wen, G. T. Zou, J. Magn. Magn. Mater. 320, 2356 (2008)

[78] W. R. Branford, K. A. Yates, E. Barkhoudarov, J. D. Moore, K. Morrison, F. Magnus, Y. Miyoshi, P. M. Sousa, O. Konde, Silvestre, L. F. Cohen, Phys. Rev. Lett 102, 227201 (2009)

[79] A. Urushibara, Y. Moritomo, T. Arima, A. Asamitsu, G. Kido, Y. Tokura, Phys. Rev. B 51, 14103 (1995)

[80] John G. Simmons, George J. Unterkofler, J. Appl. Phys. 34, 1828 (1963)

[81] W. F. Brinkman, R. C. Dynes, J. M. Rowell, J. Appl. Phys. 41, 1915 (1970)

[82] A. Barry, J. M. D. Coey, M. Viret, J. Phys.: Condens. Matter 12, L173 (2000)

[83] G. K. Lewis Jr., H. G. Drickamer, J. Chem. Phys. 45, 224 (1966)

[84] S. Greenwald, Nature 168, 379 (1951)

[85] R. Cheng, B. Xu, C. N. Borca, A. Sokolov, C. S. Yang, L. Yuan, S. H. Liou, B. Doudin, P. A. Dowben, Appl. Phys. Lett. 79, 3122 (2001)

[86] P. K. Hansma, Tunneling spectroscopy: capabilities, applications, and new techniques, Plenum Press, New York, 1982

[87] James W. Reiner, Sharon Cui, Zuoguang Liu, Miaomiao Wang, Charles H. Ahn, T. P. Ma, Adv. Mater. XX, 1-7 2010

[88] D. R. Renneke, D. W. Lynch, Phys. Rev. 138, A530 (1965)

List of publications

1 **M. Pathak**, X. Zhang, P. LeClair, A. Gupta, *Barrier height and tunnelling aspects of (110)*$CrO_2/Cr_2O_3/Co$ *junctions*, manuscript in preparation.

2 **M. Pathak**, Z. R. Tadisina, A. Natarajarathinam, P. LeClair, S. Gupta, *Effect of vanadium concentration on the magnetic moment in CoFeB thin films*, under review.

3 H. Sato, **M. Pathak**, D. Mazumdar, X. Zhang, G. J. Mankey, P. R. LeClair, A. Gupta, *Anomalous Hall behavior in (100) and (110)* CrO_2 *thin films*, under review.

4 **M. Pathak**, H. Sato, X. Zhang, K. B. Chetry, D. Mazumdar, P. LeClair, A. Gupta, *Substrate induced strain and its effect in* CrO_2 *thin films*, J. Appl. Phys. **108**, 053713 (2010)

5 **M. Pathak**, X. Zhong, J. Wang, X. Zhang, T. M. Klein, P. LeClair, A. Gupta, *Comparing magneto-transport and surface magnetic properties of half-metallic* CrO_2 *grown by low pressure and atmospheric pressure chemical vapor deposition*, Appl. Phys. Lett. **96**, 112507 (2010).

6 J. Wang, **M. Pathak**, X. Zhong, P. LeClair, T. M. Klein, A. Gupta, *Epitaxial film growth of chromium dioxide by low pressure chemical vapor deposition using chromium carbonyl*, Thin solid films **518**, 6853 (2010).

7 **M. Pathak**, H. Sims, K. B. Chetry, D. Mazumdar, P. LeClair, G. J. Mankey, W. H. Butler, A. Gupta, *Robust room temperature magnetism of (110)* CrO_2 *thin films*, Phys. Rev. B. **80**, 212405 (2009).

8 K. B. Chetry, **M. Pathak**, P. LeClair, A. Gupta, *Structural and magnetic properties of (100) and (110) oriented epitaxial* CrO_2 *films*, J. Appl. Phys. **105**, 083925 (2009).

9 H. Lee, L. Wen, **M. Pathak**, P. Janssen, P. LeClair, C. Alexander, C. K. A. Mewes, T. Mewes, *Spin pumping in* $Co_{56}Fe_{24}B_{20}$ *multilayer systems*, J. Phys. D: Appl. Phys. **41**, 215001 (2008).

Appendix A: Cohen′s method for tetragonal structure

This is a statistical approach, derived from Bragg′s law to determine lattice constants in our epitaxial (100) and (110) CrO_2 films with tetragonal unit cells. We do not need more than $(2\theta - \omega)$ scans to apply Cohen′s method.
By definition of error we have,

$$sin^2\theta(measurement) - sin^2\theta(true) = \Delta sin^2\theta(measurement) = error \tag{A.1}$$

Bragg′s law:

$$\begin{aligned} 2dsin\theta &= \lambda \\ sin^2\theta &= \lambda^2/4d^2 \\ \ln sin^2\theta &= \ln \lambda^2/4 - 2\ln d \\ \Delta sin^2\theta/sin^2\theta &= -2\Delta d/d \end{aligned} \tag{A.2}$$

Also, for a tetragonal lattice,

$$sin^2\theta(true) = \frac{\lambda^2}{4d^2} = \frac{\lambda^2}{4}\left(\frac{h^2}{a^2} + \frac{k^2}{b^2} + \frac{l^2}{c^2}\right) \tag{A.3}$$

Therefore,

$$\begin{aligned} sin^2\theta(measurement) - \frac{\lambda^2}{4}\left(\frac{h^2}{a^2} + \frac{k^2}{b^2} + \frac{l^2}{c^2}\right) &= error \\ sin^2\theta(measurement) - \frac{\lambda^2}{4}\left(\frac{h^2}{a^2} + \frac{k^2}{b^2} + \frac{l^2}{c^2}\right) &= error \\ \frac{\lambda^2}{4}\left(\frac{h^2}{a^2} + \frac{k^2}{b^2} + \frac{l^2}{c^2}\right) + error &= sin^2\theta(measurement) \\ A\alpha + B\beta + C\gamma + D\delta &= sin^2\theta(measurement) \end{aligned} \tag{A.4}$$

Where we have introduced the error function,

$$\delta = 10sin^2(2\theta)\left(\frac{1}{sin\theta} + \frac{1}{\theta}\right), [1]$$

and

$$\alpha = h^2, \beta = k^2, \gamma = l^2, A = \lambda^2/4a^2, B = \lambda^2/4b^2, C = \lambda^2/4c^2$$

Now, rewriting the error,

$$\begin{aligned} e &= A\alpha + B\beta + C\gamma + D\delta - sin^2\theta \\ e^2 &= (A\alpha + B\beta + C\gamma + D\delta - sin^2\theta)^2 \end{aligned} \tag{A.5}$$

which gives,

$$\begin{aligned} \sum e^2 = (A\alpha_1 + B\beta_1 + C\gamma_1 + D\delta_1 - sin^2\theta_1)^2 + \\ + (A\alpha_2 + B\beta_2 + C\gamma_2 + D\delta_2 - sin^2\theta_2)^2 + \ldots \end{aligned} \tag{A.6}$$

The values A-D are determined such that the summation of square error is minimized (least square). In order to accomplish this, the derivative of the summation for square error are calculated.

$$\frac{\partial \sum e^2}{\partial A} = \Sigma\alpha(A\alpha + B\beta + C\gamma + D\delta - sin^2\theta) = 0 \tag{A.7}$$

$$\frac{\partial \sum e^2}{\partial B} = \Sigma\beta(A\alpha + B\beta + C\gamma + D\delta - sin^2\theta) = 0 \tag{A.8}$$

$$\frac{\partial \sum e^2}{\partial C} = \Sigma\gamma(A\alpha + B\beta + C\gamma + D\delta - sin^2\theta) = 0 \tag{A.9}$$

$$\frac{\partial \sum e^2}{\partial D} = \Sigma\delta(A\alpha + B\beta + C\gamma + D\delta - sin^2\theta) = 0 \tag{A.10}$$

Therefore, we need to choose several planes for diffraction. Five planes are chosen and diffraction angles, 2θ are obtained. Above equations are solved for A, B, C and D. Taking the *sine* part to the right side, these equations can also be solved in the following matrix representation. Here i=1-5 stand for different planes: (h_1, k_1, l_1) - (h_5, k_5, l_5).

$$\begin{pmatrix} \sum\alpha_i^2 & \sum\alpha_i\beta_i & \sum\alpha_i\gamma_i & \sum\alpha_i\delta_i \\ \sum\alpha_i\beta_i & \sum\beta_i^2 & \sum\beta_i\gamma_i & \sum\beta_i\delta_i \\ \sum\alpha_i\gamma_i & \sum\gamma_i\beta_i & \sum\gamma_i^2 & \sum\gamma_i\delta_i \\ \sum\alpha_i\delta_i & \sum\beta_i\delta_i & \sum\gamma_i\delta_i & \sum\delta_i^2 \end{pmatrix} \begin{pmatrix} A \\ B \\ C \\ D \end{pmatrix} = \begin{pmatrix} \sum\alpha\sin\theta_i^2 \\ \sum\beta\sin\theta_i^2 \\ \sum\gamma\sin\theta_i^2 \\ \sum\delta\sin\theta_i^2 \end{pmatrix} \tag{A.11}$$

Now a, b and c can be obtained from A, B and C by solving this matrix equation.

[1]. A. Taylor and H. Sinclair, Proc. Phys. Soc. **57**, 126 (1945)

Appendix B: Four-point probe measurement

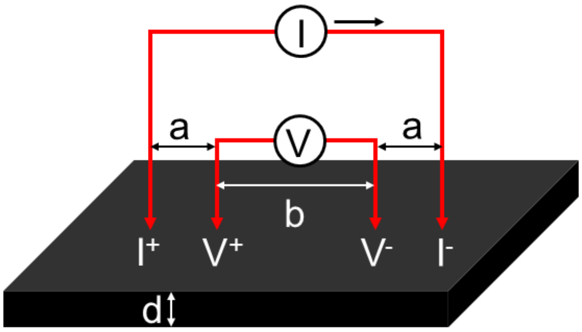

Figure 8.1: Illustration of four-point-probe measurement on a thin film of thickness d. The outer (current) and inner (voltage) probes are separated by a distance a. Distance between the two inner probes is b with a, b>>d.

In thin film, we consider circular equipotential surfaces neglecting the vertical distribution of current since a, b>>d. Therefore, the current density at a distance r from the current source (I^+) can be written as:

$$J(r) = \frac{I}{2\pi r d} \tag{B.1}$$

From Ohms law we have:

$$J = \sigma E = \frac{1}{\rho}E = -\frac{1}{\rho}\nabla V = -\frac{1}{\rho}\frac{\partial V}{\partial r} \tag{B.2}$$

& this gives,

$$V(r) = \frac{\rho}{2\pi d}\ln r \tag{B.3}$$

Therefore the potential drop between the two voltage probes is:

$$\Delta V = V^- - V^+ = \frac{\rho}{\pi d}\ln\frac{a+b}{a} \tag{B.4}$$

& therefore the resistivity of the film can be expressed as:

$$\rho = \frac{\pi \Delta V d}{I} \frac{1}{\ln \frac{a+b}{a}} \tag{B.5}$$

If the probes are equally spaced i.e. a=b, then the resistivity can be expressed as:

$$\rho = \frac{\pi \Delta V d}{I} \frac{1}{\ln 2} = 4.53 \frac{\Delta V d}{I} \tag{B.6}$$

Therefore, if all the four probes are equally spaced, the lead resistances can effectively be neglected in a resistivity measurement using four-point-probe method.